MARMARA UNIVERSITY

INSTITUTE FOR GRADUATE STUDIES
IN PURE AND APPLIED SCIENCES

MODIFICATION OF A THREE-EQUATION EDDY-VISCOSITY TURBULENCE MODEL FOR ANISOTROPIC TURBULENCE

MURAT UMUT YANGAZ

Ph.D. THESIS

Department of Mechanical Engineering

Thesis Supervisor

Prof. Dr. Mehmet Zafer GÜL

ISTANBUL, 2024

MARMARA UNIVERSITY

INSTITUTE FOR GRADUATE STUDIES
IN PURE AND APPLIED SCIENCES

MODIFICATION OF A THREE-EQUATION EDDY-VISCOSITY TURBULENCE MODEL FOR ANISOTROPIC TURBULENCE

MURAT UMUT YANGAZ

724614701

Ph.D. THESIS

Department of Mechanical Engineering

Thesis Supervisor

Prof. Dr. Mehmet Zafer GÜL

ISTANBUL, 2024

ACKNOWLEDGEMENT

Hereby, I am thankful for my advisor Prof. Dr. M. Zafer Gul who shared his knowledge and experience and for his endless support along with complete trust and patience, he showed during the whole thesis process. I would also like to thank Prof. Dr. Emre Alpman and Prof. Dr. Metin Muradoğlu for their guidance whenever I need guidance.

I would like to thank all my professors and friends in Chemical and Mechanical Engineering Departments of Marmara University.

This study, I hope, would fulfill its objective to reveal the importance of addressing anisotropy in RANS-based turbulence models is essential for improving the accuracy of simulations. The proposed modification incorporating anisotropy within a two-time scale framework holds promise for more accurate predictions in turbulent flows while mitigating the computational burden associated with DNS.

Also, this work was supported by the Scientific Research Projects Commission (BAPKO) of Marmara University under grant number FEN-C-DRP 131217-0677. This support is gratefully acknowledged.

During this study I made, I would like to thank my family who raised and supported me throughout my lifetime.

SEPTEMBER 2024 **Murat Umut YANGAZ**

CONTENTS

ÖZET

ÜÇ DENKLEMLİ BİR EDDY VİSKOZİTE TÜRBÜLANS MODELİNİN ANİZOTROPİK TÜRBÜLANS İÇİN GELİŞTİRİLMESİ

Türbülans, bir akış alanı içindeki hız, basınç ve yoğunluktaki düzensiz dalgalanmaları kapsayan, akışkanlar dinamiğinde karmaşık, kaotik ve her yerde bulunan bir olgudur. Türbülansın anlaşılması ve doğru şekilde modellenmesi, karmaşık ve çok ölçekli doğası nedeniyle temel zorluklar olmaya devam etmektedir. Türbülanslı akışlar, havacılıkta aerodinamikten endüstriyel proseslerde ısı transferine kadar çeşitli mühendislik uygulamalarında önemli bir rol oynamaktadır.

Hesaplamalı akışkanlar dinamiğinde (HAD), türbülanslı akışların simüle edilmesi, hız dağılımı, türbülans kinetik enerjisi ve kayma gerilimi gibi temel akış özelliklerini yakalamak için türbülans modellerinin kullanılmasını gerektirir. En sık kullanılan türbülans modelleri arasında yer alan Reynolds-Ortalamalı Navier-Stokes (RANS) modelleri, Navier-Stokes denklemlerinin zaman ortalamasını alarak hesaplamalı fizibilite sunar. Bununla birlikte, geleneksel RANS modelleri, türbülansın doğasında olan anizotropik doğasını göz ardı ederek izotropi varsaymaktadır.

Anizotropi, türbülans özelliklerinin yönsel bağımlılığını ifade eder. Anizotropinin ihmal edilmesi, özellikle karmaşık geometrilerde veya katı sınırlara yakın akış olaylarının tahmin edilmesinde yanlışlıklara yol açabilir. Türbülans modellemesinde daha iyi doğruluk için anizotropik etkilerin dahil edilmesi çok önemli hale gelir. Anizotropi, bir akış alanındaki momentumun, enerjinin ve skaler niceliklerin taşınmasını etkileyerek türbülansı önemli ölçüde etkiler.

Türbülanslı akışlardaki girdapların farklı ölçekleri göz önüne alındığında, anizotropiyi çözmek için RANS tabanlı bir modeli değiştirmek, iki zamanlı ölçek yaklaşımını Reynolds-Stress Modeli (RSM) bağlamında birleştirmeyi içerir. Bu değişiklik, farklı türbülans ölçeklerindeki anizotropik etkileri hesaba katmayı amaçlamaktadır. Değiştirilen model, anizotropik etkileri daha doğru bir şekilde yakalayarak, özellikle

duvarların yakınında veya türbülanslı sınır katmanları gibi anizotropinin önemli bir rol oynadığı bölgelerde simülasyonların doğruluğunu artırabilir.

Bu yaklaşım, tüm çalkantılı ölçekleri çözen ve çok büyük hesaplama kaynakları gerektiren Doğrudan Sayısal Simülasyon (DNS) ile karşılaştırıldığında, özellikle hesaplama verimliliği açısından potansiyel etkiler taşır. Değiştirilen modelin, DNS'ye kıyasla daha düşük hesaplama taleplerini korurken anizotropiyi verimli bir şekilde çözme yeteneği, onu pratik mühendislik uygulamaları, doğruluk ve hesaplama maliyetinin dengelenmesi için umut verici bir çözüm olarak konumlandırıyor.

Özetle, RANS tabanlı türbülans modellerinde anizotropinin ele alınması, simülasyonların doğruluğunun artırılması açısından önemlidir. Anizotropiyi iki zamanlı ölçek çerçevesinde birleştiren önerilen değişiklik, DNS ile ilişkili hesaplama yükünü hafifletirken türbülanslı akışlarda daha doğru tahminler için umut vaat ediyor.

ABSTRACT

MODIFICATION OF A THREE-EQUATION EDDY VISCOSITY TURBULENCE MODEL FOR ANISOTROPIC TURBULENCE

Turbulence stands as a complex, chaotic, and ubiquitous phenomenon in fluid dynamics, encompassing irregular fluctuations in velocity, pressure, and density within a flow field. Understanding and accurately modeling turbulence remain fundamental challenges due to its intricate, multi-scale nature. Turbulent flows play a pivotal role across various engineering applications, from aerodynamics in aviation to heat transfer in industrial processes.

In computational fluid dynamics (CFD), simulating turbulent flows necessitates the use of turbulence models to capture essential flow characteristics like velocity distribution, turbulent kinetic energy, and shear stress. Reynolds-Averaged Navier-Stokes (RANS) models, among the most commonly employed turbulence models, offer computational feasibility by time-averaging the Navier-Stokes equations. However, conventional RANS models assume isotropy, overlooking the inherent anisotropic nature of turbulence.

Anisotropy refers to the directional dependence of turbulent properties. Neglecting anisotropy can lead to inaccuracies in predicting flow phenomena, especially in complex geometries or near solid boundaries. The inclusion of anisotropic effects becomes crucial for better accuracy in turbulence modeling. Anisotropy significantly influences turbulence, affecting the transport of momentum, energy, and scalar quantities in a flow field.

Considering the diverse scales of eddies in turbulent flows, modifying a RANS-based model to resolve anisotropy involves incorporating a two-time scale approach in context with a Reynolds-Stress Model (RSM). This modification aims to account for anisotropic effects in different scales of turbulence. By capturing anisotropic effects more accurately, the modified model could enhance the fidelity of simulations, especially in regions where anisotropy plays a crucial role, such as near walls or in turbulent boundary layers.

This approach carries potential impacts, notably in computational efficiency compared to Direct Numerical Simulation (DNS), which resolves all turbulent scales and demands immense computational resources. The modified model's ability to resolve anisotropy efficiently while maintaining lower computational demands compared to DNS positions it as a promising solution for practical engineering applications, balancing accuracy and computational cost.

In summary, addressing anisotropy in RANS-based turbulence models is essential for improving the accuracy of simulations. The proposed modification incorporating anisotropy within a two-time scale framework holds promise for more accurate predictions in turbulent flows while mitigating the computational burden associated with DNS.

CLAIM FOR ORIGINALITY

The modifications implemented in the two-time scale three-equation turbulence model presented in this work are entirely original and have not been previously published or disclosed elsewhere in any scientific or academic literature. The adjustments made to this model are the result of rigorous and novel theoretical formulations, computational methodologies, and analytical insights derived from extensive research.

The unique modifications applied to the two-time scale turbulence model involve an innovative approach to resolve the anisotropy tensor by adopting a Reynolds Stress Model framework, addressing specific limitations in the existing model formulations. These alterations have been systematically designed and developed through a meticulous process that integrates comprehensive theoretical frameworks with empirical observations, resulting in a fundamentally distinct and previously unexplored enhancement of the model's capabilities.

Throughout the course of this research, no identical or substantially similar modifications to the specific two-time scale three-equation turbulence model, particularly regarding the resolution of the anisotropy tensor, have been identified in the academic or scientific domain. Therefore, the originality of these modifications is firmly asserted, and this work stands as the pioneering effort in introducing and implementing such advancements to refine and expand the model's predictive accuracy in capturing anisotropic turbulence effects.

The novel contributions presented herein have undergone rigorous scrutiny, validation, and verification processes, ensuring their authenticity and exclusive novelty. As such, the modifications made to the two-time scale three-equation turbulence model represent an original and unparalleled advancement within the field of turbulence modeling, promising significant contributions to the understanding and simulation of anisotropic turbulent flows.

SYMBOLS

$\mathbf{A_{ij}}$: Anisotropy Tensor

$\boldsymbol{C_1 - C_6}$: Coefficients of the WFC model

$\boldsymbol{C_\mu, C_{\varepsilon 1} - C_{\varepsilon 4}}$: Coefficients of the ε – equations

$\boldsymbol{C_{\tau 0}}$ **-** $\boldsymbol{C_{\tau 4}}$: Coefficients of the τ – equations

$\mathbf{C_1}$: Constant

$\mathbf{C_2}$: Constant

Co : Courant number

$\boldsymbol{C_f}$: Skin friction coefficient

d : Diameter of the initial jet

E : Constant of turbulence model

$\boldsymbol{f}$: Weighting factor

g : Gravitational acceleration

$\boldsymbol{k}$: Turbulent kinetic energy

$\boldsymbol{L}$: Turbulent length scale

p : Pressure

$\boldsymbol{P_k}$: Production of turbulent kinetic energy

$\mathbf{P_b}$: Production of turbulent kinetic energy due to buoyancy

R : Reynolds-Stress Tensor

$\mathbf{S_M}$: Source term

u : Flow velocity

$\mathbf{Y_M}$: Fluctuating dilatation term

GREEK SYMBOLS

$\boldsymbol{\varepsilon}$: Turbulent dissipation rate

$\epsilon_{\mathbf{ij}}$: Production of strain

$\mathbf{C_{3\varepsilon}}$: Constant

$\mathbf{C_{\mu}}$: Constant

Γ_{φ} : Diffusion constant

$\boldsymbol{\nabla}$: Gradient operator

$\boldsymbol{\lambda}$: Lambda

$\boldsymbol{\rho}$: Density of carbon monoxide

$\boldsymbol{\tau}$: Turbulent Time Scale

$\boldsymbol{\mu}$: Dynamic Viscosity

$\boldsymbol{\mu_t}$: Turbulent (Eddy) Viscosity

$\boldsymbol{\nu_t}$: Turbulent Kinematic Viscosity

$\boldsymbol{\varphi_{ij}}$: Production of strain

$\boldsymbol{\omega}$: Specific Dissipation Rate

ABBREVIATIONS

BFS : Backward-Facing Step

BO : Bayesian Optimization

CFD : Computational fluid dynamics

CFL : Courant-Friedrichs-Lewy

DES : Detached-Eddy Simulation

DNS : Direct Numerical Simulation

EASM : Explicit Algebraic Stress Model

EVM : Eddy Viscosity Model

FDM : Finite Difference Method

FEM : Finite Element Method

FVM : Finite Volume Method

GRE : General Richardson Extrapolation

HPC : High-Performance Computing

HWA : Hot-wire Anemometer

ICE : Internal Combustion Engine

JL : Jones-Launder

KMM : Kim-Moin-Moser

LDA : Laser-Doppler Anemometry

LDV : Laser-Doppler Velocimetry

LES : Large-Eddy Simulation

LEVM : Linear Eddy Viscosity Model

LHS : Left hand side

LRN : Low-Reynolds Number

MTS : Multiple Time Scale

NLEVM : Non-Linear Eddy Viscosity Model

OpenFOAM : Open Field Operation and Manipulation

RANS : Reynolds-Averaged Navier-Stokes

RDT : Rapid Distortion Theory

RFDF : Regularized Filtered Density Function

RNG : Renormalization Group

RCM : Reciprocating Compressor Model

RDM : Reynolds Stress Differential Model

RHS : Right hand side

RSM : Reynolds Stress Model

RST : Reynolds Stress Transport

RSTM : Reynolds Stress Transport Model

SAS : Scale-Adaptive Simulation

SGS : Sub-grid scale

SIMPLE : Semi-Implicit Method for Pressure-Linked Equations

SPF : Separation-Modified Production-to-Dissipation Ratio

SST : Shear Stress Transport

SST-LM : Shear Stress Transport Langtry-Menter

TDR : Turbulent Dissipation Rate

TKE : Turbulent Kinetic Energy

TTS : Two Time Scale

WALE : Wall-Adapting Local Eddy-Viscosity

WR : Wilcox-Rubesin

WFC : Wu-Ferziger-Chapman

LIST OF FIGURES

LIST OF TABLES

1. INTRODUCTION

Turbulence stands as a complex and ubiquitous phenomenon in fluid dynamics, characterized by chaotic, irregular, and seemingly random fluctuations in velocity, pressure, and density within a flow field. Understanding turbulence remains a fundamental challenge in science and engineering due to its intricate nature and widespread occurrence in natural and industrial processes.

Various forms of turbulence, such as shear turbulence, convective turbulence, and boundary layer turbulence, manifest in different flow scenarios. Shear turbulence results from fluid flow over surfaces like aviation wings, while convective turbulence occurs in heated or chilled fluids. Boundary layer turbulence arises from fluid interaction with solid surfaces.

At its core, turbulence arises from the interaction of multiple scales of motion within a fluid. It involves the formation of vortices, eddies, and swirls across a wide range of length and time scales, exhibiting rapid changes in magnitude and direction. These turbulent structures lead to enhanced mixing, increased drag, and amplified heat and mass transfer rates within the flow.

Turbulence models serve as indispensable tools in understanding and simulating turbulent flows, providing a framework to predict the complex behavior of fluid motion. They balance computational efficiency with accuracy in capturing turbulence phenomena. However, due to its complex and chaotic nature, turbulence is difficult to predict with absolute precision (Bailly & Comte-Bellot, 2015).

The methodologies for modeling and resolving turbulence can be categorized into experimental, numerical, and theoretical approaches:

- Experimental methods involve direct measurement of fluid flow using techniques like Particle Image Velocimetry (PIV), Hot-Wire Anemometry (HWA), Laser-Doppler Velocimetry (LDV), and pressure sensors, providing data for validating turbulence models and understanding turbulence phenomena.

- Numerical methods employ mathematical models and computer simulations. These include Reynolds-Averaged Navier-Stokes (RANS), Large-Eddy Simulation (LES), and Direct Numerical Simulation (DNS). DNS solves the Navier-Stokes equations without approximations, offering accurate representations but demanding significant computational resources.
- The use of mathematical models and theories to comprehend the underlying physics of turbulence constitutes theoretical methods. The Kolmogorov theory, which describes the energy cascade process in turbulence and predicts the energy distribution at various scales, is one of the most influential theories in turbulence. The turbulence closure problem necessitates the development of mathematical models to predict the effect of turbulence on fluid flow.

In conclusion, turbulence remains a challenging yet crucial aspect of fluid dynamics. Balancing computational efficiency with accuracy remains a primary goal in turbulence modeling. Recent advancements offer promising avenues to enhance predictive capabilities, but understanding the strengths and limitations of turbulence models is crucial for selecting appropriate models for specific flow scenarios (Hart, 2016; Zhang et al., 2007).

Turbulence models face challenges in accurately predicting transitional flows, handling wall-bounded flows, and capturing multi-scale turbulence phenomena. Recent advancements involve machine learning techniques, data-driven approaches, and improvements in hybrid modeling strategies to enhance predictive capabilities while balancing computational costs. Understanding the strengths and limitations of various turbulence models is crucial in selecting an appropriate model for specific flow scenarios. Balancing computational efficiency with accuracy remains a primary goal in turbulence modeling. As the field continues to evolve, advancements in modeling techniques and computational capabilities offer promising avenues to improve the fidelity of turbulent flow simulations for practical engineering applications.

Recent advancements in turbulence modeling involve the development of hybrid models such as Detached Eddy Simulation (DES), which combines RANS and Large Eddy Simulation (LES) approaches to capture both large and small turbulent scales efficiently.

Furthermore, machine learning and data-driven techniques have emerged as promising tools for improving turbulence models, leveraging vast datasets to enhance model accuracy and efficiency. In conclusion, turbulence represents a challenging yet essential aspect of fluid dynamics. Turbulence modeling plays a crucial role in predicting and understanding the behavior of turbulent flows in various engineering applications. Addressing the limitations of traditional models and incorporating advancements in turbulence research are vital steps toward achieving more accurate and reliable turbulence predictions, enabling better designs and optimizations in engineering systems.

It is clear that the topic of turbulence modeling is broad and there are many studies on developing faster, accurate, stable and less case-sensitive models. They basically consist of RANS, LES or DNS approaches as well as Lattice-Boltzmann Methods (LBM) and hybrids (i.e., DES). However, with the exception of DNS all the other models lack in some aspect of modeling turbulence correctly. And due to large computational costs, DNS could be carried out by a small portion of researchers. Therefore, there is a necessity to develop more capable and less costing models nowadays.

1.1.Thesis Outline

In this study, our aim was to develop a three-equation model (i.e., k-ε-τ and k-ω-τ) using an eddy-viscosity and/or coupling the equation(s) with a Reynolds Stress Model (RSM) to capture anisotropy in the Reynolds Stress matrix better. The results have been validated with the experimental data and will be compared with existing turbulence models in the following sections.

Firstly, the study presents a brief introduction, the methods for resolving turbulent flows, literature review and evaluation of existing models and their weaknesses. After that, there are serious work presented on how to overcome the defined drawbacks. The newly developed model has been verified for simple flow types such as round jet, wall jet, and wake in free shear flow category. After verification, further improvements and modifications on the model have been done accordingly whenever it is necessary.

In his model, Gul tested the so-called k-ε-τ three-equation turbulence model for simple free-shear flows (Z. Gul, 1994). Results were encouraging since spreading rates were predicted better than the standard k-ε model. We started testing this basic model to a

number of free and wall-bounded flows. These include 2D planar jets, 3D jets (i.e., axisymmetric jet), backward-facing step as well as channel flow and flat plate boundary layer flow. This required further modification to the model and adoption of data-driven methods for optimization of the model coefficients.

Second stage of this work is the testing of the model for anisotropic turbulence cases. At this stage, we have considered a number of approaches existed in the literature. This includes adopting RSM approach coupled with a second time scale.

All these cases have been tested on OpenFOAM (Moukalled et al., 2016), which is an open-source platform for CFD simulations.

1.2.Background: Resolving Anisotropy in RANS-Based Turbulence Models

In CFD, simulating turbulent flows necessitates the use of turbulence models to capture essential flow characteristics like velocity distribution, turbulent kinetic energy, and shear stress. RANS models, among the most commonly employed turbulence models, offer computational feasibility by time-averaging the Navier-Stokes equations. However, conventional RANS models assume isotropy, overlooking the inherent anisotropic nature of turbulence (Davidson, 2015).

Anisotropy refers to the directional dependence of turbulent properties. Neglecting anisotropy can lead to inaccuracies in predicting flow phenomena, especially in complex geometries or near solid boundaries. The inclusion of anisotropic effects becomes crucial for better accuracy in turbulence modeling. Anisotropy significantly influences turbulence, affecting the transport of momentum, energy, and scalar quantities in a flow field.

Considering the diverse scales of eddies in turbulent flows, modifying a RANS-based model to resolve anisotropy involves incorporating a two-time scale approach coupled with the Reynolds Stress Model framework. This modification aims to account for anisotropic effects in different scales of turbulence. By capturing anisotropic effects more accurately, the modified model could enhance the fidelity of simulations, especially in regions where anisotropy plays a crucial role, such as near walls or in turbulent boundary layers.

This approach carries potential impacts, notably in computational efficiency compared to DNS, which resolves all turbulent scales and demands immense computational resources. The modified model's ability to resolve anisotropy efficiently while maintaining lower computational demands compared to DNS positions it as a promising solution for practical engineering applications, balancing accuracy and computational cost.

In summary, addressing anisotropy in RANS-based turbulence models is essential for improving the accuracy of simulations. The proposed modification incorporating anisotropy within a two-time scale framework holds promise for more accurate predictions in turbulent flows while mitigating the computational burden associated with DNS.

1.3.Methods of Resolving Turbulence

There are basically two different approaches in resolving turbulence. One is through modelling, the other one is resolving all scales in a simulation domain (i.e., DNS).

In the context of turbulence physics and modeling, the concept of "closure" refers to the process of obtaining a closed set of equations from an open system of equations. Turbulent flows are described by the Navier-Stokes equations, which include terms representing the Reynolds stresses. These Reynolds stresses, in turn, depend on the velocity gradients and are unknowns in the Navier-Stokes equations. Closure in turbulence modeling involves finding a way to express these unknown Reynolds stresses in terms of known quantities (Tannehill et al., 2013).

Closure Problem in Turbulence Physics:

The closure problem arises because the Navier-Stokes equations, when written in their full form, contain terms involving higher-order moments of velocity that represent the interactions between various turbulent scales. Solving these equations directly would require knowledge of these higher-order moments, creating an infinite hierarchy of equations (Pope, 2000).

Methodologies to Address Closure:

- *Turbulence Modeling*: Closure is achieved in turbulence modeling by introducing turbulence models within the framework of RANS equations. These models, such

as eddy-viscosity models (e.g., k-ε, k-ω), aim to close the RANS equations by expressing the unknown Reynolds stresses in terms of known flow quantities. They assume a relationship between turbulent stresses and mean flow variables, introducing additional transport equations for turbulent quantities.

- *Reynolds Stress Models (RSM)*: RSM directly solves for the individual components of the Reynolds stress tensor. Unlike eddy-viscosity models, RSM aims to provide closure by solving a system of equations for the individual components of Reynolds stresses. This approach captures the anisotropic nature of turbulence more accurately but requires solving additional equations, increasing computational cost.
- *Large Eddy Simulation (LES)*: In LES, the closure problem is addressed by resolving larger turbulent structures explicitly while modeling smaller scales using subgrid-scale (SGS) models. LES bypasses the closure problem associated with RANS by directly simulating larger eddies while modeling the smaller unresolved scales.
- *Statistical Closure Theories*: These theories attempt to formulate closure schemes based on statistical properties of turbulence, such as correlations between different flow variables. They explore mathematical approaches to approximate the interactions between turbulent scales by invoking statistical assumptions.

<u>Challenges in Closure:</u>

- *Scale Interactions*: Capturing interactions between different turbulent scales accurately poses challenges, especially in complex flows.
- *Turbulence Anisotropy*: Modeling anisotropic turbulence behavior accurately remains challenging, especially near solid boundaries or in shear flows.
- *Modeling Assumptions*: Turbulence models rely on empirical constants and assumptions, potentially limiting their applicability in diverse flow conditions.

Turbulence models are utilized instead of directly solving the Navier-Stokes equations for several reasons (Tu et al., 2012):

- *Computational Complexity*: Turbulent flows involve a wide range of length and time scales. Directly solving the Navier-Stokes equations to simulate turbulent flows, without a turbulence model, would require resolving all these scales,

leading to an enormous computational cost. Turbulence models help reduce computational requirements by providing closure to the equations, allowing simulation at a manageable computational expense.

- *Inaccessible Small Scales*: In turbulent flows, a significant portion of energy resides in the small-scale turbulence, which is computationally expensive to resolve. Turbulence models, especially RANS models, average out these small scales, providing a computationally feasible approach by considering only the mean flow and certain turbulence quantities.
- *Boundary Layer and Wall Effects*: Near solid boundaries, such as walls, the complexity of turbulence increases significantly. Resolving this complexity in numerical simulations demands extremely fine grids, making direct simulation impractical. Turbulence models, especially those designed for near-wall treatments, help capture boundary layer effects more efficiently.
- *Engineering Applications*: For most engineering applications, obtaining precise details of small-scale turbulence might not be necessary. Turbulence models, particularly RANS models, are adequate in predicting mean flow characteristics, making them more suitable for practical engineering simulations where accuracy at a reduced computational cost is paramount.
- *Experimental Validation and Data Availability*: Turbulence models are extensively validated against experimental data. They provide a balance between accuracy and computational cost, allowing comparisons and validations against experimental results, making them more widely accepted in engineering practice.
- *Understanding and Interpretation*: Turbulence models provide insights and understanding of turbulent flow behavior. They help interpret flow phenomena by providing information about turbulent quantities like turbulent kinetic energy, eddy viscosity, and other turbulence-related parameters.
- *Suitability for Different Flow Conditions*: Different turbulence models cater to various flow conditions. Models like LES are suitable for capturing large turbulent structures, while RANS models are effective in capturing mean flow properties in various engineering applications.

In summary, turbulence models serve as practical tools that strike a balance between computational resources and accuracy, allowing engineers and scientists to simulate

turbulent flows efficiently while capturing essential flow characteristics. They provide a reasonable compromise between computational complexity and accuracy, making them indispensable for a wide range of engineering and scientific applications.

1.3.1. Reynolds-Averaged Navier-Stokes (RANS) Modelling

RANS models aim to predict mean flow behavior by time-averaging the Navier-Stokes equations, accounting for unresolved turbulent fluctuations. These models introduce additional transport equations for turbulent quantities (e.g., turbulent kinetic energy, dissipation rate) and approximate the Reynolds stresses using empirical closures.

RANS models employ turbulence closure models (e.g., k-ε, k-ω) to estimate turbulent viscosity and model turbulent stresses. These closures involve empirical coefficients and assumptions to predict turbulence behavior, assuming eddy viscosity and isotropy.

RANS models find extensive use in engineering simulations due to their computational efficiency. They are applied in aerodynamics, combustion, and industrial fluid flows where accurate predictions of mean flow properties are crucial, but resolving small-scale turbulent structures is less critical (Wilcox, 2006).

1.3.1.1.Linear Eddy Viscosity Models (EVMs)

Linear eddy-viscosity models belong to the class of eddy-viscosity models. These models assume a linear relationship between the Reynolds stresses and the mean velocity gradients, where the eddy viscosity (ν_t) is proportional to the turbulent kinetic energy (k) and the length scale (Piquet, 1999).

Examples of linear eddy-viscosity models include the widely used k-ε models (such as the Standard k-ε and RNG k-ε models). These models employ an eddy-viscosity concept to close the RANS equations, assuming isotropic turbulence and utilizing simplified relationships to express the eddy viscosity.

Linear eddy-viscosity models assume isotropy and have limited accuracy in capturing anisotropic turbulence effects, particularly in complex flows near walls or in shear layers. These models rely on empirical constants and may struggle in predicting complex turbulence behaviors accurately.

These models can be classified as zero-equation (algebraic models), one-equation, two-equation, three-equation, and four-equation models:

a) Zero-equation models (Algebraic models)

Zero-equation models in turbulence modeling assume a direct relationship between the turbulent viscosity and a characteristic length scale, typically represented by a single equation without additional transport equations for turbulence quantities. These models are among the simplest turbulence models and are based on empirical assumptions about the turbulent length scale. They are often used in cases where computational resources are limited or where simplicity is preferred over accuracy.

Zero-equation models are applied in cases where turbulence is relatively simple or where computational resources are limited. These models are used in initial or preliminary stages of simulations to estimate turbulence effects.

They rely on oversimplified assumptions and might not capture complex turbulent behaviors accurately. Zero-equation models might not be suitable for flows with intricate turbulence characteristics or complex geometries.

Zero-equation models, such as the Mixing-Length Model and its variants like Prandtl's Mixing Length Model, offer simplicity in turbulence modeling by directly relating turbulent viscosity to a characteristic length scale. While they are computationally inexpensive and straightforward, they often lack accuracy in predicting turbulence in complex flow conditions and might be limited in their applicability compared to more sophisticated turbulence models.

<u>Some of the Zero-Equation Models:</u>

- Cebeci-Smith Model (Smith & Cebeci, 1967)
- Mixing-Length Model (Prandtl, 1925)
- Baldwin-Lomax Model (Baldwin & Lomax, 1978)

b) One-equation models

One-equation turbulence models are a class of RANS turbulence models that introduce a single additional transport equation to represent turbulence within the

flow field. These models aim to predict the behavior of one primary turbulence quantity, often the turbulent kinetic energy (k), without explicitly solving for a separate transport equation for the dissipation rate (ε).

Some of the One-Equation Models:

- Baldwin-Barth Model (Baldwin & Barth, 1991)
- Shuai-Agarwal Turbulence Model (Shuai & Agarwal, 2020)
- Rahman-Agarwal-Siikonen Model (Rahman et al., 2011)
- Spalart-Allmaras Model (P. Spalart & Allmaras, 1992)

c) Two-equation models

Two-equation turbulence models are a class of RANS models that introduce two additional transport equations to predict two primary turbulent quantities within a flow field. These models offer more sophistication and versatility compared to one-equation models, allowing for a more detailed representation of turbulence phenomena.

Two-equation turbulence models, classified under the $k-\varepsilon$ and $k-\omega$ families, introduce two transport equations to predict turbulence characteristics more comprehensively than one-equation models. While $k-\varepsilon$ models offer simplicity and computational efficiency, $k-\omega$ models excel in handling boundary layers and transition regions more accurately. The choice of model depends on the specific flow conditions, accuracy requirements, and computational resources available for the simulation. These models can be listed as below:

- $k-\varepsilon$ model family
    - Standard $k-\varepsilon$ model (Launder & Spalding, 1974)
    - RNG $k-\varepsilon$ model (Yakhot et al., 1992)
    - Realizable $k-\varepsilon$ model (T. H. Shih et al., 1995)
- $k-\omega$ model family
    - $k-\omega$ model (Wilcox, 1988b)
    - *SST* $k-\omega$ model (Menter, 1994)
    - *SST-DES* $k-\omega$ model (Strelets, 2001)

- *SST-LM* $k-\omega$ model (Langtry & Menter, 2009)

Also, there are turbulence models that don't use the dissipation rate ε or the specific dissipation rate ω in their formulations. Instead, they employ different variables to represent the dissipation or length scales. Two notable examples are:

- $k-\tau$ model

The $k-\tau$ model introduces a transport equation for the turbulent timescale (τ) instead of the dissipation rate ε. This model aims to represent the timescale of turbulence rather than explicitly calculating the dissipation rate (Thangam et al., 1992).

- $k-L$ model

The $k-L$ model replaces the dissipation rate ε with a turbulent length scale (L). The transport equation involves the evolution of k along with the length scale L instead of ε (Chiravalle, 2006).

These models offer alternative approaches to represent turbulence and dissipation within the flow field without using the dissipation rate ε or specific dissipation rate ω traditionally found in $k-\varepsilon$ or $k-\omega$ models.

However, it's important to note that while these models offer different variable representations, they might have specific limitations or assumptions that influence their accuracy and applicability in various flow conditions. The $k-\tau$ and $k-L$ models might not be as widely used or recognized as the traditional $k-\varepsilon$ and $k-\omega$ models in most practical applications of CFD.

d) Three-equation models

Three-equation turbulence models are an extension of the commonly used two-equation models (such as the $k-\varepsilon$ or $k-\omega$ models) and aim to provide more detailed information about the turbulence behavior by introducing an additional transport equation for a third variable related to turbulence. These models typically involve equations for turbulent kinetic energy (k), turbulent dissipation rate (ε), and an additional variable related to anisotropy or another turbulence property.

Three-equation models aim to capture further turbulence details, such as the effects of rotation, turbulence length scales, or anisotropy, by introducing an additional transport equation. The third equation can represent various turbulence characteristics, such as the turbulent kinetic energy of the smallest turbulent eddies, the length scale of the turbulence, or a transport equation for anisotropic properties.

Examples of Three-Equation Turbulence Models:

1. *R-k-ε* Model (U. C. Goldberg, 1996)
2. $k - \overline{v^2} - \omega$ Modified Turbulence Model (Li et al., 2020)
3. *k-k*$_L$*-ω* Model (Fürst et al., 2013; Walters & Cokljat, 2008)
4. k-ε-R$_t$ Model (U. Goldberg et al., 2009)
5. *K-ε-V*$_n$ Model (Molchanov & Bykov, 2013)
6. $k - \varepsilon - \overline{\theta^2}$ Model (Mompean, 1994)
7. $K - \omega - \overline{\rho'^2}$ Model (J. Liu, 2013)
8. $k - \tilde{\varepsilon} - A_2$ Three-Equation Non-Linear Eddy Viscosity Model (Craft et al., 1997)
9. *K-ε-K*$_\rho$ Model (Duranti & Pittaluga, 2000)
10. *k-ε-α* Model (Ghirelli, 2007)
11. *k-L-a* Model (Morgan et al., 2018)
12. *k-ω-v*^{2} Model (Dhakal & Walters, 2011)
13. *K-K*$_\rho$*-ξ* Model (Yoshizawa, 1990)

Three-equation turbulence models aim to enhance the predictive capabilities of turbulence modeling by incorporating an additional transport equation for a third variable related to turbulence characteristics, anisotropy, or length scales. These models are developed to address specific limitations of traditional two-equation models by offering more detailed insight into complex turbulence phenomena. The choice of a specific model depends on the flow physics, desired turbulence details, and available experimental data for validation.

e) Four-equation models

Four-equation turbulence models are an extension of three-equation models, incorporating an additional transport equation to further capture the complexities of

turbulent flows. These models aim to provide more detailed information about the turbulence by introducing an extra equation typically related to the transport of an additional turbulence property or anisotropy parameter. The additional equation is meant to address specific aspects that may not be adequately represented in three-equation models, such as the effects of rotation, compressibility, or specific turbulence scales.

The four-equation turbulence models commonly consist of equations for TKE (k) that represents the fluctuating component of kinetic energy due to turbulence, TDR (ε) that indicates the rate at which turbulence dissipates energy and additional variables (e.g., turbulent scale, anisotropy parameter, etc.) that involve extra equation(s) which introduces a variable that captures more specific turbulence characteristics or properties. This equation aims to provide additional insight into certain aspects of turbulence that might be crucial in particular flow scenarios.

The goal of these models is to enhance the predictive capabilities of turbulence modeling by considering additional turbulence properties or parameters. By introducing an extra equation, four-equation models attempt to address limitations in simpler models and provide a more comprehensive understanding of turbulent flows, especially in complex flow situations where the standard models may fall short.

Existing Four-Equation Turbulence Models:

1. k-ε-θ^2-ε_θ Model (Sung & Chung, 1984)
2. k-ε-K-Ω Model (Barbi et al., 2022)
3. k-ε-k_t-ω_t Model (Grunloh, 2019)
4. k-ε-k_p-k_{fp} Model (Mashayek & Taulbee, 2002)
5. k_T-k_L-ω-v^2 Model (Chitta et al., 2013)
6. $k - \tilde{\varepsilon} - k_\theta - \widetilde{\varepsilon_\theta}$ Model (Su et al., 2022)

These models aim to provide a more comprehensive representation of turbulent flows by considering additional variables or properties that might significantly influence the flow behavior. However, the increased complexity comes with challenges in accurately determining model parameters and requires extensive validation against experimental or high-fidelity data to ensure their reliability in various flow conditions.

1.3.1.2.Non-Linear Eddy Viscosity Models (NLEVMs)

Non-linear eddy-viscosity models are a subset of eddy-viscosity models that exhibit non-linear behavior between the Reynolds stresses and mean velocity gradients.

These models aim to introduce non-linear effects within the eddy-viscosity concept, attempting to address some limitations of linear eddy-viscosity models. They attempt to account for deviations from isotropy and improve the representation of turbulence behavior in more complex flows.

Non-linear eddy-viscosity models aim to capture more complex turbulence phenomena by introducing additional terms or modifications to the eddy-viscosity formulation. They try to improve the accuracy of predictions in flows where linear models struggle but remain computationally more efficient compared to Reynolds Stress Models (Hanjalić & Launder, 2011).

1.3.1.3.Reynolds Stress Model (RSM)

Reynolds Stress Models (RSM) represent a different category of turbulence models compared to eddy-viscosity models. RSM directly solve for the individual components of the Reynolds stresses rather than relying on an eddy-viscosity assumption.

RSMs involve solving a system of equations for the six individual components of the Reynolds stress tensor, accounting for anisotropic turbulence. These models (Chou, 1945; T. J. Craft et al., 1996; Hanjalić & Launder, 2011; B. E. Launder et al., 1975; Rotta, 1951) capture the complexities of turbulence by explicitly modeling the Reynolds stresses based on transport equations for their individual components.

RSMs offer the advantage of accounting for anisotropy and more accurately representing turbulence near walls or in shear flows. However, they require additional computational resources due to the increased number of equations, making them more computationally expensive than eddy-viscosity models.

1.3.2. Large Eddy Simulation (LES)

Large Eddy Simulation (LES) is a CFD technique used to simulate turbulent flows by explicitly resolving larger-scale turbulent structures while modeling smaller-scale turbulence (Pope, 2000).

LES aims to separate turbulent flow into large and small scales. It resolves larger eddies explicitly while modeling smaller-scale turbulent fluctuations using SGS models. It primarily targets the larger, energy-containing eddies that significantly contribute to the turbulent kinetic energy within the flow.

LES employs spatial filtering of the Navier-Stokes equations, separating resolved and unresolved components of turbulence within the flow field. Filtered equations are derived by applying a spatial filter to the governing equations, resulting in the resolved scale equations and additional terms representing the SGS contributions (John, 2004).

SGS models approximate the effects of unresolved turbulent motions on the resolved scales. Various SGS models, such as the Smagorinsky model or dynamic models, represent the interactions between resolved and unresolved scales by providing closure for the filtered equations.

LES requires sufficient grid resolution to capture the larger turbulent structures adequately. Resolving the energy-containing eddies accurately depends on the computational grid's ability to capture these scales.

LES typically employs explicit or implicit time integration schemes to advance the flow solution in time. Time-step sizes are determined based on the Courant-Friedrichs-Lewy (CFL) condition to ensure numerical stability.

LES is computationally demanding due to its need to resolve a range of turbulent scales explicitly and model smaller scales using SGS models. Proper resolution of the larger scales necessitates finer grids, increasing computational expenses.

Challenges in LES:

- *Near-Wall Modeling*: Accurate modeling of near-wall turbulence remains a challenge in LES due to the complexity of flow near boundaries.
- *Subgrid-Scale Modeling*: Developing robust and accurate SGS models for various flow conditions and geometries remains an active area of research in LES.

LES finds applications in aerodynamics, aircraft and vehicle design, and turbomachinery simulations, where resolving detailed flow features is crucial. It aids in simulating

atmospheric boundary layers, pollutant dispersion, and environmental flows, providing insights into complex flow behaviors (Galperin & Orszag, 2010).

In short, LES is a powerful computational technique that explicitly resolves larger turbulent structures while modeling smaller scales using SGS models. It strikes a balance between the computational expense of DNS and the empirical assumptions of RANS models, making it valuable for understanding and predicting complex turbulent flows in various engineering and environmental applications. Ongoing research in LES focuses on refining SGS modeling and addressing computational challenges to extend its applicability to a wider range of flow scenarios.

LES employs various SGS models to approximate the effects of unresolved turbulent motions on the resolved scales. An overview of some common LES approaches and SGS models is given below (Garnier et al., 2009):

- Smagorinsky-Lilly Model:

This model, proposed by Smagorinsky and Lilly, introduces a turbulent viscosity term to represent the SGS stresses. The SGS stress is related to the resolved flow gradients through a proportionality constant (Smagorinsky constant) that determines the rate of energy transfer between resolved and unresolved scales.

- Dynamic Smagorinsky Model:

The Dynamic Smagorinsky Model aims to dynamically adjust the Smagorinsky constant based on the local flow features. It computes the Smagorinsky constant locally, adapting it to the resolved flow's strain rate. This offers better adaptability to varying turbulence levels in different flow regions.

- Wall-Adapting Local Eddy-Viscosity (WALE) Model:

The WALE model focuses on addressing near-wall turbulence effects more accurately than conventional models. It incorporates a function (localization function) that adapts the SGS model near walls, enhancing predictions in boundary layer flows where conventional SGS models might be less effective.

- Scale-Adaptive Simulation (SAS) Model:

The Scale-Adaptive Simulation model dynamically adjusts turbulent scales based on resolved flow gradients and local characteristics. It uses a scale-adaptive filter to distinguish between resolved and unresolved scales, offering an alternative to constant-coefficient SGS models.

- Approximate Deconvolution Models:

Approximate Deconvolution Models aim to recover SGS motions by deconvolving the resolved flow field. These models employ deconvolution operations (high-order filtering) to approximate the small-scale motions, enhancing the modeling of smaller scales within LES.

- Regularized Filtered Density Function (RFD) Model:

The RFD model employs stochastic techniques to represent the SGS effects. It uses a filtered density function to model the subgrid-scale motions, introducing a probabilistic approach to represent turbulence.

LES employs various SGS models like the Smagorinsky-Lilly model, Dynamic Smagorinsky model, WALE model, SAS model, Approximate Deconvolution models, and RFD model. Each model offers distinct methodologies to improve the representation of subgrid-scale turbulence in LES simulations. The choice of an SGS model often depends on the flow conditions, boundary effects, and accuracy requirements of the simulation. Ongoing research aims to enhance the accuracy and applicability of these models across diverse turbulent flow scenarios.

1.3.3. Detached Eddy Simulation (DES)

Detached Eddy Simulation (DES) is a hybrid turbulence modeling approach that combines elements of both RANS and LES techniques. It was developed to capture both the advantages of RANS in wall-bounded flows and the ability of LES to resolve large turbulent structures in separated and complex flow regions (P. R. Spalart, 2000).

RANS models are effective near solid boundaries but struggle to resolve larger turbulent structures. On the other hand, LES accurately resolves larger eddies but is computationally expensive, particularly near walls where fine grids are necessary. DES

seeks to strike a balance between accuracy and computational cost by utilizing RANS in attached boundary layers and LES in separated or transitional regions.

DES divides the flow domain into zones: a RANS mode in regions where RANS is effective (near walls and in attached boundary layers) and an LES mode in regions where larger eddies are crucial (in separated or transitional flow regions).

In the transition region between RANS and LES zones, DES employs a blending function to smoothly transition from the RANS to the LES mode. This transition is critical for a seamless exchange between the two modeling strategies.

DES relies on a scale-resolving turbulence model like the Spalart-Allmaras model or *SST k-ω* model for the RANS part, while switching to a subgrid-scale model (like the Smagorinsky model) for the LES part.

DES aims to provide accurate predictions of complex turbulent flows, particularly those with flow separation and transitional behaviors, at a reduced computational cost compared to LES.

Workflow of DES:

1. *Initialization*: Similar to LES or RANS simulations, DES starts with setting up the flow domain, specifying boundary conditions, and initializing the turbulence model parameters.
2. *Zonal Division*: The computational domain is divided into RANS and LES regions based on a predefined criterion, usually using the grid resolution or turbulent length scales.
3. *RANS Mode*: In the attached boundary layer zones, the flow is simulated using a RANS turbulence model, which models turbulence using a time-averaged approach. RANS models are computationally less expensive but lack accuracy in resolving larger turbulent structures.
4. *LES Mode*: In regions where, larger eddies are prevalent (such as flow separation regions), the simulation transitions to an LES approach, where larger turbulent structures are directly resolved on the grid while smaller eddies are modeled using a subgrid-scale model.

5. Transition and Blending: The transition zone between RANS and LES employs a blending function or filter that smoothly switches from RANS to LES modeling approaches, ensuring a seamless transition between the two zones.

DES has become a popular choice in computational fluid dynamics, especially for simulating complex turbulent flows where both attached and separated flow regions are present. Its ability to balance computational efficiency and accuracy in such scenarios makes it a valuable tool for various engineering applications.

1.3.4. Direct Numerical Simulation (DNS)

DNS is a computational technique used in CFD to solve the governing equations of fluid flow without any turbulence modeling. DNS provides a comprehensive and detailed solution by directly resolving all spatial and temporal scales of turbulent motion within a flow domain.

DNS solves the complete set of unsteady Navier-Stokes equations, considering conservation of mass and momentum without any turbulence model. These equations describe the behavior of fluid motion and account for viscous effects, inertia, and pressure gradients in the flow.

DNS discretizes both spatial and temporal domains finely enough to resolve the smallest turbulent scales present in the flow. This high-resolution discretization involves a very dense grid for spatial discretization and a small-time step for temporal discretization.

Unlike RANS or LES methods, DNS directly resolves all turbulent fluctuations down to the Kolmogorov microscales without any need for turbulence closure models (Orszag, 1970).

Workflow of DNS:

1. *Grid Generation*: DNS requires a highly refined grid to capture the smallest turbulent structures. Generating this grid is computationally demanding, especially for complex geometries or three-dimensional flows.
2. *Initialization*: The flow domain is initialized with known or prescribed initial conditions, such as velocity, pressure, and density distributions, to start the simulation.

3. *Time Integration*: The Navier-Stokes equations are solved iteratively over time using numerical methods like finite difference, finite volume, or spectral methods. The time step used in DNS is usually limited by the CFL stability condition, which ensures numerical stability.
4. *Numerical Solvers*: Sophisticated numerical solvers are employed to compute the convective, viscous, and pressure terms in the Navier-Stokes equations accurately.
5. *Computational Resources*: DNS demands substantial computational resources due to the need for fine spatial and temporal resolutions. High-Performance Computing (HPC) clusters or supercomputers are often used to handle the computational demands of DNS.

DNS provides highly accurate and detailed information about turbulent flows, capturing all scales of turbulence, making it a valuable tool for fundamental turbulence research and validation of turbulence models.

It is computationally expensive due to the requirement for fine grid resolution and small-time steps, making it impractical for many industrial applications or large-scale simulations.

DNS is often limited to low-to-moderate Reynolds number flows due to its computational demands. Higher Reynolds numbers increase the range of turbulent scales, demanding finer grid resolutions and significantly increasing computational costs.

It serves as an essential tool for understanding fundamental turbulence physics and validating turbulence models but is typically limited to academic research or small-scale simulations due to its computational intensity.

1.4.Literature Review

Most flows in real world are in turbulent region such as flow around a wing of an airplane, exhaust gas getting out of a rocket's exit nozzle or the atmospheric boundary layer over the surface of the Earth. In this regard, modeling turbulence becomes quite important. Turbulence can be described by a fluid's unpredictable characteristics coupled with various spatial and time scales in a flow. This phenomenon can occur when the driving force of motion, the kinetic energy becomes so intense that, it allows the fluid to overcome the viscous effects The fluid motion tends to become unstable if the viscous damping gets too weak (Bailly & Comte-Bellot, 2015).

Turbulence in shear-free domains is used as references in measuring the capability of turbulence models developed, since, they are well investigated experimentally and documented in the literature. There are many studies in the literature that are related to the behavior of the turbulence in different type of flows.

Fares et al. developed a general one-equation model suitable for both free-shear and wall-bounded flows. They aimed to achieve a capability to model turbulence entities for various flow types including wake, boundary layer, vortical flows and jet flows. They also claimed that the model they developed, which was derivated from a two-equation *k-ω* turbulence model by themselves, had superiorities over the well-known one equation model, Spalart-Allmaras for vortical and jet flows without affecting the quality and efficiency of the outcomes. They compared and validated their model with the *k-ω* and Spalart-Allmaras model (Fares & Schröder, 2005). Using data-driven techniques, Zhao et al.'s objective was to investigate wake mixing in turbomachines. They trained a model on a high-pressure turbine case and subsequently tested it for three additional cases, all of which are representative of contemporary turbine nozzles. They were able to accomplish significant improvements (Zhao et al., 2020).

Ma et al. compared five different two-equation turbulence models (i.e., *SST k-ω*, standard *k-ε*) in a curved (90^o) rectangular duct evaluating the turbulence parameters. They validated the results with existing experimental data in the literature. They have presented their findings as a reference for similar applications. They stated that standard *k-ε* is the most efficient in terms of computational time. On the other hand, it had the lowest capability to predict the relevant quantities. Also, they found that k-ω SST model was more compliant with the experimental data in 3D cases. However, its predicting performance remained rather poor. Finally, they observed that LS model, as being one of the low-Re models, showed better outcomes for turbulent kinetic energy (TKE) and Reynold Stresses. Overall, they summed up by mentioning that all the models they compared had indicated weaknesses on matching the experimental data, with LS' superiority over the rest (Ma & Lai, 2016). Savio et al. studied the comparison of different two-equation turbulence models including Jones and Launder's (JL) and Wilcox and Rubesin's (WR) for low supersonic flows along a ramp and medium-level supersonic flows around a blunt body. They had proven that the results of WR yielded more critical

pressure fields than JL's. WR showed better prediction capabilities on the angle of shock in the ramp problem and pressure at the stagnation points after the blunt body. They also mentioned that pressure distributions on the wall were better predicted by JL for the ramp case, despite the slight under-prediction. In the blunt body problem, pressure values at the stagnation region were better for WR with 3.83% error. Due to the insignificance of 2.1% computational cost advantage of JL, they declared that WR was superior to JL (Sávio & Maciel, 2011). Igci et al. evaluated four different low-Reynolds *k-ε* models (Lam-Bremhorst, Abe-Kondoh-Nagano Chien, and Launder-Sharma) for periodic fully developed duct flow and heat transfer (Igci & Arici, 2016). On the other hand, newer studies focused on calibration, optimization, and applications of neural networks, such as the study of Portal-Porras et al.'s. The Convolutional Neural Network (CNN) method was implemented by the authors on a two-layer *k-ε* turbulence model (Portal-Porras et al., 2021). In addition, they have developed a Realizable two-layer *k-ε* model that takes into account the influence of the viscous affected layer.

A normalizing technique was employed to ensure that the features were scaled between the range of 0 and 1:

$$\varphi' = \frac{\varphi - \min(\varphi)}{\max(\varphi) - \min(\varphi)} \tag{1.1}$$

The data was divided into three parts: 60% for training, 30% for validation, and 10% for testing.

Kashefi et al. employed CNN to obtain precise outcomes for the velocity and pressure distributions of stagnant fluids around basic geometric obstacles (Kashefi et al., 2021). Remarkably, their approach demonstrated computing efficiency that was three to five orders of magnitude lower than traditional CFD simulations.

Several other studies also made these model comparisons. Singh et al. compared several turbulence models in the context of simulating the flow over a backward facing step (BFS). The turbulence models compared in this study include the *SST k-ω*, *k-ω*, *Lien Cubic k-ε, Shih Quadratic k-ε*, *k-ε*, and *Realizable k-ε* models (Singh et al., 2020). The comparison was based on the assessment of the reattachment lengths predicted by each turbulence model. The reattachment length is a critical parameter in the study of flow

separation and reattachment phenomena. It indicates the distance downstream from the step at which the separated flow reattaches to the surface. The re-attachment lengths for different numerical models and the experimental value were presented in millimeters and non-dimensionalized distance (x/S) in the manuscript. Here are the re-attachment lengths for the different numerical models and the experimental value that they mentioned in their work:

- *SST k-ω*: 43.89 mm (8.96 x/S)
- *k-ω*: 45.02 mm (9.18 x/S)
- *Lien Cubic k-ε*: 35.51 mm (7.25 x/S)
- *Shih Quadratic k-ε*: 32.77 mm (6.68 x/S)
- *k-ε*: 28.87 mm (5.89 x/S)
- *Realizable k-ε*: 40.13 mm (8.19 x/S)
- Experimental (Armaly et al., 1983): 39.40 mm (8.04 x/S)

In addition to the quantitative assessment, the authors also conducted qualitative visualizations to compare the flow characteristics predicted by each turbulence model. These visualizations, using velocity magnitude contours, revealed differences in the size and position of the recirculation zones and vortices for each turbulence model. Notably, the *k-ω* model was observed to have the largest primary vortex, leading to the maximum reattachment length, while the *SST k-ω* model exhibited a moderate size of the secondary vortex and primary vortex compared to the other models.

Optimization and calibration studies are trending topics in turbulence modeling subject. Within that particular framework, Barkalov et al. examined the phenomenon of slope flow and sought to identify the most favorable parameter values (Barkalov et al., 2022). The simulation of the slope flow scenario was conducted using the SST k-ω model. The turbulence model coefficients were determined using the Global Search Method (GSM) to find the optimal values. Calibration was conducted to enhance the resemblance between the experimental and computed velocity profiles. The optimization task employed the root mean square error (RMSE) as the objective function to measure the difference between the calculated and experimental values. To address the multi-extremal optimization problem that arises when searching for the minimum of the loss function. To minimize the dimensionality of the problem, an optimization strategy was employed

utilizing a Peano curve for the flow velocity profile. In order to expedite the optimization process, the objective function was approximated utilizing an ANN. The researchers have examined six parameters of turbulence models and conducted the specified research using OpenFOAM and Globalizer software.

The researchers utilized the MLPRegressor class from the scikit-learn machine learning framework to build an approximation of the goal function. The system utilizes a Multilayer Perceptron (MLP) that is trained via error backpropagation without an activation function in the output layer.

The researchers employed a three-layered neural network (NN) to address the approximation problem. This choice was made because of the NN's ability to achieve high accuracy. Additionally, the usage of a deep neural network (DNN) was deemed unnecessary owing to the redundancy it would introduce. The dataset utilized to construct the approximation was limited in size, making it insufficient for training a deep network.

The selection of the solver, the activation function, the regularization parameter value, and the number of neurons in the hidden layer are all adjustable parameters of the neural network. The "lbfgs" solution has been shown to be superior and more efficient for small sets of multi-dimensional data.

For their computational experiment, they used the subsequent network architecture:

model=MLPRegressor(activation='logistic', solver='lbgfs', alpha=0.001, hidden_layer_sizes(20;), max_iter=5000, tol=10e-6, random_state=10)

A small study was conducted to determine that β^*, α_1, $\alpha_{k1,2}$ and $\alpha_{\omega 1,2}$ have the highest level of significance in influencing the outcomes. They adjusted or fine-tuned these factors.

Another study which focuses on adopting a computational coupling of ML and RANS (W. Liu et al., 2021). The authors evaluated the effectiveness of their method by applying it to Channel Flow and Periodic Hills scenarios. The model was trained using the channel flow example and evaluated on periodic hills, demonstrating superior performance compared to the SST k-ω model. An ML technique, namely a neural network (NN), was employed to develop a functional representation of correction coefficients in the equations governing turbulent transport. The SA and k-ω model have been tested by the authors. The researchers developed an iterative computational framework that integrates

ML with RANS solver. The main objective of this framework is to accurately replicate the instance that was used to train the ML models. The main breakthrough was achieved by solving traditional turbulence equations utilizing high-fidelity mean flows as input, instead of relying on imported high-fidelity data to generate turbulence numbers.

Recent advancements lead to many new studies and methodologies. For instance, Duarte et al. employed the optimization technique known as kriging and Bayesian methods to optimize specific coefficients of the k-ε turbulence model (Duarte et al., 2020). Following Lefantzi et al.'s calibration method to tackle the issue of forecasting k-ε RANS simulation of a jet in crossflow (JIC) (Lefantzi et al., 2014). By combining C_{μ}, $C_{\varepsilon 1}$, $C_{\varepsilon 2}$ and doing regression analysis on the Reynolds Stresses using a basic polynomial, the researchers created a surrogate model for the 2D RANS model. They then used this model to determine a joint distance for the k-ε parameters by solving a Bayesian inverse problem, taking into account the experimental data. While the model was calibrated specifically for JIC, it has also been demonstrated to be applicable to two additional scenarios: the Volvo example and the high-rise building instance.

Bayesian analysis (BA) is frequently employed to adjust RANS closures in order to enhance the precision of predictions (as demonstrated with the Launder-Sharma k-ε, k-ω Wilcox, SA, and Baldwin-Lomax models). de Zordo-Banliat et al. utilized Bayesian analysis on compressor cascades to derive a collection of calibrated turbulence model parameters in response to the deficiencies of the initial model (de Zordo-Banliat et al., 2020). Cheung et al. employed Bayesian analysis to adjust the coefficients of the SA turbulence model in order to rectify model shortcomings and accurately replicate the characteristics of a turbulent boundary layer on a flat plate (Cheung et al., 2011). Guillas et al. calibrated the k-ε model among other related researches (Guillas et al., 2014).

A recent study (Almohammadi, 2020) revolved around the examination of BFS flow at a Reynolds number of 37,000. The main focus was on evaluating various turbulence models regarding their capacity to predict the reattachment length. The study utilized three different grid types to determine the most accurate solution for the turbulence model being studied. A modified general Richardson extrapolation (GRE) technique was employed to estimate the reattachment length, resulting in a calculated value of 6.79 h. According to the findings, this predicted value closely aligned with experimental data, exhibiting a

small percentage error of merely 0.15%. The results suggested the effectiveness of turbulence models in predicting reattachment length, contingent upon the achievement of grid-independent solutions. Additionally, the application of the modified GRE method was found to significantly reduce computational costs compared to conventional grid refinement methods. The visual representations of the flow field validated the turbulence models' ability to capture the separation-reattachment mechanism accurately. Similar trends were observed in both wall shear stress along the computational domain bed and vorticity magnitude in the 2D cross-sectional area of the tunnel. The paper's findings provided substantial insights into obtaining grid-independent solutions and facilitating a comprehensive comparison of turbulence models' performance. Specifically, it contributed to enriching the understanding of turbulence modeling within the context of a fundamental fluid flow problem, namely, the BFS flow.

Hamlington and Ihne reported on the modeling of compressed turbulence (Hamlington & Ihme, 2014), where they compared various closure models. This comparison included equilibrium models based on the Boussinesq hypothesis, second-order Reynolds stress transport models (RSTMs), and differential models. According to their findings, equilibrium models, while computationally stable and efficient, have limitations in accurately representing non-equilibrium effects in rapidly strained flows. In contrast, second-order Reynolds stress transport models (RSTMs) can address non-equilibrium flow effects, but they exhibit poor computational stability and increased complexity due to the necessity of closures for several terms.

The study also introduced a new non-equilibrium model for the anisotropic Reynolds stress tensor. This newly proposed model was found to be in relatively good agreement with the results obtained from the integration of the full Reynolds stress differential model (RDM). This agreement suggests that the approximations and assumptions made to derive the new non-equilibrium model closure are reasonable for Internal Combustion Engines (ICEs) and Reciprocating Compressor Models (RCMs).

Furthermore, the research investigated the evolution of turbulence kinetic energy and stresses in ICEs and RCMs under non-equilibrium conditions. The results demonstrated that the non-equilibrium model aligns well with the outcomes from the Reynolds stress differential model, particularly for situations involving large degrees of non-equilibrium.

On the other hand, various studies have been carried out on multiple time scale models (MTS) (C. P. Chen & Guo, 1991; Hanjalic et al., 1979; S.-W. Kim & Chen, 1990; Nagano et al., 1997). However, they are not preferred by most of the industry. Klein et al. (Klein et al., 2018) worked on the development of two-time-scale (TTS) turbulence models. They mainly focused on linear-eddy viscosity models coupled with TTS. Their findings indicated significant improvements compared to both single and multi-scale models for all of the test cases they performed in the context of an earlier study in which they evaluated different turbulence models for various non-equilibrium flows (Klein et al., 2015). The test cases they chose were:

- Homogeneous shear flows
- Normally strained flows
- Adverse pressure gradient boundary layer flows
- Favorable pressure gradient boundary layer flows
- Oscillatory boundary layer flows
- Fully developed oscillatory flows
- Ramp-up pipe flows
- Steady and pulsated backward facing step flows

In context of their work, they considered thirteen different turbulence models including both single scale and multi scale models, low Reynolds models, LEVMs and NLEVMs making a wide spectrum of models. These models were:

- Chen and Guo (1991) LEVM MTS model (C. P. Chen & Guo, 1991)
- GL Gibson and Launder (1978) RST model (Gibson & Launder, 1978)
- HJ Hanjalic´ et al. (1997) LRN RST model (Hanjalić et al., 1997)
- HLS Hanjalic´ et al. (1980) LEVM MTS model (Hanjalic et al., 1980)
- KC Kim and Chen (1990) LEVM MTS model (S.-W. Kim & Chen, 1990)
- Standard k–ε model with constants of (Launder & Spalding, 1974)
- (Launder & Sharma, 1974) LRN k–ε model
- (Nagano et al., 1997) LRN LEVM MTS model
- (Craft et al., 2000) cubic k–ε model (NLEVM)
- (Speziale et al., 1991) SSG RST model

- (Menter, 1994) SST model
- (Craft, 1998) Two-Component-Limit LRN RST model
- (Wilcox, 1988a) LRN RST MTS model

There are also many other three-equation models as they were stated before. In his article, Goldberg proposed a low Reynolds number extension of the *k*-ε turbulence model. The proposed model has several attributes:

- It does not involve wall distance or normal-to-wall directionality, making it applicable to arbitrary flow topologies.
- It enforces time scale realizability by preventing it from falling below the Kolmogorov (dissipative eddy) scale ($\tau_\eta = (\upsilon/\varepsilon)^{\frac{1}{2}}$).
- It employs a simple wall boundary condition for the dissipation rate of turbulence kinetic energy, ε.

To achieve this, Goldberg introduced an additional transport equation for the undamped eddy viscosity, *R*, resulting in a three-equation model. This modification allows for the model to be pointwise (local) and applicable to arbitrary geometries without the need for explicit wall distance. The proposed model was compared with experimental data of several flow cases, and the results were encouraging, demonstrating the feasibility of this three-equation approach (U. C. Goldberg, 1996).

The research compares velocity, turbulence kinetic energy, and Reynolds shear stress profiles for the turbulent boundary layer on a flat plate with an adverse pressure gradient. When compared to experimental data, the *R*-*k*-ε model yields better predictions than the traditional *k*-ε model. For the second scenario, supersonic ramp flow, the research compares surface pressure, skin friction, and corner velocity profiles. Comparing the *R*-*k*-ε model to experimental data, the new model predicts flow separation better than the classic *k*-ε model. However, skin friction peak post-reattachment differs little. The research finds that the *R*-*k*-ε model proves the three-equation technique is feasible and yields better forecasts than the ordinary *k*-ε model. The paper's quantitative data is particular to the flow scenarios analyzed and may not apply to all flow circumstances.

Another study of Goldberg disclosed a different model that utilizes the same two turbulence quantities, however coupling it with another entity created to solve the issue of turbulence degradation in simulations of CFD. In many instances, the turbulence levels anticipated by traditional k-ε or k-ω closures can decay to the point where laminar flow occurs at the body surface, particularly in subsonic/transonic flows. This is inconvenient from a computational viewpoint, as it requires placing the outer boundary at a large distance from the body to prevent body-induced pressure signals from reaching the outer boundary.

To overcome this issue, the researchers proposed coupling the k-ε model with another type of turbulence closure, the R_t closure, which naturally maintains inflow turbulence levels undecayed all the way to the body. By setting the final eddy viscosity as the maximum of the two models' contributions, a non-decaying eddy viscosity field is obtained.

The objective of designing this model was to provide engineers with a more accurate and efficient technique for simulating exterior flows, in which input turbulence levels are maintained all the way to the body without degrading. This method eliminates the requirement for specific treatment in the formulation of the freestream production term and avoids the restrictions and limitations associated with other methods. The researchers' ultimate objective was to make the computation of such processes simpler and less prone to error for engineers (U. Goldberg et al., 2009).

The authors examined two aerodynamic flow cases in their study. In the first case, a NACA 63210 airfoil was used. The computational domain consisted of a grid with a layer of prisms surrounding the airfoil and triangular elements in the remaining portion of the domain. The far-field boundary was placed 100 cord lengths away from the body. In this case, the flow conditions were stated as M=0.6, Re=1,000,000, and Tu=5%. The authors compared the results obtained using the original k-ε closure with the results obtained using the current three-equation model. To comprehend the differences between the two closure models, they evaluated eddy viscosity contour plots, turbulence kinetic energy at the leading edge, pressure coefficient profiles, and skin friction profiles.

As a summary, in many flow scenarios of technical importance, it is easier to estimate turbulence levels near aerial vehicles than far upstream. In order to avoid body-induced

pressure signals from reaching the outer boundary, the computational domain must frequently be extended well upstream of the body. As a result, turbulence levels predicted using k-ε or k-ω closures may diminish or perhaps vanish entirely before the body is reached. In contrast, the k-ε-R_t turbulence closure examined in this paper maintains turbulence levels from the inlet to the body. This makes it a useful turbulence closure for a wide variety of external aerodynamic flow problems. The k-ε-R_t model ensures that turbulence levels in the region of the flight vehicle do not diminish and remain constant. This is essential for correct estimates of aerodynamic forces like lift and drag.

Cotton and Ismael (Cotton & Ismael, 1998) also introduced a third equation for the so called 'transported strain parameter', (S) in their model together with the k and ε equations and employed a dumping function in the turbulence viscosity relation that is predominantly influenced by Billard and Lawrence (Billard & Laurence, 2012) who provide a twenty-year evolution of the k-ε-v^2 type of three-equation models focusing on the variance of wall-normal fluctuating velocity and its source "f" in their paper.

To estimate the aerodynamic performance of iced airfoils, Li, Zhang, and Chen developed a modified three-equation turbulence model in their research (Li et al., 2020). As ice formation on a wing can severely degrade its aerodynamic performance and represent a hazard to aircraft safety, this model was designed to precisely predict the stalling behavior of frozen airfoils. The original model that they started working on was of Lopez and Walters' $k - \overline{v^2} - \omega$ (Lopez & Walters, 2016). The improvements Li et al. made were intended to calibrate the transitional behavior and enhance the performance of the non-equilibrium state.

The rationale behind their model is to accurately simulate complex flow phenomena such as laminar separation, shear layer transition, and turbulent reattachment, which are crucial for predicting the stall behavior of iced airfoils. The authors implemented their modified model using a linear eddy viscosity transition model as a baseline and made specific modifications to calibrate the transition behavior and improve the nonequilibrium performance. They calibrated the model based on two test cases, a clean airfoil (NACA23012) and an iced airfoil (GLC305 with ice shape 944). The modifications included adjusting parameters for turbulent reattachment prediction, and predicting the transition process inside the separation region.

The relative errors of the predicted maximum lift coefficients of the iced airfoils were approximately 5% of the experimental values. The authors concluded that their modified three-equation turbulence model showed considerable improvement in predicting the lift coefficient of iced airfoils compared to existing turbulence models. They also highlighted the importance of accurately describing the flow features to yield acceptable results for the stall behavior of iced airfoils. Researchers evaluated the model on several airfoils, including clean airfoils and three types of iced airfoils (horn ice, streamwise ice, and spanwise-ridge ice). In estimating the aerodynamic performance of iced airfoils, the Separation-Modified Production-to-Dissipation Ratio (SPF) model of Li et al. performs pretty well compared to other turbulence models. The SPF model achieved the best results in terms of the highest lift coefficient, with relative errors of approximately 5 percent. This model was a significant improvement over the others. In contrast, the *SST* k-ω model has significantly bigger errors of 20-60%, but the original k-ε model yields relatively lesser errors of 10-40%.

Considering recent studies, Nowruzi et al. conducted a successful study on the integration of CFD and ANN for analyzing airfoil simulations in both 2D and 3D scenarios (Nowruzi et al., 2017). Thuerey et al. employed CNN to estimate velocity and pressure distributions by utilizing the Spalart-Allmaras (SA) model on airfoils (Thuerey et al., 2020). Sun et al. carried out an ANN analysis utilizing data from the SA turbulence model. They combined the ANN with the Discontinuous-Galerkin (DG) method. According to their statement, the coupling of DG and ANN is a reliable technique that ensures consistent convergence, as opposed to the coupling of DG and SA (Sun et al., 2019). Using SA-trained ANN for a variety of flows, Tracey et al. developed a novel machine learning (ML) algorithm for low-fidelity turbulence models, which also covers combustion models (Tracey et al., 2013).

The authors (Molchanov & Bykov, 2013) suggested a turbulence model, an explicit algebraic stress model (EASM), for compressible high-velocity flows. Modeling of the rapid component of the pressure-strain correlation, which is dependent on the turbulent Mach number, forms the basis of the model. For instance, they discussed the work of Park and Park (Park & Park, 2005), who introduced the notion of shifting equilibrium to modify the linear pressure strain term in homogeneous shear flow. They also highlighted the research conducted by Gomez and Girimaji (Gomez & Girimaji, 2011), who

concluded that the impact of compressibility on turbulence is reflected mostly by the fast portion of the pressure-strain correlation. The model sought to provide explicit formulas for each element of the Reynolds stress tensor, presuming that velocity fluctuations normal to the streamline play a crucial role in the mechanism of turbulent mixing. Moreover, the authors analyzed the findings of rapid distortion theory (RDT) research, which indicated that the effect of pressure on turbulence varies with Mach number. At low velocities, pressure imposes incompressibility, which can be modeled using the conventional incompressible pressure-strain correlation. At intermediate Mach numbers, the magnitudes of the inertial and pressure terms were comparable, resulting in the stabilization of the turbulent kinetic energy growth rate. At extremely high Mach numbers, pressure becomes insignificant in comparison to inertial terms. In addition, the authors sought to construct a flexible model applicable to both free shear flows (such as jets and mixing layers) and near-wall flows.

The key aspects of the turbulence model developed in the paper are as follows:

- Modeling of the rapid part of pressure-strain correlation: The model concentrates on capturing the rapid part of the pressure-strain coupling, which is crucial for high-velocity compressible flows. To effectively describe turbulence properties in these flows, the model considers the turbulent Mach number.

- Explicit formulas for Reynolds stress tensor components: The model provides explicit formulas for each Reynolds stress tensor component. It implies that velocity fluctuations perpendicular to the streamline play a significant role in the turbulent mixing process. By explicitly computing these components, the model tries to increase the precision with which turbulent flows are predicted.

- Applicability to both free shear flows and near-wall flows: The model is intended to be flexible and adaptable to both free shear flows (including jets and mixing layers) and near-wall flows. This enables for a vast array of applications and makes the model applicable in numerous circumstances.

The researchers evaluated their approach using a variety of benchmark scenarios. Here are the illustrative cases addressed in the text:

- The researchers compared their model to experimental data from Goebel, and Dutton (Goebel & Dutton, 1991), and another scientific study about high-velocity plane mixing layers. The experimental apparatus consisted of a two-dimensional mixing layer with two incoming streams that were separated by a splitter plate. In terms of freestream velocity ratios, freestream density ratios, and relative Mach numbers, the operating parameters for the seven examined examples differed.
- Cold under-expanded and over-expanded air jets: Using experimental data from Safronov and Khotulev (Safronov & Khotulev, 2008), the researchers verified their model for under-expanded and over-expanded air jets. Air jets with an overall temperature of 300 K and a nozzle exit Mach number of 3.3 were simulated. Experimental data and simulation results were compared for an under-expanded jet with a static pressure ratio of 1.5, a profiled nozzle diameter of 53.7 mm, and a nozzle exit half cone angle of 10 degrees.
- Hypersonic compression ramp: The researchers simulated the flow along a 34^{o} compression ramp using the same input parameters as the reference tests. The simulation was performed for an open-jet test flow of Mach-9 nitrogen gas. For various scenarios, including the existence of fuel injection, the simulation results were compared to experimental data.
- Base-Bleed Experiments with a Cylindrical Afterbody in Supersonic Flow: The authors simulated the flow over a cylindrical afterbody in supersonic flow using their turbulence model, comparing simulated results to available experimental data.
- Dual-mode scramjet/ramjet combustor: The researchers also assessed their model on a dual-mode scramjet/ramjet combustor. The purpose of the simulation was to examine the vitiation effects on a hydrogen-powered scramjet. The outcomes were compared to earlier numerical simulations.

On the other hand, in one of the recent studies, Weatheritt et al. utilized gene-expression programming (GEP) to create EASM on Pope's proposed method of stress tensor decomposition. The representation of turbulence closures similar to EASM is in the form:

$$a_{ij} = \sum_{k} \mathrm{f}^{(k)}(I_1, I_2, I_3, \ldots, I_n) V_{ij}^{k} \tag{1.2}$$

The non-dimensional anisotropic stress tensor, denoted as a_{ij} is expressed as a linear combination of tensor bases V_{ij}^{k} and scalar invariants I_j. Research has demonstrated that models derived from EASM equations can be explicitly constructed using symbolic regression through GEP, which is employed to ascertain the coefficients, $\mathrm{f}^{(k)}$ from training data. Implementing these GEP-trained models in RANS solvers has shown enhanced predictive precision in many applications, including rectangular duct and turbomachinery flows. However, the literature also emphasizes that the fundamental discrepancy between RANS modeling and high-fidelity data is frequently overlooked, indicating that RANS predictions may still be insufficient even when Reynolds stresses obtained from DNS are used in CFD calculations.

Also, there are experimental studies considered to be the fundamental or essential works related to turbulence topics. In one of them, Heskestad presented the results of hot-wire measurements in a plane-jet using air as the fluid. Moreover, he had investigated the effect of jet speed on turbulence intensity at the centerline. He had discovered that the mean of velocities and square of streamwise turbulent velocity were nearly self-preserving for downstream of the flow at which energy balance were obtained about x/d=65. (Heskestad, 2011). He also mentioned that the dissipation term had not reached self-preserving state till x/d>100. Ramaprian et al. carried out a similar study focusing on turbulent jets in plane-jet type flows for both heated and isothermal cases. They utilized a two-component Laser Doppler Anemometry (LDA) coupled with resistance type thermometry for the measurements. They had observed lower fluxes and turbulence intensities compared to hot-wire studies in the literature (Ramaprian & Chandrasekhara, 2009). They had verified the previous studies when they considered the mean entities. On the other hand, they stated that turbulent fluxes and velocities are below the levels of hot-wire data.

The authors reported that numerical predictions of turbulent impinging jets discharged from a circular pipe were measured by Cooper et al. (Cooper et al., 1993) and Baughn and Shimizu (Baughn & Shimizu, 1989). Additionally, Craft et al. presented an evaluation of four turbulence models in terms of performance (Craft et al., 1993). They included one k-eddy viscosity model and three second-moment closures. The test instances chosen

placed the jet discharge at two and six diameters above a planar surface orthogonal to the jet's axis. The Reynolds values were 2.3×10^4 and 7×10^4, respectively, with the flow completely formed at the discharge plane.

According to the numerical predictions from an upgraded version of the finite-volume code, the k-model and one of the Reynolds stress models produced far too much turbulence at the stagnation point. This excessive energy led to high heat transfer coefficients and turbulent mixing with the surrounding fluid. On the other hand, the other two second-moment closures, which employed new techniques to account for the wall's effect on pressure fluctuations, performed much better. One of them clearly outperformed the others in accounting for the effects of the jet discharge's height above the plate.

However, none of the approaches completely predicted the effects of Reynolds number. The authors believed that the primary source of this failure was the two-equation eddy viscosity technique employed in all cases to bridge the near-wall sublayer, rather than the outer layer models on which the current study had concentrated. They studied numerical predictions from an upgraded version of a finite-volume code, which indicated that the k-model and one of the Reynolds stress models produced far too much turbulence at the stagnation point. Conversely, the other two second-moment closures, which used new techniques to account for the wall's effect on pressure fluctuations, performed much better.

2. MATHEMATICAL MODEL

This chapter comprehensively explains the actions taken in the study, the handling of the simulation process, and the parameters utilized.

2.1. Navier-Stokes Equations

The Navier-Stokes equations describe the fundamental laws governing the motion of fluid substances. They are a set of nonlinear partial differential equations that define the conservation of mass and momentum within a continuous fluid medium. These equations are derived from the basic principles of conservation of mass and Newton's second law of motion applied to a fluid element.

2.1.1. Conservation of Mass

Conservation of mass corresponds to the summation of the change in density over time and the net mass flow across the boundaries of the control volume by convection.

The continuity equation represents the conservation of mass for an incompressible fluid:

$$\frac{\partial \rho}{\partial t} + \nabla \cdot (\rho \boldsymbol{u}) = S_M \tag{2.1}$$

where ρ is the fluid density, t denotes time, $\boldsymbol{u}$ is the velocity vector, $\nabla \cdot$ represents the divergence operator.

2.1.2. Conservation of Momentum

Conservation of momentum can be identified as the summation of the change of velocity with time and convective term on one side, which equals to the summation of pressure gradient, diffusion term, body force term and the other source terms on the other side of the equation.

The Navier-Stokes equations describe the conservation of momentum for a fluid element in three dimensions and in the absence of external forces, where viscosity is the dominant force:

$$\frac{\partial \rho \boldsymbol{u}}{\partial t} + \boldsymbol{u} \cdot \nabla \boldsymbol{u} = -\nabla p + \mu \nabla^2 \boldsymbol{u} - \nabla \boldsymbol{u}' \boldsymbol{u}' + \rho g + S \tag{2.2}$$

where p is the pressure, μ is the molecular viscosity, g represents the gravitational force, S denotes the source terms.

This equation states that the change in momentum of a fluid element equals the sum of the pressure gradient, viscous forces, and gravitational forces acting on it.

Incompressible Navier-Stokes Equations:

The incompressible form of the Navier-Stokes equations is derived under the assumption that the fluid density (ρ) is constant, implying that the fluid is incompressible. The equations are as follows:

The continuity equation (mass conservation):

$$\nabla \cdot \boldsymbol{u} = 0 \tag{2.3}$$

The momentum equations (Newton's second law for fluid motion):

$$\frac{\partial \boldsymbol{u}}{\partial \mathrm{t}} + (\boldsymbol{u} \cdot \nabla)\boldsymbol{u} = -\frac{1}{\rho}\nabla \mathrm{p} + \nu\nabla^2\boldsymbol{u} + \mathrm{g} \tag{2.4}$$

where $\boldsymbol{u}$ represents the velocity vector, t is time, p denotes the pressure ν is the kinematic viscosity, g is the acceleration due to gravity.

$$\frac{\partial u_i}{\partial t} + \frac{\partial (u_i u_j)}{\partial x_j} = -\frac{1}{\rho}\frac{\partial p}{\partial x_i} + \frac{\partial}{\partial x_j}\left[\nu\left(\frac{\partial u_i}{\partial x_j} + \frac{\partial u_j}{\partial x_i}\right)\right] \tag{2.5}$$

Solving the Navier-Stokes equations numerically often involves discretization techniques (like finite difference, finite volume, or finite element methods) to approximate the continuous equations. CFD simulations utilize these discretized equations to predict the flow behavior in various engineering applications.

The Navier-Stokes equations govern a wide range of fluid flow behaviors but solving them analytically is usually limited to idealized cases. For complex and practical scenarios, numerical solutions are employed, considering turbulence, boundary effects, and other complexities using computational methods.

2.2.Reynolds-Averaged Navier-Stokes (RANS) Models: Concept and Principles

The RANS equations constitute a fundamental approach in CFD to model turbulent flows. The core principle of RANS models involves the application of Reynolds averaging to the governing Navier-Stokes equations, aiming to capture the mean flow behavior and resolve the impact of unresolved turbulent fluctuations.

2.2.1. Concept of Reynolds Averaging

Reynolds averaging is a mathematical technique used to decompose the flow variables into mean and fluctuating components. In a turbulent flow, any flow variable (ϕ) is expressed as the sum of its mean ($\bar{\phi}$) and fluctuating (ϕ') components:

$$\phi = \bar{\phi} + \phi' \tag{2.6}$$

Reynolds averaging is performed by taking a time average over a sufficiently long period, denoted by the angular brackets $\langle\cdot\rangle$:

$$\overline{\phi} = \langle\phi\rangle \tag{2.7}$$

Reynolds Decomposition:

Consider a flow variable ϕ which comprises a mean part denoted by $\overline{\phi}$ and a fluctuating part denoted by ϕ':

$$\phi(\boldsymbol{x}, t) = \overline{\phi(\boldsymbol{x}, t)} + \phi'(\boldsymbol{x}, t) \tag{2.8}$$

Time-Averaging Operation:

Reynolds-averaging involves taking the ensemble average (or time average) of the Navier-Stokes equations to obtain the RANS equations.

For a generic variable ϕ, the time-average is given by:

$$\overline{\phi(\boldsymbol{x}, t)} = \lim_{T\to\infty} \frac{1}{T} \int_{t_0}^{t_0+T} \phi(\boldsymbol{x}, t)dt \tag{2.9}$$

2.2.2. Application to Navier-Stokes Equations

Applying Reynolds decomposition to the Navier-Stokes equations yields the RANS. Below steps show the Reynolds-Averaging process of Navier-Stokes Equations

considering the continuity equation and one component of the momentum equation. For simplicity, only x-component has been presented.

- Step 1: Continuity Equation

$$\frac{\partial \rho}{\partial t} + \frac{\partial (\rho u_i)}{\partial x_i} = 0 \tag{2.10}$$

after Reynolds averaging applied,

$$\frac{\partial \overline{\rho}}{\partial t} + \frac{\partial \overline{(\rho u_i)}}{\partial x_i} = 0 \tag{2.11}$$

- Step 2: Momentum Equation (x-component)

$$\frac{\partial (\rho u_i)}{\partial t} + \frac{\partial \left(\rho u_i u_j\right)}{\partial x_j} = -\frac{\partial p}{\partial x_i} + \frac{\partial \tau_{ij}}{\partial x_j} + \rho g_i \tag{2.12}$$

after Reynolds averaging applied,

$$\frac{\partial \overline{(\rho u_i)}}{\partial t} + \frac{\partial \overline{\left(\rho u_i u_j\right)}}{\partial x_j} = -\frac{\partial \overline{p}}{\partial x_i} + \frac{\partial \overline{\tau_{ij}}}{\partial x_j} + \overline{\rho g_i} \tag{2.13}$$

- Step 3: Velocity Decomposition of the velocity u_i into mean U and fluctuating u_i' components:

$$u_i = U + u_i' \tag{2.14}$$

- Step 4: Product of Fluctuations

For any variable A, the product of fluctuations is expressed as:

$$A_i' B_j' = \overline{A_i' B_j'} + \overline{A_i'} \cdot \overline{B_j'} \tag{2.15}$$

- Step 5: Substitution of the velocity decomposition into the momentum equation and simplify using the product of fluctuations:

$$\frac{\partial \overline{(\rho U + \rho u_i')}}{\partial t} + \frac{\partial \overline{\left(\rho (U + u_i') u_j\right)}}{\partial x_j} = -\frac{\partial \overline{p}}{\partial x_i} + \frac{\partial \overline{\tau_{ij}}}{\partial x_j} + \overline{\rho g_i} \tag{2.16}$$

- Step 6: Reynolds Averaging of Fluctuations

Reynolds averaging of fluctuating quantities $\rho u_i'$ results in zero, assuming that fluctuations are uncorrelated with mean flow:

$$\frac{\partial(\overline{\rho \mathrm{U}})}{\partial t}+\frac{\partial\left(\overline{\rho \mathrm{U} u_j}\right)}{\partial x_j}=-\frac{\partial \overline{p}}{\partial x_i}+\frac{\partial \overline{\tau_{ij}}}{\partial x_j}+\overline{\rho g_i} \tag{2.17}$$

- Final Form of Reynolds-Averaged Equations

After simplification and neglecting terms involving the product of fluctuations, the Reynolds-averaged continuity equation and all components of the momentum equation are obtained:

- Reynolds-Averaged Continuity Equation:

$$\frac{\partial \overline{\rho}}{\partial t}+\frac{\partial(\overline{\rho \mathrm{U}})}{\partial x}+\frac{\partial(\overline{\rho V})}{\partial y}+\frac{\partial(\overline{\rho W})}{\partial z}=0 \tag{2.18}$$

- Reynolds-Averaged Momentum Equations:

$$\frac{\partial(\overline{\rho U})}{\partial t}+\frac{\partial(\overline{\rho U U})}{\partial x}+\frac{\partial(\overline{\rho U V})}{\partial y}+\frac{\partial(\overline{\rho U W})}{\partial z}=-\frac{\partial \overline{p}}{\partial x}+\frac{\partial \overline{\tau_{ij}}}{\partial x}+\overline{\rho g_x} \tag{2.19}$$

$$\frac{\partial(\overline{\rho V})}{\partial t}+\frac{\partial(\overline{\rho \mathrm{U} \mathrm{V}})}{\partial x}+\frac{\partial(\overline{\rho \mathrm{V} \mathrm{V}})}{\partial y}+\frac{\partial(\overline{\rho \mathrm{V} \mathrm{W}})}{\partial z}=-\frac{\partial \overline{p}}{\partial y}+\frac{\partial \overline{\tau_{ij}}}{\partial y}+\overline{\rho g_y} \tag{2.20}$$

$$\frac{\partial(\overline{\rho W})}{\partial t}+\frac{\partial(\overline{\rho \mathrm{U} \mathrm{W}})}{\partial x}+\frac{\partial(\overline{\rho \mathrm{V} \mathrm{W}})}{\partial y}+\frac{\partial(\overline{\rho \mathrm{W} \mathrm{W}})}{\partial z}=-\frac{\partial \overline{p}}{\partial z}+\frac{\partial \overline{\tau_{ij}}}{\partial z}+\overline{\rho g_z} \tag{2.21}$$

2.3.Reynolds Stress Transport (RST)

The Reynolds stress transport equation describes the evolution of the Reynolds stress tensor in a turbulent flow. It is derived by taking the Reynolds averaging of the Navier-Stokes equations and applying some algebraic manipulation. The Reynolds stress transport equation for an incompressible flow can be written as follows (White, 2011):

$$\frac{\partial}{\partial t}(\rho\overline{u_i u_j}) + \frac{\partial}{\partial x_k}(\rho\overline{u_i u_j u_k}) = -\frac{\partial}{\partial x_j}\overline{p} + \frac{\partial}{\partial x_k}\left(\mu\left(\frac{\partial\overline{u_i}}{\partial x_j} + \frac{\partial\overline{u_j}}{\partial x_i}\right) - \frac{2}{3}\mu\frac{\partial\overline{u_k}}{\partial x_k}\delta_{ij}\right) + R_{ij} \quad (2.22)$$

Where ρ is the fluid density, $\overline{u_i u_j}$ represents the Reynolds stress tensor, $\overline{p}$ represents the Reynolds-averaged pressure, μ is the dynamic viscosity of the fluid, R_{ij} represents the Reynolds stress tensor's generation terms, which account for the production and dissipation of turbulent kinetic energy.

The terms on the right-hand side of the equation represent various physical processes:

- Pressure gradient term represents the effect of pressure gradients on the Reynolds stress tensor. It is the contribution of the pressure to the transport of momentum in the flow.
- Viscous diffusion term represents the effect of molecular viscosity on the Reynolds stress tensor. It includes both the diffusion of momentum due to velocity gradients and the dissipation of turbulence through viscous effects.
- Reynolds stress generation term, R_{ij} accounts for the production and dissipation of turbulent kinetic energy. These terms arise due to the interaction between the mean flow and the turbulent fluctuations and often involve nonlinear interactions.

The Reynolds stress transport equation is a fundamental equation in turbulent flow modeling as it provides insights into the transport and redistribution of momentum due to turbulence. It is often solved along with other equations, such as the continuity equation and the turbulent kinetic energy equation, in computational fluid dynamics simulations to predict turbulent flows accurately.

2.3.1. Reynolds Stress Tensor

The Reynolds stress tensor is a key concept in the study of fluid mechanics, particularly in turbulent flow. It represents the additional stresses caused by the turbulent fluctuations in a fluid flow, beyond the stresses present in laminar flow. To understand the Reynolds stress tensor, it's essential to first grasp the concept of Reynolds decomposition.

To derive the Reynolds stress tensor, we can start with the Navier-Stokes equations, which describe the conservation of momentum in a fluid flow. The Navier-Stokes equations in their general vector form are:

$$\frac{\partial u_i}{\partial t} + u_j \frac{\partial u_i}{\partial x_j} = -\frac{1}{\rho}\frac{\partial p}{\partial x_i} + \nu \frac{\partial^2 u_i}{\partial x_j \partial x_j} \tag{2.23}$$

where u_i is the velocity component in the i - direction, p symbolizes the pressure, ρ is the density, ν is the kinematic viscosity, and x_j represents the spatial coordinates.

Decomposing the velocity field into its mean and fluctuating components:

$$u_i = \overline{u_i} + u_i' \tag{2.24}$$

Substituting this decomposition into the Navier-Stokes equations,

$$\frac{\partial}{\partial t}(\overline{u_i} + u_i') + (\overline{u_j} + u_j')\frac{\partial}{\partial x_j}(\overline{u_i} + u_i') = -\frac{1}{\rho}\frac{\partial p}{\partial x_i} + \nu \frac{\partial^2}{\partial x_j \partial x_j}(\overline{u_i} + u_i') \tag{2.25}$$

Expanding and rearranging terms,

$$\begin{aligned} &\frac{\partial \overline{u_i}}{\partial t} + \overline{u_j}\frac{\partial \overline{u_i}}{\partial x_j} + \frac{\partial u_i'}{\partial t} + \overline{u_j}\frac{\partial u_i'}{\partial x_j} + u_j'\frac{\partial \overline{u_i}}{\partial x_j} + u_j'\frac{\partial u_i'}{\partial x_j} \\ &\qquad = -\frac{1}{\rho}\frac{\partial p}{\partial x_i} + \nu \frac{\partial^2 \overline{u_i}}{\partial x_j \partial x_j} + \nu \frac{\partial^2 u_i'}{\partial x_j \partial x_j} \end{aligned} \tag{2.26}$$

After taking the time average of this equation, and since the mean velocity is constant with time, its time derivative becomes zero. Additionally, the time average of the fluctuating velocity terms is zero, since turbulence is characterized by random fluctuations. The convective term $u_j' \frac{\partial \overline{u_i}}{\partial x_j}$ vanishes because the mean velocity is independent of the fluctuating velocity. We are left with the following term, which represents the Reynolds stress:

$$\frac{\partial \tau_{ij}}{\partial x_j} = -\frac{1}{\rho}\frac{\partial \overline{p}}{\partial x_i} + \nu \frac{\partial^2 \overline{u_i}}{\partial x_j \partial x_j} \tag{2.27}$$

where $\tau_{ij} = \overline{u_i' u_j'}$ is the Reynolds stress tensor.

This equation shows that the Reynolds stress arises from the fluctuating velocity components and is a consequence of the turbulent nature of the flow.

2.3.2. Boussinesq's Approximation

The Boussinesq's approximation is a fundamental assumption used in modeling turbulent flows, particularly in the context of incompressible flows. It simplifies the equations of motion by accounting for the effects of turbulence through an additional term in the momentum equation, known as the turbulent viscosity or eddy viscosity (Versteeg & Malalasekera, 2007).

The Boussinesq's approximation introduces the concept of eddy viscosity, denoted by ν_t, which accounts for the turbulent mixing in the flow. It assumes that the turbulent stresses can be related to the mean velocity gradients through a linear relationship similar to that in Newton's law of viscosity:

$$\tau_{ij} = -2\mu_t \overline{S}_{ij} \tag{2.28}$$

where τ_{ij} is the Reynolds stress tensor component, μ_t is the turbulent viscosity (eddy viscosity), $\overline{S}_{ij}$ represents the mean strain-rate tensor, defined as $\overline{S}_{ij} = \frac{1}{2}\left(\frac{\partial \overline{u}_i}{\partial x_j} + \frac{\partial \overline{u}_j}{\partial x_i}\right)$.

This equation expresses how the turbulent stresses τ_{ij} are related to the mean strain rate $\overline{S}_{ij}$ and the turbulent viscosity ν_t.

The Boussinesq's approximation does not provide a direct expression for the turbulent viscosity ν_t. Instead, it is often modeled using turbulence models such as the *k-ε* model or the *k-ω* model. These models include additional equations for *k* (turbulence kinetic energy) and *ε* (dissipation rate), which are solved alongside the equations for the mean flow to determine the turbulent viscosity. In summary, the Boussinesq's approximation simplifies the Navier-Stokes equations by introducing the concept of eddy viscosity to account for turbulent effects. It relates the Reynolds stress tensor to the mean flow and turbulence through a linear relationship, allowing for the modeling of turbulent flows in a computationally efficient manner. However, the determination of the turbulent viscosity requires closure models, which remain an active area of research in fluid dynamics.

2.4.RANS Turbulence Models Used in the Study

In the exploration of fluid dynamics and turbulence, the choice of an appropriate turbulence model plays a pivotal role in obtaining accurate and reliable simulation results. In this study, our focus lies on RANS turbulence models, specifically honing in on widely employed two-equation models documented in the literature. These models, which include but are not limited to the *k-ε,* and *k-ω* formulations, have become cornerstones in simulating turbulent flows. As we delve into the intricacies of RANS turbulence modeling, the spotlight is cast on these popular two-equation models, celebrated for their balance between computational efficiency and capability to capture essential turbulence characteristics across a diverse range of fluid flow scenarios.

2.4.1. *Standard k-ε* Turbulence Model

The ***k-ε*** turbulence model (Launder & Spalding, 1974), first proposed by Launder and Spalding in the 1970s, has become one of the most widely used models in CFD for simulating turbulent flows. This model has undergone several modifications and improvements over the years to enhance its accuracy and applicability.

The original *k-ε* model introduced two transport equations, one for turbulent kinetic energy, *k* and the other for the turbulence dissipation rate, *ε*. This model assumed isotropic turbulence and provided a practical framework for engineering applications.

Many researchers have contributed to and have improved model's capabilities in terms of near-wall treatment and damping functions, the effects of large eddies in turbulent flows, and better resolved compressibility effects (Launder & Sharma, 1974; Rodi, 1993; Rodi & Mansour, 1993; Tahry, 1983).

Model Equations:

- Turbulent Kinetic Energy, *k*-Equation:

$$\frac{\partial(\rho k)}{\partial t}+\frac{\partial\left(\rho u_j k\right)}{\partial x_j}=\frac{\partial}{\partial x_j}\left(\left(\mu+\frac{\mu_t}{\sigma_k}\right)\frac{\partial k}{\partial x_j}\right)+P_k-\rho\varepsilon \qquad (2.29)$$

where ρ is the density, *k* represents turbulent kinetic energy,

- Turbulence Dissipation Rate, ε-Equation:

$$\frac{\partial(\rho\varepsilon)}{\partial t}+\frac{\partial(\rho u_j\varepsilon)}{\partial x_j}=\frac{\partial}{\partial x_j}\left(\left(\mu+\frac{\mu_t}{\sigma_\varepsilon}\right)\frac{\partial\varepsilon}{\partial x_j}\right)+C_{1\varepsilon}\frac{\varepsilon}{k}P_k-C_{2\varepsilon}\rho\frac{\varepsilon^2}{k} \quad (2.30)$$

Here, P_k represents the turbulent kinetic energy production term, μ_t is the turbulent viscosity, and $C_{1\varepsilon}$, $C_{2\varepsilon}$, σ_k, and σ_ε are model constants.

2.4.2. *Realizable k-ε* Turbulence Model

The Realizable *k-ε* turbulence model is a widely used and well-regarded turbulence closure model in CFD. It was developed to address some of the limitations of earlier *k-ε* models, particularly in accurately capturing the behavior of complex turbulent flows.

Unlike the standard *k-ε* model, the Realizable *k-ε* model incorporates additional physics and constraints to ensure that the model's predictions are physically realizable. This means that the model equations respect fundamental principles of turbulence and are consistent with observed turbulent behavior.

One of the key features of the Realizable *k-ε* model is its modification of the turbulent viscosity term, which accounts for the eddy viscosity in the turbulent flow. This modification includes a more accurate representation of the turbulent length scale and incorporates constraints that ensure the model's stability and physical realism.

The Realizable *k-ε* model has been extensively validated against experimental data and has shown improved performance over the standard *k-ε* model, particularly in complex flows with adverse pressure gradients, swirling flows, and separated flows. Its robustness and accuracy make it a popular choice for simulating a wide range of turbulent flows encountered in engineering applications, such as aerospace, automotive, and environmental fluid dynamics.

In Equation (2.31), the first term on the left-hand side (LHS) can be described as the rate of the change in turbulent kinetic energy (TKE), second term on the LHS can be defined as the transport of TKE by convection. The first term on the right-hand side (RHS) represents the transport of TKE by diffusion, P_k demonstrates the production of TKE. P_b symbolizes the production of TKE due to buoyancy, fourth term on the RHS represents

the destruction of TKE, Y_M demonstrates the fluctuating dilatation term. Finally, the last term, S_k is defined as a source term.

Equation (2.32) can be expressed as the rate of change of turbulent dissipation rate (TDR) summation with transport of TDR by convection, which equals to the transport of TDR by diffusion and production of TDR difference by the destruction of TDR.

Realizable k-ε turbulence model, and transport equation for the model are given below:

- k – equation:

$$\frac{\partial}{\partial t}(\rho k) + \frac{\partial}{\partial x_i}(\rho k u_i) = \frac{\partial}{\partial x_j}\left(\frac{\left(\mu + \frac{\mu_t}{\sigma_\varepsilon}\right)\partial k}{\partial x_j}\right) + P_k + P_b - \rho\varepsilon - Y_M + S_k \qquad (2.31)$$

and,

- ε – equation:

$$\frac{\partial}{\partial t}(\rho\varepsilon) + \frac{\partial}{\partial x_i}(\rho\varepsilon u_i) = \frac{\partial}{\partial x_j}\left(\left(\mu + \frac{\mu_t}{\sigma_\varepsilon}\right) + \frac{\partial\varepsilon}{\partial x_j}\right) + \rho C_1 S_\varepsilon - \rho C_2 \frac{\varepsilon^2}{k + \sqrt{\vartheta\varepsilon}} + C_{1\varepsilon}\frac{\varepsilon}{k} C_{3\varepsilon} P_b + S_\varepsilon \qquad (2.32)$$

where,

$$C_1 = \max\left[0.43, \frac{\eta}{\eta + 5}\right] \qquad (2.33)$$

and,

$$\eta = S\frac{k}{\varepsilon}, \qquad (2.34)$$

$$S = \sqrt{2S_{ij}S_{ij}} \qquad (2.35)$$

in Realizable k-ε turbulence model, turbulent (eddy) viscosity can be calculated using the below formula:

$$\mu_t = \rho C_\mu \frac{k^2}{\varepsilon} \qquad (2.36)$$

Due to the realizability of the model, it satisfies the mathematical constraints on Reynolds stresses thoroughly and thus it ensures consistency with turbulent flow physics. It can

also predict the spreading rate for plane and round jets accurately. It has been tested extensively over many types of flows including boundary layer and channel flows, and jets and free flows (T.-H. Shih et al., 1995).

2.4.3. *RNG k-ε* Turbulence Model

The Renormalization Group (RNG) *k-ε* turbulence model is a variant of the traditional two-equation turbulence closure model used in CFD. Developed by Yakhot and Orszag (Yakhot et al., 1992), the RNG *k-ε* model addresses some of the deficiencies of standard *k-ε* models by incorporating additional physics derived from the renormalization group theory.

The RNG *k-ε* model includes a modification to the standard dissipation rate equation, which leads to improved predictions of near-wall flows and separation regions. It also incorporates a dynamic procedure for determining the turbulent length scale, providing better accuracy in complex flows with adverse pressure gradients and swirling motion.

Transport Equations:

The RNG *k-ε* model includes two transport equations for the turbulence kinetic energy (*k*) and the turbulence dissipation rate (*ε*).

- Turbulence Kinetic Energy Equation:

$$\frac{\partial(\rho k)}{\partial t}+\frac{\partial(\rho k u_i)}{\partial x_i}=\frac{\partial}{\partial x_j}\left[\left(\mu+\frac{\mu_t}{\sigma_k}\right)\frac{\partial k}{\partial x_j}\right]+P_k-\rho\varepsilon-\rho\varepsilon_b \tag{2.37}$$

where P_k represents the production of turbulence kinetic energy, μ_t is the turbulent viscosity, σ_k is a model constant, and ε_b is a damping term.

- Turbulence Dissipation Rate Equation:

$$\frac{\partial(\rho\varepsilon)}{\partial t}+\frac{\partial(\rho\varepsilon u_i)}{\partial x_i}=\frac{\partial}{\partial x_j}\left[\left(\mu+\frac{\mu_t}{\sigma_\varepsilon}\right)\frac{\partial\varepsilon}{\partial x_j}\right]+C_{\varepsilon1}\frac{P_k}{k}\varepsilon-C_{\varepsilon2}\frac{\rho\varepsilon^2}{k}+\rho\varepsilon_b \tag{2.38}$$

where $C_{\varepsilon1}$ and $C_{\varepsilon2}$ are model constants, and ε_b is a damping term.

Turbulent Viscosity:

The turbulent viscosity is determined using the eddy viscosity concept and is defined as:

$$\mu_t = \rho C_\mu \frac{k^2}{\varepsilon} \tag{2.39}$$

where C_μ is a model constant.

2.4.4. *k-ω* Turbulence Model

The *k-ω* turbulence model is a prevalent two-equation turbulence model, created by Wilcox in 1988 (Versteeg & Malalasekera, 2007) and revised in 2006 (Wilcox, 2006). This model is employed for simulating turbulent flows, especially in near-wall regions, where it frequently surpasses other models such as the *k-ε* model. The model utilizes two transport equations: one for turbulent kinetic energy (*k*) and another for the specific dissipation rate (*ω*). These equations assist in calculating turbulent viscosity and simulating turbulent flow dynamics.

The *k-ω* model is formulated to rectify the shortcomings of the *k-ε* model, especially in forecasting boundary layer flows in the presence of adverse pressure gradients and flow separation. It has gained popularity for its capacity to deliver precise outcomes for intricate boundary layers, particularly adjacent to walls, without necessitating further dampening operations.

The primary equations governing the *k-ω* model are the transport equations for *k* and *ω*:

- Turbulence Kinetic Energy (*k*) Equation:

$$\frac{\partial k}{\partial t} + U_j \frac{\partial k}{\partial x_j} = P_k - \beta^* k\omega + \frac{\partial}{\partial x_j}\left[(\nu + \sigma_k \nu_t)\frac{\partial k}{\partial x_j}\right] \tag{2.40}$$

where, k is the TKE, U_j represents the mean velocity component in the j direction, P_k denotes the production of TKE, β^* is a model constant, ω symbolizes the specific dissipation rate, ν is the kinematic viscosity, and ν_t is the turbulent viscosity. σ_k is the turbulent Prandtl number for k.

- Specific Dissipation Rate (ω) Equation:

$$\frac{\partial \omega}{\partial t} + U_j \frac{\partial \omega}{\partial x_j} = \alpha \frac{\omega}{k} P_k - \beta \omega^2 + \frac{\partial}{\partial x_j}\left[(\nu + \sigma_\omega \nu_t)\frac{\partial \omega}{\partial x_j}\right] \quad (2.41)$$

where, α, and β are model constants. σ_ω is the turbulent Prandtl number for ω.

Production of Turbulence Kinetic Energy (P_k):

$$P_k = \tau_{ij} \frac{\partial U_i}{\partial x_j} \quad (2.42)$$

where, τ_{ij} represents the Reynolds stress tensor, ($\frac{\partial U_i}{\partial x_j}$) denotes the mean velocity gradient.

The turbulent viscosity (ν_t) is calculated using:

$$\nu_t = \frac{k}{\omega} \quad (2.43)$$

This relationship helps link the turbulence kinetic energy and the dissipation rate directly to the flow's eddy viscosity, influencing the momentum equations.

Model Constants:

The standard constants for the k-ω model as per (Wilcox, 2006) are given in **Table 2.1**:

Table 2.1. *k-ω* turbulence model constants

β^*	α	β	σ_k	σ_ω
0.09	5/9	0.075	0.5	0.5

The *k-ω* model involves other versions, notably the SST (Shear Stress Transport) model, which integrates the *k-ω* model in the near-wall region with the k-ε model in the outer region to optimize their respective advantages.

The *k-ω* model is widely used in aerospace, automotive, and marine applications, where accurate boundary layer predictions are crucial for performance and safety.

2.4.5. *SST k-ω* Turbulence Model

The Shear Stress Transport (SST) *k-ω* turbulence model is a popular choice in CFD for simulating turbulent flows, particularly in aerodynamics and turbomachinery applications. It combines elements of both the *k-ω* and *k-ε* models to provide accurate predictions across a wide range of flow regimes, including boundary layers, separated flows, and transitional flows.

The SST *k-ω* model addresses some of the limitations of the standard *k-ω* model near solid walls, where it can be prone to numerical instability and inaccurate predictions. By incorporating a blending function that smoothly transitions between the *k-ω* and *k-ε* formulations, the SST model provides improved accuracy and robustness, especially in adverse pressure gradient regions and near-wall flows.

Transport Equations:

The SST *k-ω* model includes transport equations for both *k* and *ω*:

- Turbulence Kinetic Energy Equation:

$$\frac{\partial(\rho k)}{\partial t} + \frac{\partial(\rho k u_i)}{\partial x_i} = P_k - \beta^* \rho k \omega + \frac{\partial}{\partial x_j}\left[(\mu + \sigma_k \mu_t)\frac{\partial k}{\partial x_j}\right] \quad (2.44)$$

where P_k represents the production of turbulence kinetic energy, β^* is the beta-star term, μ_t is the turbulent viscosity, and σ_k is a model constant.

- Turbulence Specific Dissipation Rate Equation:

$$\frac{\partial(\rho \omega)}{\partial t} + \frac{\partial(\rho \omega u_i)}{\partial x_i} = \frac{\alpha}{\omega} P_k - \beta \rho \omega^2 + \frac{\partial}{\partial x_j}\left[(\mu + \sigma_\omega \mu_t)\frac{\partial \omega}{\partial x_j}\right] \quad (2.45)$$

where P_k is again the production of turbulence kinetic energy, α and β are model constants, and σ_ω is another model constant.

Turbulent Viscosity:

The turbulent viscosity in the SST *k-ω* model is determined using a blending function that smoothly transitions between the *k-ω* and *k-ε* formulations based on the distance to the nearest wall. Near-wall regions, where the *k-ω* model is prone to errors, the model switches to a *k-ε* formulation to improve accuracy and stability.

Blending Function (F_1):

$$F_1 = \tanh\left(\left(\frac{\beta^* \omega}{\widehat{S}}\right)^2\right) \tag{2.46}$$

where $\widehat{S}$ is a modified local strain rate.

3. NUMERICAL MODEL AND SOLUTION PROCEDURE

Constructing and solving numerical models in CFD involves several key steps to accurately capture the complex behavior of turbulent flows and other flow phenomena.

The first step in constructing a CFD model is to define the problem to be solved. This includes specifying the geometry of the domain, boundary conditions, fluid properties, and any other relevant parameters. For turbulent flows, the choice of turbulence model and initial conditions are critical.

Once the problem is formulated, the computational domain needs to be discretized into a grid or mesh. The grid should be structured or unstructured, depending on the complexity of the geometry and flow features. For turbulent flows, the grid resolution near walls and other regions of interest is crucial for capturing boundary layer effects and turbulent structures accurately.

The governing equations of fluid flow, typically the Navier-Stokes equations, need to be discretized to solve them numerically. This involves expressing the equations in a form suitable for solution on a discrete grid, commonly using finite difference, finite volume, or finite element methods. For turbulent flows, additional equations for turbulence quantities, such as k and ω, are included based on chosen turbulence models.

Turbulence models are essential for simulating turbulent flows in CFD. Various turbulence models, such as k-ε, k-ω, and LES are available, each with its assumptions and complexities. The choice of turbulence model depends on the flow regime, computational resources, and accuracy requirements.

The continuous governing equations are discretized using numerical methods to obtain algebraic equations suitable for solution on a computer. This step involves approximating spatial derivatives using finite differences, finite volumes, or finite elements and integrating the equations over the discretized control volumes or elements.

The discretized equations are typically solved iteratively using numerical solution algorithms such as the SIMPLE algorithm for steady-state problems or the PISO algorithm for unsteady problems. These algorithms iterate between velocity and pressure corrections until a converged solution is obtained.

Appropriate boundary conditions are applied to the numerical model to represent the physical conditions at the boundaries of the computational domain accurately. These boundary conditions may include specified velocities, pressures, temperatures, or other quantities, depending on the problem.

The solution process begins by initializing the flow field with an initial guess or solution. For turbulent flows, the initial conditions often include estimates of turbulence quantities based on empirical correlations or physical considerations.

The discretized equations are solved numerically using iterative solvers to obtain the velocity, pressure, and other flow variables at each grid point or element. The solution procedure involves iterating until a converged solution is achieved, where the residual errors are below a specified tolerance.

Once the numerical solution is obtained, post-processing and analysis techniques are applied to interpret and visualize the results. This may include generating flow visualizations, calculating flow quantities of interest (e.g., forces, heat transfer rates), and comparing the results to experimental data or analytical solutions for validation.

Finally, the numerical results are validated and verified against experimental data or other benchmark solutions to assess the accuracy and reliability of the numerical model. This process helps ensure that the model provides physically realistic predictions and can be trusted for engineering analysis and design (Moukalled et al., 2016).

3.1.Discretization Methods

In CFD, discretization methods are used to approximate the partial differential equations governing fluid flow on a discrete grid or mesh. The choice of discretization method can significantly impact the accuracy, stability, and computational efficiency of the numerical solution. Here are some widely used discretization methods along with their equations (Tannehill et al., 2013):

- *Finite Difference Method (FDM):* In the finite difference method, derivatives in the governing equations are approximated using finite difference formulas. For example, the first-order central difference approximation for the spatial derivative of a function (f) with respect to x is given by:

$$\frac{\partial f}{\partial x} \approx \frac{f_{i+1} - f_{i-1}}{2\Delta x} \tag{3.1}$$

Similarly, the second-order central difference approximation for the second derivative is:

$$\frac{\partial^2 f}{\partial x^2} \approx \frac{f_{i+1} - 2f_i + f_{i-1}}{(\Delta x)^2} \tag{3.2}$$

where f_i represents the value of f at grid point i and Δx is the grid spacing.

- *Finite Volume Method (FVM):* In the finite volume method, the governing equations are integrated over control volumes or cells in the computational domain. The fluxes across the faces of each control volume are calculated based on the spatial gradients of the flow variables. The discretized form of the conservation equations for a control volume (V) can be written as:

$$\frac{d}{dt}\int_V \rho dV + \oint_S \rho u \cdot n dS = 0 \tag{3.3}$$

where ρ is the density, u is the velocity vector, V is the control volume, S is the surface of the control volume, and n is the outward unit normal vector.

- *Finite Element Method (FEM):* In the finite element method, the computational domain is discretized into elements, and the governing equations are approximated by piecewise polynomial interpolations within each element. The weak form of the governing equations is derived by multiplying the equations by suitable weight functions and integrating over the domain. For example, the weak form of the Poisson equation $\nabla^2\phi = f$ can be written as:

$$\int_\Omega \nabla\phi \cdot \nabla v \, d\Omega = \int_\Omega f v \, d \tag{3.4}$$

where ϕ is the solution variable, f is a given function, and v is a test function.

Depending on the specific problem and requirements, variations and combinations of these methods, such as high-order schemes, upwind schemes, and hybrid methods, may be employed to achieve desired accuracy and efficiency in numerical simulations.

3.2.Simulation Parameters

The study involved conducting simulations to evaluate the efficacy of a newly created turbulence model in comparison to established models and experimental data from current literature. The simulations concentrated on two specific flow patterns: free-shear jets and wall-bounded flows. The parameters utilized in these simulations are outlined below.

The fluid considered in the simulations is assumed to be incompressible and Newtonian. Density (ρ) and dynamic viscosity (μ) of the fluid are specified based on the fluid being simulated (e.g., air, water).

For free-shear jets, the geometric configuration typically includes a nozzle orifice from which the jet issues into a quiescent ambient fluid. For wall-bounded flows, the geometry comprises solid walls confining the flow, such as a channel or boundary layer setup. Geometric dimensions, such as the diameter of the nozzle, channel height, and length scales, are specified based on the specific configuration being simulated.

For free-shear jets, the inlet boundary condition involves prescribing the velocity profile and turbulence characteristics at the nozzle exit. For wall-bounded flows, the boundary conditions include specifying the velocity profile and turbulence quantities at the inlet, as well as no-slip conditions on the walls. Appropriate boundary conditions are also set at the outlet to ensure the conservation of mass and momentum.

The newly developed turbulence model, along with established turbulence models (e.g., k-ε, *SST* k-ω), are employed to simulate turbulence in the flow. Model-specific parameters, such as k and its dissipation, ε, are specified according to the turbulence model being used.

CFD simulations are performed using a finite volume method. Spatial discretization is achieved through structured or unstructured grids, depending on the complexity of the geometry.

Solver settings, including convergence criteria and iteration schemes, are adjusted to ensure accurate and efficient simulation results.

The simulation domain encompasses the entire flow region of interest, extending sufficiently upstream and downstream to minimize boundary effects.

Grid resolution is carefully chosen to capture the relevant flow features and turbulence scales accurately.

Experimental data from the literature, including velocity profiles, turbulence intensity profiles, and other relevant quantities, are used for comparison and validation of the simulation results.

By carefully controlling and specifying these simulation parameters, the study aims to provide a comprehensive comparison between the newly developed turbulence model and existing models, as well as experimental data, in both free-shear jets and wall-bounded flows.

3.3.Solution Procedure

Throughout whole study, all the simulations have been carried out using the SIMPLE (Semi-Implicit Method for Pressure-Linked Equations) algorithm.

The SIMPLE algorithm is widely used in CFD to solve the Navier-Stokes equations for incompressible flows, particularly for pressure-velocity coupling. This algorithm ensures a consistent and stable solution by decoupling pressure and velocity calculations and iterating until convergence is achieved. Here are the detailed steps of the SIMPLE algorithm:

Step 1: Initialization

- Start by initializing the flow field variables such as velocity components (u, v, w), pressure (p), and turbulence properties (k, ε, ω, …), if using turbulence models).
- Set convergence criteria (e.g., residual tolerances) for iterative convergence checks.

Step 2: Predictor Step - Velocity Calculation

- *Velocity Prediction*:
  - Initialize a tentative velocity field (u^*, v^*, w^*) based on the previous time step or initial conditions.

- Discretize the momentum equations (Navier-Stokes) without the pressure term to predict the tentative velocities:

$$\frac{\partial u^*}{\partial t} + \left(u\frac{\partial u}{\partial x} + v\frac{\partial u}{\partial y} + w\frac{\partial u}{\partial z}\right) = -\frac{1}{\rho}\frac{\partial p}{\partial x} + \nu\nabla^2 u \tag{3.5}$$

(Similarly, for $v^*$and w^* equations).

- *Velocity Corrections*:
  - Compute the velocity corrections ($\delta u, \delta v, \delta w$) from the tentative velocities to satisfy the continuity equation.

Step 3: Pressure Correction

- *Pressure Correction Equation*:

Formulate a pressure correction equation to enforce mass conservation (Poisson equation) derived from the continuity equation:

$$\frac{\partial^2 p}{\partial x^2} + \frac{\partial^2 p}{\partial y^2} + \frac{\partial^2 p}{\partial z^2} = \frac{\rho}{\Delta t}\left(\frac{\partial u^*}{\partial x} + \frac{\partial v^*}{\partial y} + \frac{\partial w^*}{\partial z}\right) \tag{3.6}$$

- *Pressure Update*:
  - Correct the pressure field (p') using the pressure correction equation.
  - Update the pressure field (p) by adding the pressure correction (p').

Step 4: Velocity Correction

- *Velocity Field Update*:
  - Update the velocity field (u, v, w), using the velocity corrections ($\delta u, \delta v, \delta w$) calculated previously.

Step 5: Convergence Check

- Check for convergence by calculating residuals (e.g., based on changes in velocity or pressure values) against predefined convergence criteria.

If convergence criteria are not met, return to Step 2 and iterate until convergence is achieved.

3.4.Wall Treatment

Wall functions are an integral part of CFD, particularly in simulating turbulent flows near solid boundaries. These functions provide an efficient and accurate way to model the boundary layer near walls without resolving the near-wall region explicitly, significantly reducing computational costs.

In many engineering applications, such as aerodynamics, heat transfer, and turbomachinery, flows occur in the presence of solid boundaries, leading to the formation of thin boundary layers near the walls. These boundary layers are dominated by viscous effects and turbulence, making them computationally expensive to resolve fully. Wall functions provide an alternative approach to model these boundary layers accurately while minimizing computational resources.

Wall functions exploit the behavior of turbulent flows near walls, where the velocity and temperature profiles exhibit universal behavior known as the "law of the wall." This law describes the logarithmic variation of velocity and temperature with distance from the wall. Wall functions approximate these logarithmic profiles to calculate velocity and temperature values at grid points near the wall without solving the governing equations directly in the near-wall region.

The law of the wall is a fundamental concept in boundary layer theory that describes the behavior of velocity and shear stress near a solid boundary in a turbulent flow. It states that the velocity profile in the turbulent boundary layer exhibits a logarithmic variation with distance from the wall. The law of the wall provides a key insight into the near-wall flow behavior, enabling accurate modeling of turbulent boundary layers using wall functions in CFD.

The dimensionless variables u^+ and y^+ are defined as:

$$u^+ = \frac{u}{u_\tau}, \quad y^+ = \frac{y u_\tau}{\nu} \tag{3.7}$$

where u is the velocity at distance y from the wall, u_τ is the friction velocity, defined as $u_\tau = \sqrt{\tau_w/\rho}$, τ_w is the wall shear stress, ν is the kinematic viscosity of the fluid.

The friction velocity u_τ characterizes the shear stress at the wall and serves as a characteristic velocity scale for the near-wall flow. The dimensionless distance y^+ measures how far a point is from the wall in terms of the viscous length scale, and u^+ represents the velocity normalized by the friction velocity. The law of the wall states that the dimensionless velocity u^+varies logarithmically with the dimensionless distance y^+ from the wall, with the von Kármán constant κ determining the slope of the logarithmic profile. The integration constant B represents the intercept of the velocity profile with the wall.

Figure 3.1 illustrates the division of the near-wall region into three sections: the viscous sub-layer, the buffer layer, and the logarithmic zone. These sections are as follows:

- The viscous sub-layer ($y^+ < 1$)

In the viscous layer, the fluid is primarily influenced by viscous effects, allowing for the assumption that the shear stress of the fluid equals the wall shear stress τ_w. Viscous stress determines the flow in the viscous layer, resulting in a linear velocity profile.

$$u^+ = y^+ \tag{3.8}$$

- Logarithmic area ($30 < y^+ < 200$)

Turbulence stress dominates the flow in the logarithmic layer, and the velocity profile changes gradually with a logarithmic function as distance y increases.

$$u^+ = \frac{1}{\kappa}\ln(Ey^+) \tag{3.9}$$

where κ represents the von Karman constant which is 0.41, and E is equal to 9.8 for the smooth walls. The red line in **Figure 3.1** illustrates the logarithmic correlation in the logarithmic region.

- Buffer Layer

Viscous and turbulent stresses are comparable in strength, and due to the intricate velocity profile being undefined, the original wall functions exclude the initial cell center in this area. The enhanced wall functions enable the first cell center to be positioned in the buffer layer. The buffer layer in OpenFOAM is broken into two parts. One method utilizes a

linear relation similar to the viscous sublayer, while the second method employs a logarithmic function akin to the logarithmic region.

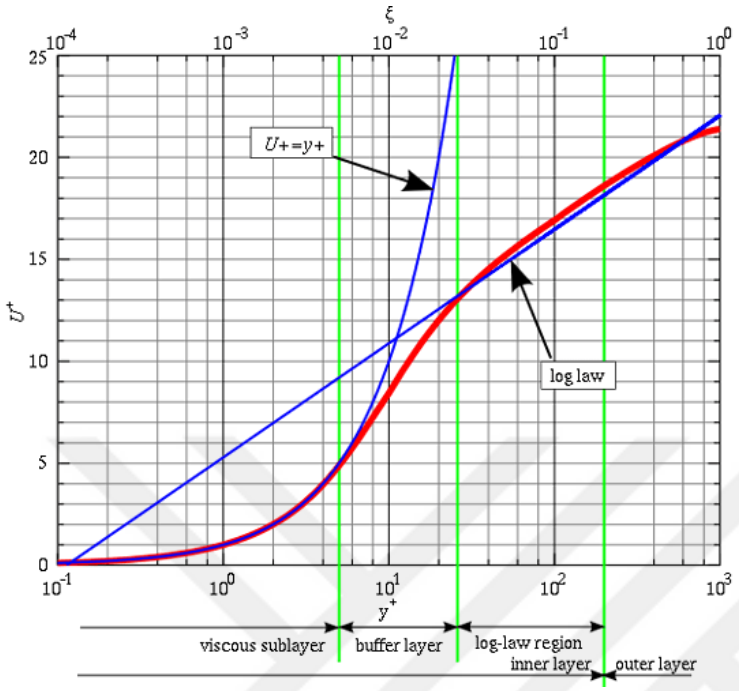

Figure 3.1. Relationship between u^+ and y^+ in various sections of the boundary layer *(*SimScale*, 2024)*.

The law of the wall provides a universal description of the near-wall velocity profile in turbulent boundary layers, valid for a wide range of flow conditions and geometries. It serves as the basis for turbulence modeling approaches such as wall functions, which approximate the near-wall flow behavior using empirical correlations derived from the law of the wall.

There are several types of wall functions used in CFD simulations, including:

- *Standard Wall Functions:* These functions assume a logarithmic velocity profile near the wall and use empirical correlations to determine the velocity and temperature values at the first grid point away from the wall.
- *Enhanced Wall Functions*: Enhanced wall functions improve upon standard wall functions by incorporating corrections to account for effects such as adverse pressure gradients, flow separation, and non-equilibrium turbulence.

- *Non-Equilibrium Wall Functions:* These wall functions consider the non-equilibrium effects in the near-wall region, such as flow unsteadiness and intermittency, to improve accuracy in highly turbulent and transitional flows.

To apply wall functions in a CFD simulation, the user specifies appropriate boundary conditions at the solid walls, typically in the form of wall functions, near-wall grid resolution, and turbulence model settings. The CFD solver then calculates the flow field using these boundary conditions, with the wall functions providing accurate representations of the near-wall behavior. While wall functions offer significant computational savings, they also come with limitations and considerations. Wall functions are based on empirical correlations and assumptions about the near-wall flow behavior, which may not always hold true for complex flows or near rough or highly curved surfaces. Grid resolution near the wall affects the accuracy of wall functions. It is essential to ensure that the first grid point away from the wall is located within the logarithmic region of the boundary layer. Wall functions may not capture phenomena such as flow separation, pressure gradients, or thermal stratification accurately. In such cases, more advanced modeling techniques or resolved simulations may be necessary.

Wall functions utilized for the k-ε-τ turbulence model in wall-bounded flows are as follows:

- Turbulent kinetic energy (k): kqRWallFunction

In OpenFOAM, the `kqRWallFunction` boundary condition is typically used to model the turbulent kinetic energy (k) near wall regions in turbulent flow simulations. This boundary condition is based on the concept of the turbulent kinetic energy dissipation rate (ε) and is used in conjunction with the standard wall functions approach.

The `kqRWallFunction` boundary condition assumes a logarithmic velocity profile near the wall and employs the following equations:

Logarithmic Law:

$$u^+ = \frac{1}{\kappa}\ln(y^+) + B \tag{3.10}$$

where u^+ is the dimensionless velocity (normalized by the friction velocity, u_τ. y^+ is the dimensionless distance from the wall (normalized by the viscous length scale, ν/u_τ). κ is the von Kármán constant (approximately 0.41). B is a constant determined empirically.

Near-Wall Turbulent Kinetic Energy:

$$k = \frac{u_\tau^2}{C_\mu} f_\mu \tag{3.11}$$

where u_τ is the friction velocity. C_μ is the turbulence model constant. f_μ is a damping function that corrects the near-wall behavior of the turbulence model.

- Specific dissipation rate (ω): omegaWallFunction

The omega wall function integrates the viscous and logarithmic equations, as previously discussed in the theory. The omegaWallFunction in OpenFOAM is a specialized wall function that transitions between the viscous and logarithmic regions based on the y^+ position. The value at the junction of the viscous sublayer and the log-law region is determined by integrating the values from both the viscous and log-law sublayers.

The equations below indicate that omegavis and omegalog are computed at the cell's surface, thereafter blended to determine the value at the cell center.

In the viscous layer, it is defined by:

$$\omega_{vis} = \frac{6\nu}{\beta_1 y^2} \tag{3.12}$$

where β_1 is a constant and equals to 0.075.

In the log-law layer, the relation is expressed as follows:

$$\omega_{log} = \frac{\sqrt{k}}{\sqrt[4]{C_\mu}\kappa y} \tag{3.13}$$

where k represents the cell value. Thus, obtaining the integration of Equation (3.12) and Equation (3.13).

$$\omega = \sqrt{\omega_{vis}^2 + \omega_{log}^2} \tag{3.14}$$

- Turbulent dissipation rate (ε): epsilonWallFunction (modified)

Instead of using two different functions, a single equation is used in the model simulations for the three-equation model. The `epsilonWallFunction` boundary condition typically implements a power law profile for ε near the wall, expressed as follows:

$$\varepsilon = \frac{C_{\mu}^{0.75} k^{1.5}}{\kappa y} \tag{3.15}$$

where ε is the turbulent kinetic energy dissipation rate. k is the turbulent kinetic energy. y is the distance from the wall. C_{μ} is the turbulent kinetic energy dissipation rate model constant.

- Turbulent time scale (τ): tauWallFunction (implemented in this study)

Similar to epsilonWallFunction, tauWallFunction employs a single equation such as below:

$$\tau = \frac{z_1 \kappa y}{C_{\mu}^{0.75} k^{1.5}} \tag{3.16}$$

Here, z_1 denotes a constant which is equal to 0.505.

3.5.Optimization / Model Calibration Methodology

Bayesian model calibration is a systematic method that modifies the parameters of a model to align with observed data, while also measuring the uncertainty in both the model parameters and the predictions. This approach entails revising initial assumptions regarding the model parameters by incorporating observed data through the utilization of Bayes' Theorem. As a consequence, a posterior distribution is obtained, which accurately represents the updated beliefs concerning the parameters. Below, you will find a detailed description of how Bayesian analysis operates within the framework of model calibration.

- Defining the model and its parameters:

The initial stage of Bayesian calibration involves establishing the model, identifying the parameters to be calibrated, and selecting the data to be used for calibration. The model can be formulated as:

$$y = f(x, \theta) + \epsilon \tag{3.17}$$

where, *y* is the observed data, $f(x, \theta)$ is the model output, where *x* represents the inputs and θ denotes the parameters to be calibrated. ϵ denotes the measurement or model error, typically believed to follow a normal distribution with a mean of zero and a variance σ^2.

The goal is to find the posterior distribution of the parameters θ given the observed data *y*.

- Specifying the prior distribution:

The prior distribution $P(\theta)$ reflects the initial beliefs about the parameters before observing the data. Priors can be informative, based on previous studies or expert knowledge, or non-informative if no prior information is available.

For example, if you have a parameter θ, you might specify a normal prior:

$$\theta \sim \mathcal{N}(\mu_0, \sigma_0^2) \tag{3.18}$$

where μ_0 is the mean of the prior distribution, σ_0^2 is the variance of the prior distribution.

- Defining the Likelihood Function:

The probability function $P(\boldsymbol{y}|\boldsymbol{\theta})$ quantifies the degree to which the model, characterized by the parameter set $\boldsymbol{\theta}$, provides an accurate explanation for the observed data y. The phrase "It captures the probability of observing the data given the model parameters" refers to the measure of the likelihood of the data being observed based on the specific values of the model parameters. If the mistakes follow a normal distribution, the likelihood can be represented as:

$$P(y|\theta) = \prod_{i=1}^{n} \frac{1}{\sqrt{2\pi\sigma^2}} \exp\left(-\frac{\left(y_i - f(x_i, \theta)\right)^2}{2\sigma^2}\right) \tag{3.19}$$

where *n* is the number of observations, y_i represents the observed data point. $f(x_i, \boldsymbol{\theta})$ denotes the model output for the input x_i.

- Calculating the Posterior Distribution:

The posterior distribution $P(\boldsymbol{\theta}|\mathbf{y})$ is derived by applying Bayes' Theorem, which incorporates the observed data to update the prior beliefs.

$$P(\theta|y) = \frac{P(y|\theta) \times P(\theta)}{P(y)} \quad (3.20)$$

where $P(\boldsymbol{\theta}|\boldsymbol{y})$ is the posterior probability of the parameters given the observed data, $P(\boldsymbol{y}|\boldsymbol{\theta})$ denotes the likelihood of the data given the parameters, $P(\boldsymbol{\theta})$ represents the prior probability of the parameters. $P(\boldsymbol{y})$ is the evidence or marginal likelihood, calculated as:

$$P(y) = \int P(y|\theta)P(\theta)d\theta \quad (3.21)$$

The evidence serves as a normalizing constant, guaranteeing that the posterior is a legitimate probability distribution.

- Performing Posterior Inference:

Computing the posterior distribution directly can be impractical because of the intricacy of the integrals required. Hence, computational techniques like Markov Chain Monte Carlo (MCMC) are employed to extract samples from the posterior distribution.

  - MCMC Algorithms:
    I. Metropolis-Hastings: Suggests alternative parameter values and approves them based on their likelihood ratio in comparison to the present values.
    II. Gibbs Sampling: Sequentially samples each parameter from its conditional distribution, taking into account the current values of the other parameters.
    III. Hamiltonian Monte Carlo (HMC): Utilizes the gradient information from the likelihood function to generate new samples, resulting in improved efficiency for situations with a high number of dimensions.

These techniques produce samples from the posterior distribution, which can be utilized to estimate summary statistics such as the mean and variance, or to determine credible ranges for the parameters.

- <u>Model Calibration and Uncertainty Quantification:</u>

By utilizing the samples derived from the posterior distribution, it is possible to:

- Calibrate the Model: Calibrate the model parameters by setting their values to the posterior mean or mode, in order to align them with the observed data.
- Quantify Uncertainty: The posterior distribution quantifies the level of uncertainty associated with the calibrated values. Credible intervals are formed to indicate the range in which the true values of the parameters are likely to be found, with a specified probability (e.g., 95%).

- Validation and Model Checking:

Following the calibration process, it is essential to validate the model to confirm its accurate representation of the data. This can be accomplished by:

- Posterior Predictive Checks: Generate data from the posterior predictive distribution:

$$\tilde{y} \sim P(y|\theta), \quad \theta \sim P(\theta|y) \tag{3.22}$$

Comparing the simulated data $\tilde{y}$ with the observed data $\boldsymbol{y}$ helps assess model fit.

- Goodness-of-Fit Statistics: Employ statistical techniques such as the posterior predictive p-value or residual analysis to assess the adequacy of the fit.
- Sensitivity Analysis: Analyze the extent to which the posterior is affected by the selection of priors and evaluate the robustness of the calibration outcomes.

Bayesian calibration offers a thorough framework for estimating parameters, taking into account uncertainties and prior knowledge. This makes it particularly effective in sectors where precise and dependable model predictions are essential.

4. TURBULENCE MODEL DEVELOPMENT AND VALIDATION

The development of turbulence models involves a combination of theoretical analysis, empirical observations, and numerical simulations. Theoretical frameworks, such as RANS equations or LES techniques, provide the foundation for turbulence modelling. Empirical correlations and experimental data play a crucial role in guiding model development and validating its predictions against real-world observations.

The validation process of turbulence models is essential for assessing their accuracy and reliability across a range of flow conditions. Validation typically involves comparing model predictions with experimental data obtained from laboratory experiments, field measurements, or high-fidelity numerical simulations. Metrics such as mean velocity profiles, turbulence intensity, and Reynolds stresses are commonly used to evaluate the performance of turbulence models. Additionally, model validation may involve benchmarking against analytical solutions for simplified flow configurations or well-documented test cases.

The validation process is not limited to qualitative agreement between model predictions and experimental data but also includes quantitative assessments of model performance. Statistical measures such as RMSE, correlation coefficients, and spatial correlation functions are used to quantify the level of agreement between model predictions and experimental observations. Sensitivity analyses are also conducted to identify model parameters that significantly impact the predictions and to assess the robustness of the turbulence model.

In recent years, advancements in computational capabilities have facilitated the development of more sophisticated turbulence models, such as hybrid RANS-LES approaches and data-driven machine learning techniques. These models offer improved accuracy and applicability for a wide range of turbulent flows, from boundary layer flows to complex turbulent flows encountered in engineering and environmental systems.

The motivation behind the WFC three equation turbulence model is to decouple the dissipation and the time and length scales and introduce a minimum of additional complexity. Towards this end, Wu, Ferziger and Chapman (Wu et al., 1985) introduced

a model equation for a turbulence time scale τ to be solved together with the k and ε equations.

For homogeneous isotropic decay flow, the exact equation of the TKE reduces to:

$$\frac{dk}{dt} = -\varepsilon \tag{4.1}$$

The model equation for dissipation rate is modified to include the new turbulence time scale:

$$\frac{d\varepsilon}{dt} = -\frac{\varepsilon}{\tau} \tag{4.2}$$

This equation can also be seen as the definition of the new time-scale τ. In isotropic turbulence decay behind a grid, TKE, k decays according to power law ($k = t^{-n}$). The turbulence kinetic-energy Equation (4.1). then yields $\varepsilon = nt^{-n-1}$. These can be used together with the Equation (4.2) in order to close the set of model equations to yield $\frac{d\tau}{dt} = \frac{1}{n+1}$ in differential form which suggests a constant term associated with the τ equation.

When strain is applied to the flow, all turbulence quantities are modified. In particular, the turbulence time scale τ is pushed away from equilibrium. After the strain is removed, the turbulence tends to return to an equilibrium state. The modifications adopted by Wu et al. (Wu et al., 1985) to accomplish this is:

$$\frac{d\tau}{dt} = \frac{1}{n+1} + C_5(z - z_0) \tag{4.3}$$

where $z = \frac{\varepsilon\tau}{k}$ and z_0 is the value of z in isotropic decay flow (i.e., since the energy spectrum shape is preserved during decay $z_0 = \left(\frac{\varepsilon\tau}{k}\right)_0$ is a constant which gives $\tau = \frac{z_0 t}{n}$). By using the ε – transport equation, $z_0 = \frac{n}{n+1}$ can be deduced which shows that z_0 is the reciprocal of $C_{\varepsilon 2}$ in the $k - \varepsilon$ model. Wu et al. (Wu et al., 1985) chose z_0 to be 0.54.

By manipulating Equations (4.1-4.3), the following expression for z can be obtained:

$$\frac{dz}{dt} = \frac{\varepsilon}{k(1 + C_5)(z - z_0)} \tag{4.4}$$

In the (*z, dz/dt*) phase plane $(z_{0,0})$ is an equilibrium point. For this to be a stable point, in other words, to assure return to equilibrium, $1 + C_5$ must be negative or $C_5 < -1$.
Final form of the model equations of the WFC model for homogeneous incompressible axisymmetric expansion flow was then given as*:

$$\frac{dk}{dt} = P_k - \varepsilon \tag{4.5}$$

$$\frac{d\varepsilon}{dt} = -\frac{\varepsilon}{\tau} + C_1 \frac{P_k \varepsilon}{k} \tag{4.6}$$

$$\frac{d\tau}{dt} = \frac{1}{n+1} + C_5(z - z_0) + C_6 S\tau \tag{4.7}$$

where P_k is the production of TKE and *S* is the mean strain rate. On the basis that "production of dissipation" estimated by the *k*-*ε* model is too weak (i.e., ε is under-predicted in high strain rate flows), Wu et al. (Wu et al., 1985) had tended to increase C_1 and tuned the coefficients at $C_1 = 2$ and $C_6 = -2$. However, the choice of $C_1 = 2$ does not satisfy spreading rate predictions for shear flows, as this coefficient tuned here for a plane jet is found to be $C_1 = 1.44$.

4.1.Turbulence Model Development Procedure

The current methodology expands upon the existing model to incorporate shear flows, subsequently employing the modified model to analyze the plane far wake, axisymmetric and planar jet. In this section we will show that we can look at the WFC-model from a slightly different viewpoint and derive the relations among the model constants for the modified k-ε-τ turbulence model.

For homogeneous shear flow the model equations with the proposed modifications are as follows:

$$\frac{dk}{dt} = P_k - \varepsilon \tag{4.8}$$

$$\frac{d\varepsilon}{dt} = C_{\varepsilon 1} \frac{P_k}{\tau} - C_{\varepsilon 2} \frac{\varepsilon}{\tau} \tag{4.9}$$

* Here the WFC-model is expressed in a form more suitable for the context.

$$\frac{d\tau}{dt} = C_{\tau 0} - C_{\tau 1} z - C_{\tau 2} \frac{P_k}{\varepsilon} z \tag{4.10}$$

Modification to the WFC model stem from the fact that:

- First item; Production and destruction terms of ε in the Equation (4.6) cannot balance each other properly with two different time scales in each (i.e., $\frac{k}{\varepsilon}$ in the production term of ε and τ in the other), and this imbalance causes the model to give instability and overshoot of the turbulence viscosity in shear flows particularly in plane and round jets. This, therefore, necessitated the use of the same time scale in both terms in the ε - equation for shear flows;
- τ – equation in Equation (4.7), as it is, cannot account for shear flows as also warned by Wu et al. (Wu et al., 1985). Hence a production related term associated with the $C_{\tau 2}$ constant has been added to the τ - equation, and its coefficient has been tuned to give the best result for free shear flows provided that coefficients satisfy the relations derived below.

4.1.1. Grid Turbulence Decay

In the above equations, the τ – equation (Equation (4.10)) gives a relation between $C_{\tau 0}$ and $C_{\tau 1}$ in isotropic turbulence decay behind a grid.

$$\frac{d\tau}{dt} = C_{\tau 0} - C_{\tau 1} z_0 = \frac{z_0}{n} \tag{4.11}$$

By rearranging we get $C_{\tau 0} = 1 - z_0(1 - C_{\tau 1})$.

4.1.2. Return to Equilibrium

Differentiation of $z = \frac{\varepsilon \tau}{k}$ yields:

$$\frac{dz}{dt} = \frac{\varepsilon}{k}\frac{d\tau}{dt} + \frac{\tau}{k}\frac{d\varepsilon}{dt} - \frac{\varepsilon\tau}{k^2}\frac{dk}{dt} \tag{4.12}$$

Then inserting *k, ε* and *τ* transport equations we can get a transport equation for *z*. In the absence of TKE production, the transport equation for *z*, in grid decay, reduces to:

$$\frac{dz}{dt} = \frac{\varepsilon}{k}[z(1 - C_{\tau 1}) + (C_{\tau 0} - 1)] \tag{4.13}$$

When turbulence is in equilibrium state (i.e., $z=z_0$) RHS of this equation (what we call H) must be zero. Thus,

$$H = \frac{\varepsilon}{k(z - z_0)(1 - C_{\tau 1})} \tag{4.14}$$

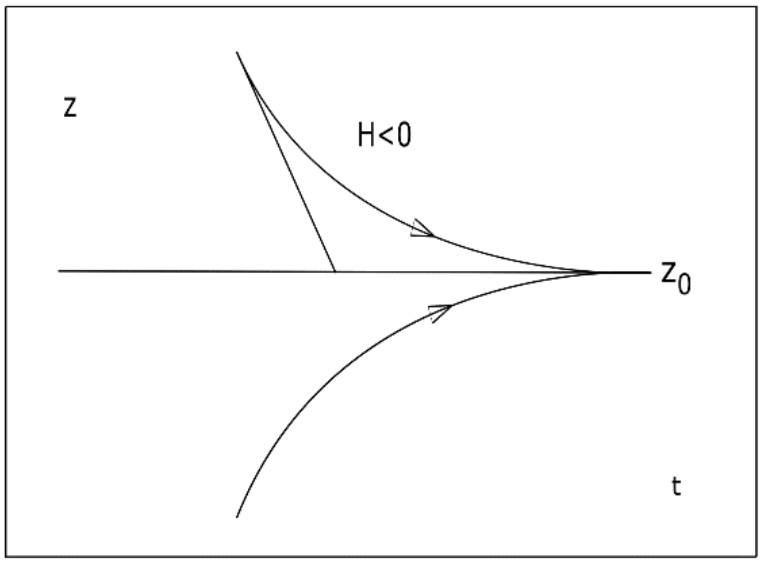

Figure 4.1. Return to equilibrium of z (M. Z. Gul et al., 2024)

If z is perturbed from its equilibrium point in the direction of larger z, ($z>z_0$), after removing strain, as can be seen qualitatively from **Figure *4.1***, z tends to return to z_0 in such a way that we require $H \leq 0$. For the displacement of z in the opposite direction, z will again return to $z=z_0$, after removing strain. In this case we require $H>0$, therefore $C_{\tau 1} > 1$.

4.1.3. Constraint for the Coefficient of Mean Strain Term

In the presence of mean strain, our basic assumption is that, if, in a homogeneous flow, the ratio $\frac{P_k}{\varepsilon}$ is held at a fixed value, the turbulence spectrum will evolve to an equilibrium form i.e., z approaches a fixed value. The general transport equation for z is:

$$dz/dt = \varepsilon/k\ [(z - z_0)(1 - C_{\tau 1}) + \frac{P_k}{k(C_{\varepsilon 1} - z(1 + C_{\tau 2})]}] \tag{4.15}$$

For any given $\frac{P_k}{\varepsilon}$, z will always approach its equilibrium value z_e which is presumably a function of $\left(\frac{P_k}{\varepsilon}\right)$. If $z=z_e$ in its equilibrium then $\frac{Dz}{Dt} \equiv 0$.

Therefore,

$$(z_e - z_0)(1 - C_{\tau 1}) = -\frac{P_k}{\varepsilon\left(C_{\varepsilon 1} - z_e(1 + C_{\tau 2})\right)} \tag{4.16}$$

or,

$$\frac{z_0}{z_e} = 1 + \frac{P_k}{\varepsilon}\frac{C_{\varepsilon 1} - z_e(1 + C_{\tau 2})}{(1 - C_{\tau 1})z_e} \tag{4.17}$$

Since $1 - C_{\tau 1} < 0$ we must require $C_{\varepsilon 1} - z_e(1 + C_{\tau 2}) \leq 0$ to avoid the risk of z becoming negative. In other words, $C_{\tau 2} \geq \frac{C_{\varepsilon 1}}{z_\varepsilon} - 1$. In the event of z_e=z_0 for all $\frac{P_k}{\varepsilon}$ we get:

$$C_{\tau 2} \geq \frac{C_{\varepsilon 1}}{z_0} - 1 \tag{4.18}$$

4.1.4. Local Equilibrium

In the case of local equilibrium where $P_k \equiv \varepsilon$, the z transport equation becomes with $z_1 = \left(\frac{\varepsilon\tau}{k}\right)_1$:

$$\left(\frac{dz}{dt}\right)_1 = \frac{\tau}{k}\frac{d\varepsilon}{dt} + \frac{\varepsilon}{k}\frac{d\tau}{dt} = 0 \tag{4.19}$$

Together with the ε and τ-transport equations:

$$\frac{d\varepsilon}{dt} = (C_{\varepsilon 1} - 1)\frac{P_k}{\tau} \tag{4.20}$$

$$\frac{d\tau}{dt} = C_{\tau 0} - C_{\tau 1}z_1 - C_{\tau 2}z_1 \tag{4.21}$$

we get another relation between the coefficients. (Note that RHS of τ – equation is constant.)

$$1 - C_{\varepsilon 1} = C_{\tau 0} - z_1(C_{\tau 1} + C_{\tau 2}) \tag{4.22}$$

Here one must note that we have a freedom of choosing z_0, provided that we initially adjust the coefficients in the ε-equation accordingly. Comparison of ε-equations for *k*-ε and *k*-ε-τ models yields that for z_0=6/11, $C_{\varepsilon 1}$becomes $C_{\varepsilon 1} \cong 0.75$ which is a good choice. This also implies that $C_{\varepsilon 2}$ taken as $C_{\varepsilon 2} = 1.0$. $C_{\tau 0} = 1.054$ and $C_{\tau 1} = 1.1$ are taken in parallel with WFC model, and $C_{\tau 2}$establishes quite well at $C_{\tau 2} = 0.59$ for jet flow computations presented in the next section. This is also in agreement with the previous

constraint (Equation (4.18)) on $C_{\tau 2}$ which suggested that $C_{\tau 2} > 0.375$. A rough estimation of z_1 from Equation (4.22) yields that it is in the range of $0.47<z_1<0.54$ for $\frac{P_k}{\varepsilon} < 1.3$. Equation (4.16) can be re-organized to yield:

$$z_e = \frac{z_0 + \frac{C_{z1} P_k}{\varepsilon}}{1 + \frac{C_{z2} P_k}{\varepsilon}} \tag{4.23}$$

where $C_{z1} = \frac{C_{\varepsilon 1}}{C_{\tau 1} - 1}$ and $C_{z2} = \frac{C_{\tau 2} + 1}{C_{\tau 1} - 1}$. The Equation (4.23) has an asymptotic value of 0.472 for z_e vs $\frac{P_k}{\varepsilon}$ with the values of coefficients given at Table 1, which indicates that assumption of $z_e \cong z_0 = 0.54$ is well within the 13% error range.

The near-wall equilibrium layer can help in providing a relation for σ_ε as in the $k - \varepsilon$ turbulence model. The ε -equation can be expressed as follows by neglecting convection, diffusion of energy, and convective transport of ε:

$$0 = \frac{\partial}{\partial y}\left(\frac{\mu_T}{\sigma_\varepsilon}\frac{\partial \varepsilon}{\partial y}\right) + C_{\varepsilon 1}\rho\frac{P_k}{\tau} - C_{\varepsilon 2}\rho\frac{\varepsilon}{\tau} \tag{4.24}$$

With the assumption of constant wall shear stress and logarithmic law of the wall theory, Equation (4.24) can be cast into*:

$$\sigma_e = \frac{z_1 \kappa^2}{C_\mu^{\frac{1}{2}}(C_{\varepsilon 2} - C_{\varepsilon 1})} \tag{4.25}$$

σ_e and σ_τ together with other coefficients are then optimized by numerical experiments to give the best results in simple shear flows.

4.2.k-ε-τ Turbulence Model

Starting point of this study was the three-equation turbulence model of Gul (Z. Gul, 1994). In his model, Gul suggested the possibility of using a two-time scale model for better prediction of flow in both larger scales and smaller scales. In that context, he formed

* Here $\tau = z_1\, \kappa y / C_\mu^{1/2} U_\tau$ was also employed since $\tau = z_1 k/\varepsilon$ in local equilibrium.

another transport equation for the larger eddies time-scale, τ, in addition to the equations of turbulent kinetic energy, k, and turbulent dissipation rate, ε.

Preliminary results are the outcomes of Gul's model with a minor modification in coefficients chosen based on many trials on the coefficients. This fix may be attributed to the variances in results between parabolic and elliptic codes. Since throughout this study, OpenFOAM is used as a sole CFD package for all the simulations. Gul's model can be found below in general form which is implemented exactly as in OpenFOAM with the mentioned modification above.

$$\frac{\partial(\rho k)}{\partial t} + \frac{\partial(\rho U_j k)}{\partial x_j} = \frac{\partial}{\partial x_j}\left(\frac{\mu_t}{\sigma_k}\frac{\partial k}{\partial x_j}\right) + P_k - \rho\varepsilon \tag{4.26}$$

$$\frac{\partial(\rho\varepsilon)}{\partial t} + \frac{\partial(\rho U_j \varepsilon)}{\partial x_j} = \frac{\partial}{\partial x_j}\left(\frac{\mu_t}{\sigma_\varepsilon}\frac{\partial \varepsilon}{\partial x_j}\right) + C_{\varepsilon 1}\frac{P_k}{\tau} - C_{\varepsilon 2}\rho\frac{\varepsilon}{\tau} - C_{\varepsilon 3}\rho\varepsilon S \tag{4.27}$$

$$\frac{\partial(\rho\tau)}{\partial t} + \frac{\partial(\rho U_j \tau)}{\partial x_j} = \frac{\partial}{\partial x_j}\left(\frac{\mu_t}{\sigma_\tau}\frac{\partial \tau}{\partial x_j}\right) + C_{\tau 0}\rho - C_{\tau 1}\frac{\varepsilon\tau}{k} - C_{\tau 2}\frac{P_k}{\varepsilon}\frac{\varepsilon\tau}{k} - C_{\tau 3}\rho\tau S \tag{4.28}$$

Model constants can be found in the table below (**Table 4.1**):

Table 4.1. k-ε-τ Turbulence model constants

$C_{\varepsilon 1}$	$C_{\varepsilon 2}$	$C_{\varepsilon 3}$	$C_{\tau 0}$	$C_{\tau 1}$	$C_{\tau 2}$	$C_{\tau 3}$	σ_k	σ_ε	σ_τ
0.75	1.05	0.67	1.054	1.1	0.59	0.83	1.0	1.2	1.1

4.3.k-ω-τ Turbulence Model

Considering the ability to capture the flow field better (as in SST-k- ω), especially in wall-bounded low scenarios, it has been assumed that integrating ω instead of ε in three-equation, two-time-scale turbulence model could provide better outcomes. In fact, it has been proven that with the help of optimization techniques, the results of two of the cases appear to be better than the rest of the turbulence models used in the current study.

However, integration of ω-equation with turbulent time-scale equation coupled with turbulent kinetic energy equation was not straightforward. Four different versions of ω-equation have been tested and version-3 was selected as the final version according to the

results achieved by both CFD simulations and model calibration outcomes. All four versions of ω-equation can be found in the following paragraphs.

Starting from the general form of the equations that can be found below (version-0 (v0)):

$$\frac{\partial(\rho k)}{\partial t} + \frac{\partial(\rho u_j k)}{\partial x_j} = \frac{\partial}{\partial x_j}\left[\left(\mu + \alpha_k \frac{\rho k}{\omega}\right)\frac{\partial k}{\partial x_j}\right] + P - \beta^* \rho \omega k \tag{4.29}$$

$$\frac{\partial(\rho \omega)}{\partial t} + \frac{\partial(\rho u_j \omega)}{\partial x_j} = \frac{\partial}{\partial x_j}\left[\left(\mu + \alpha_\omega \frac{\rho k}{\omega}\right)\frac{\partial \omega}{\partial x_j}\right] + \rho \frac{\gamma}{\beta^* k \tau} P - \beta \rho \frac{\omega}{\beta^* \tau} + \frac{\rho \sigma_d}{\omega}\frac{\partial k}{\partial x_j}\frac{\partial \omega}{\partial x_j} \tag{4.30}$$

$$\frac{\partial(\rho \tau)}{\partial t} + \frac{\partial(\rho u_j \tau)}{\partial x_j} = \frac{\partial}{\partial x_j}\left[\left(\mu + \frac{\rho k}{\sigma_\tau \omega}\right)\frac{\partial \tau}{\partial x_j}\right] + C_{\tau 0}\rho - C_{\tau 1}\rho \beta^* \omega \tau - C_{\tau 2} P \frac{\tau}{k} \tag{4.31}$$

where,

$$P = \tau_{ij}\frac{\partial u_i}{\partial x_j} \tag{4.32}$$

$$\tau_{ij} = \mu_t\left(2S_{ij} - \frac{2}{3}\frac{\partial u_k}{\partial x_k}\delta_{ij}\right) - \frac{2}{3}\rho k \delta_{ij} \tag{4.33}$$

$$S_{ij} = \frac{1}{2}\left(\frac{\partial u_i}{\partial x_j} + \frac{\partial u_j}{\partial x_i}\right) \tag{4.34}$$

and turbulent kinetic energy is computed from,

$$\mu_t = \rho \frac{k}{\widehat{\omega}} \tag{4.35}$$

where,

$$\widehat{\omega} = \max\left(\omega,\ C_{\lim}\sqrt{\frac{2\overline{S_{ij}}\,\overline{S_{ij}}}{\beta^*}}\right) \tag{4.36}$$

$$\overline{S_{ij}} = S_{ij} - \frac{1}{3}\frac{\partial u_k}{\partial x_k}\delta_{ij} \tag{4.37}$$

Constants and auxiliary functions are,

$$\sigma_k = 0.6,\ \sigma_\omega = 0.5, \sigma_\tau = 1.1,\ \beta^* = 0.09,\ \gamma = 0.52,\ C_{lim} = 0.875,\ \beta = \beta_o f_\beta,\ \beta_o = 0.0708 \tag{4.38}$$

$$f_\beta = \frac{1+85\chi_\omega}{1+100\chi_\omega}, \chi_\omega = \left|\frac{\Omega_{ij}\Omega_{jk}\hat{s}_{ki}}{(\beta\omega)^3}\right|, \hat{s}_{ki} = S_{ki} - \frac{1}{2}\frac{\partial u_m}{\partial x_m}\delta_{ki}, \Omega_{ij} = \frac{1}{2}\left(\frac{\partial u_i}{\partial x_j} - \frac{\partial u_j}{\partial x_i}\right) \quad (4.39)$$

$$\sigma_d = \begin{cases} 0, & \frac{\partial k}{\partial x_j}\frac{\partial \omega}{\partial x_j} \leq 0 \\ 0.125, & \frac{\partial k}{\partial x_j}\frac{\partial \omega}{\partial x_j} > 0 \end{cases} \quad (4.40)$$

While the other transport equations keep the same form, the other versions of ω-equation considered in the current study are given below:

$$v1: \frac{\partial(\rho\omega)}{\partial t} + \frac{\partial(\rho u_j \omega)}{\partial x_j} = \frac{\partial}{\partial x_j}\left[\left(\mu + \alpha_\omega \frac{\rho k}{\omega}\right)\frac{\partial \omega}{\partial x_j}\right] + \rho\frac{\gamma\omega}{k}P - \beta\rho\frac{\omega}{\beta^*\tau} + \frac{\rho\sigma_d}{\omega}\frac{\partial k}{\partial x_j}\frac{\partial \omega}{\partial x_j} \quad (4.41)$$

$$v2: \frac{\partial(\rho\omega)}{\partial t} + \frac{\partial(\rho u_j \omega)}{\partial x_j} = \frac{\partial}{\partial x_j}\left[\left(\mu + \alpha_\omega \frac{\rho k}{\omega}\right)\frac{\partial \omega}{\partial x_j}\right] + \rho\frac{\gamma}{\beta^* k\tau}P - \beta\rho\omega^2 + \frac{\rho\sigma_d}{\omega}\frac{\partial k}{\partial x_j}\frac{\partial \omega}{\partial x_j} \quad (4.42)$$

$$v3: \frac{\partial(\rho\omega)}{\partial t} + \frac{\partial(\rho u_j \omega)}{\partial x_j} = \frac{\partial}{\partial x_j}\left[\left(\mu + \alpha_\omega \frac{\rho k}{\omega}\right)\frac{\partial \omega}{\partial x_j}\right] + \rho\frac{\gamma\omega}{k}P - \beta\rho\omega^2 + \frac{\rho\sigma_d}{\omega}\frac{\partial k}{\partial x_j}\frac{\partial \omega}{\partial x_j} \quad (4.43)$$

The rationale behind the selection was of course, directly depending on the results of simulations and optimization study. In the meantime, integration of the τ into production term rather than the sink term is assumed to be the most effective and meaningful, since τ is designed to be the larger eddies' time scale.

4.3.1. Optimization & Model Calibration Process

The model calibration process was carried out using BA, considering the studies investigated in Literature Review section. Those studies involved optimization techniques, machine learning algorithms and artificial intelligence methods and various regression methodologies. Specifically, various ML techniques applied on RANS including modifying model parameters with Bayesian methods, introducing a correction factor for the turbulence production term using NNS and adding a spatially distributed correction field via field inversion and Gaussian process. However, some of them seem to be not physically interpretable.

As it was stated above, following the optimization methodology explained in previous chapter, BA applied using below parameters and feeding the model with fast CFD simulations of channel flow and plane far wake data. Since, these two cases converge in matter of minutes, carrying out a grid study wouldn't have been a big problem which is already mentioned by several researchers (Zhang et al., 2023). For k-ω-τ model, three of the coefficients of τ-equation, namely $\boldsymbol{C_{\tau 0}}$, $\boldsymbol{C_{\tau 1}}$, $\boldsymbol{C_{\tau 2}}$, and one coefficient of ω-equation that is found be the most effective parameter according to preliminary studies, γ have been selected for the calibration work.

To simplify the process, the output parameter is selected by a summation of RMSE data collected from four entities, each multiplied by a factor considering its importance. These entities are also plotted as graphs. They are basically comprised of normalized velocity profiles, wall-normalized velocity, wall-normalized turbulent kinetic energy, and wall-normalized shear stress. The selected weighting factors are as follows: 0.4 for normalized velocity, 0.25 for wall-normalized velocity, 0.1 for wall-normalized turbulent kinetic energy, 0.25 for wall-normalized shear stress. These weighting factors also have been tested using different values. The best set has been chosen for the optimization and following simulations.

For the optimization of coefficients, python programming language has been used as the Bayesian optimization (BO) procedure. Following libraries have been used extensively: Pandas for data manipulation and reading from excel files, NumPy for numerical operations, Sklearn for data scaling, splitting, and model evaluation, TensorFlow and Keras for building and training the neural network model and finally Scikit-Optimize for performing BO.

After selecting the coefficients to be optimized, the process of optimization begins by importing libraries, followed by loading the data from an excel file containing design points with parameters P1, P2, P3, P4, and a target output parameter to prepare the dataset. Then, the code carries out normalization which scales the features to have zero mean and unit variance. This is crucial for effective neural network training. After that, defining the neural network section begins. In the current study, the following parameters and options were selected: A sequential model with two hidden layers, each with 128 neurons and ReLU activation. The output layer has one neuron (since it's a regression problem). The

model uses the Adam optimizer and mean squared error loss function. Mean squared error is tracked as a performance metric. Parameter space has been defined for the bounds for each parameter that will be optimized. Here, each parameter ranges from 0.01 to 10. The objective function is defined for BO followed by data preparation that creates a feature matrix using the current values of parameters being optimized. Here, the data is split into two sets 80% for training, and 20% for validation. The model is fitted on the training set. Then, the model is evaluated by predicting on the validation set and calculates the mean squared error.

$$MSE = \frac{1}{N}\sum_{i=1}^{n}(y_i - \hat{y}_i) \tag{4.44}$$

Here, y_i represent the true values, and $\hat{y}_i$ are the predicted values.

Finally, BO uses Gaussian process-based optimization to minimize the objective function over 100 calls and extracts the best parameters that resulted in the lowest MSE. Also, a so-called final model training is applied to retrain the model on the entire dataset using the best-found parameters. Lastly, the trained model is saved for future use.

This approach leverages Bayesian optimization to systematically and efficiently search through a multi-dimensional space to find the parameter combination that minimizes prediction error, offering a powerful alternative to manual or grid-based hyperparameter tuning.

Figure *4.2* shows normalized velocity profile, u^+ and y^+ graph, wall turbulent kinetic energy, and wall shear stress against normalized wall distance for channel flow case. As it can be seen from the graphs, there are many models including the *k*-ω-τ models with various coefficient combinations.

Some of the simulation results from the grid study of v0 of *k*-ω-τ model on plane far wake test case can be found below:

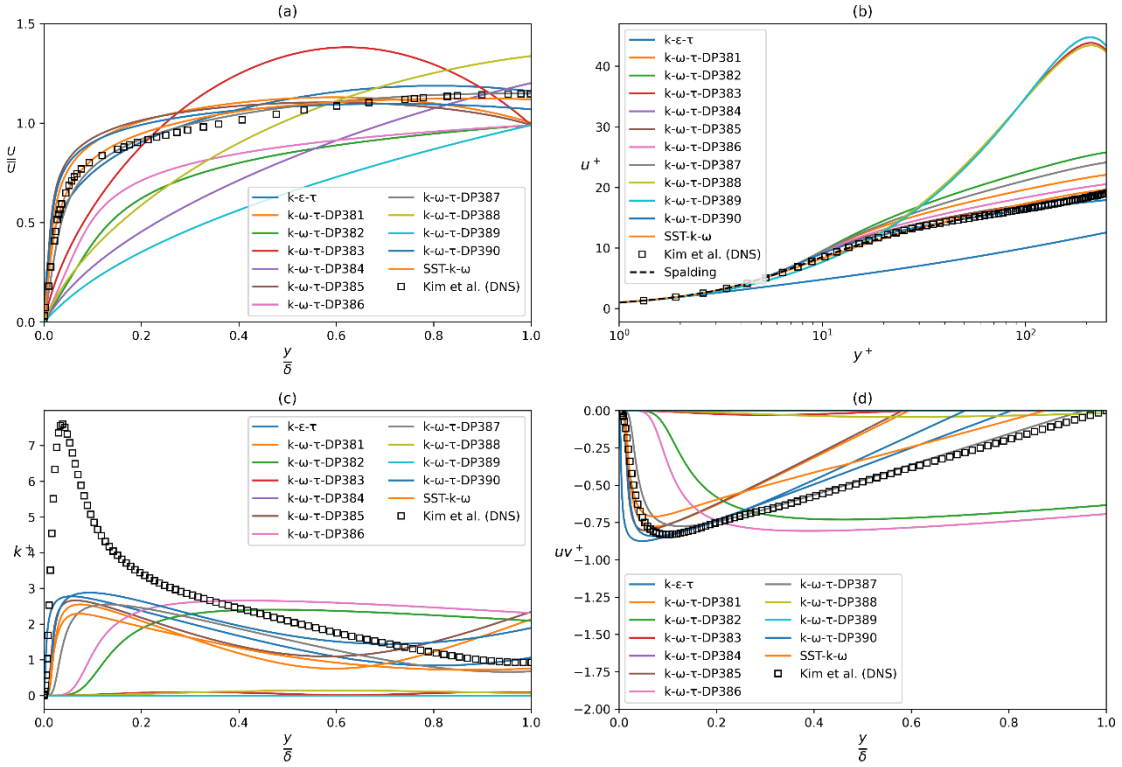

Figure 4.2. (a) Normalized velocity vs normalized wall distance, (b) Comparison of the dimensionless variables u^+ and y^+, (c) Wall turbulent kinetic energy vs normalized wall distance, (d) Wall shear stress vs normalized wall distance for channel flow case

Model calibration results showed that v3 of the ω-equation with the below coefficients (**Table 4.2**) were found to be the best for channel flow. And it also produces fairly acceptable results for plane far wake case.

Table 4.2. Values of the optimized coefficients of *k*-*ω*-*τ* turbulence model constants

$C_{\tau 0}$	$C_{\tau 1}$	$C_{\tau 2}$	γ
1.286	0.592	0.625	0.55

The model's best output parameter estimate is about 0.14.

4.4.R-ε-τ Reynolds Stress Model

The Reynolds stress model entails the computation of the individual Reynolds stresses, $\rho\overline{u_i'u_j'}$, through the utilization of differential transport equations. The various Reynolds stresses are subsequently employed to achieve closure of the Reynolds-averaged momentum equation.

The precise transport equations governing the transport of the Reynolds stresses, denoted as $\overline{u_i' u_j'}$, can be expressed as:

$$\begin{aligned}\frac{\partial}{\partial t}\left(\rho\overline{u_i' u_j'}\right) + \frac{\partial}{\partial x_k}\left(\rho u_k \overline{u_i' u_j'}\right) \\ = -\frac{\partial}{\partial x_k}\left[\rho\overline{u_i' u_j' u_k'} + \overline{p'\left(\delta_{kj}u_i' + \delta_{ik}u_j'\right)}\right] \\ + \frac{\partial}{\partial x_k}\left[\mu\frac{\partial}{\partial x_k}\left(\overline{u_i' u_j'}\right)\right] - \rho\left(\overline{u_i' u_j'}\frac{\partial u_j}{\partial x_k} + \overline{u_j' u_k'}\frac{\partial u_i}{\partial x_k}\right) \\ + \overline{p'\left(\frac{\partial u_i'}{\partial x_j} + \frac{\partial u_j'}{\partial x_i}\right)} - 2\mu\overline{\frac{\partial u_i'}{\partial x_k}\frac{\partial u_j'}{\partial x_k}} \\ - 2\rho\Omega_k\left(\overline{u_j' u_m'}\epsilon_{ikm} + \overline{u_i' u_m'}\epsilon_{jkm}\right)\end{aligned} \tag{4.45}$$

Above equation can be written in symbolic form:

$$Local\ Time\ Derivative + C_{ij} = D_{T,ij} + D_{L,ij} + P_{ij} + \varphi_{ij} - \epsilon_{ij} + F_{ij} \tag{4.46}$$

where, C_{ij} represents convective term, $D_{T,ij}$ denotes turbulent diffusion, $D_{L,ij}$ is the molecular diffusion, P_{ij} stands for the production of stress, φ_{ij} symbolizes pressure strain, ϵ_{ij} is the dissipation term, and F_{ij} the generation by the rotation of the system.

Among these only three of them have to modeled: $D_{T,ij}$, φ_{ij}, and ϵ_{ij}.

Adopting Rotta's approach, φ_{ij} can be modeled as (Rotta, 1951b):

$$\varphi_{ij} = -1.8\frac{\varepsilon}{k}\left(\overline{u_i u_j} - \frac{2}{3}\delta_{ij}k\right) \tag{4.47}$$

The diffusion terms can be approximated using Daly and Harlow's method as:

$$\varphi_{ij} = \frac{\partial}{\partial x_k}\left(0.22\frac{k}{\varepsilon}\overline{u_k u_m}\frac{\partial\overline{u_i u_j}}{\partial x_m}\right) \tag{4.48}$$

Here, ε-equation and τ-equation are coupled in the framework of RSM, using the same equations as they are given below:

$$\frac{\partial\varepsilon}{\partial t} + U_k\frac{\partial\varepsilon}{\partial x_k} = C_{\varepsilon 1}\frac{P_k}{\tau} + 0.18\frac{\partial}{\partial x_j}\left(\overline{u_j u_k}\frac{k}{\varepsilon}\frac{\partial\varepsilon}{\partial x_k}\right) - C_{\epsilon 2}\frac{\varepsilon}{\tau} \tag{4.49}$$

$$\frac{\partial \tau}{\partial t} + U_k \frac{\partial \tau}{\partial x_k} = C_{\tau 0} + 0.18 \frac{\partial}{\partial x_j}\left(\overline{u_j u_k} \frac{k}{\varepsilon} \frac{\partial \tau}{\partial x_k}\right) - C_{\tau 1} Z - C_{\tau 2} \frac{P_k}{\varepsilon} Z \qquad (4.50)$$

Optimization studies have started using four coefficients, however, due to several reasons such as abundancy of coefficients of the certain model, calibration methodology and its parameters have created some issues. Therefore, the study is extended to five coefficients which lead to 3125 individual cases comprised of the combinations of the following coefficients, $C_{\varepsilon 1}$, $C_{\varepsilon 2}$, $C_{\tau 0}$, $C_{\tau 1}$, $C_{\tau 2}$.

These coefficients have been selected by carrying out sensitivity analysis and concerning about adaptation of an additional turbulent time scale.

4.5.Benchmark Cases for Turbulence Model Testing

An essential component of CFD simulations is turbulence modeling. The objective of turbulence models is to depict the complex behavior of turbulent flows and to provide insight into flow characteristics such as velocity fluctuations, turbulence intensity, and eddy structures. For the validation and evaluation of turbulence model efficacy, benchmark cases or test cases are utilized. This section provides a comprehensive analysis of the benchmark cases commonly used for testing turbulence models.

Benchmark cases act as standardized conditions for testing that enable researchers and engineers to evaluate and compare various turbulence models in an identical way. They serve as a benchmark for evaluating the precision, dependability, and applicability of turbulence models for a variety of flow configurations. Benchmark cases are essential for expanding turbulence modeling methods and assuring the quality and accuracy of CFD simulations.

Typical Benchmark Cases:

- *Channel Flow*: Channel flow is the flow between two parallel plates with an applied pressure gradient along the length of the channel. The benchmark case for channel flow involves estimating the mean velocity profile, Reynolds stresses, and other flow data. It is a fundamental test for turbulence models, especially wall-bounded flows.

- *Backward-Facing Step*: In the case of a backward-facing step, the flow downstream of a step-like obstruction expands abruptly. It is frequently used to assess models in complex flow patterns with separation, recirculation regions, and variations in wall shear stress. The benchmark case is designed for obtaining the reattachment length, characteristics of the recirculation area, and velocity profiles.

- *Flow Over a Circular Cylinder*: Flow over a circular cylinder is a typical benchmark case to evaluate turbulence models in the framework of bluff body flows. It entails simulating the flow around a cylinder, which displays complex vortex scattering and wake formation. This benchmark case involves obtaining drag and lift coefficients, the Strouhal number, and vortex-shedding frequency.

- *Jet Flows*: Jet flows, including plane or round jets, often serve as benchmark cases for turbulence modeling. They involve simulating the flow released from an orifice into an environment at rest. Priority here is placed on obtaining distribution of velocity, velocity decay on the centerline, the spreading rate of the jet, and turbulent mixing when evaluating a jet flow case.

4.5.1. Evaluation Metrics

Various evaluation metrics are utilized to quantitatively evaluate turbulence models using benchmark cases. These metrics help to quantify how well the turbulence models simulate the flow characteristics and compare model predictions against experimental or high-fidelity computational data. Here are some key evaluation metrics used for free shear and wall-bounded flows:

Free Shear Flows:

- *Centerline Velocity Decay* – Measures how accurately the model predicts the decay of the velocity along the centerline of a jet or wake compared to experimental data.
- *Spreading Rate* – Evaluates the model's ability to predict the spreading of a jet or wake in comparison to experimental observations.
- *Turbulence Intensity Profiles* – Compares the predicted turbulence intensity distribution across the jet or wake cross-sections with experimental data.

- *Vorticity Structure* – Assessing the vorticity structures and their evolution within the flow field against experimental observations.
- *Reynolds Stress Components* – Evaluates the accuracy of predicted Reynolds stresses in terms of the normal and shear components compared to experimental data.

Wall-Bounded Flows:

- *Boundary Layer Profile* – Compares the model-predicted velocity profiles near the wall (boundary layer) with experimental data or well-established empirical profiles like the logarithmic law of the wall.
- *Skin Friction Coefficient* – Evaluates the agreement between the model-predicted and experimentally measured skin friction coefficient along the wall.
- *Reattachment Length and Point* – Assesses the model's capability to predict the point of flow reattachment in separated flows and the length of the reattachment region.
- *Boundary Layer Thickness* – Evaluates the predicted boundary layer thickness in comparison to experimental data at different streamwise locations.
- *Pressure Gradient Effects* – Assesses the model's performance in predicting adverse pressure gradient flows or flows with different pressure gradients, comparing separation points and reattachment lengths.
- *Turbulence Intensity and Kinetic Energy* – Compares the predicted turbulence intensity profiles and turbulent kinetic energy distribution near the wall with experimental data.

General Metrics:

- *Root Mean Square Error (RMSE)* – Quantifies the deviation between the predicted values and the data used as a standard. It provides a comprehensive evaluation of the reliability of the turbulence model.
- *Correlation Coefficients* – Evaluates the linear relationship between model predictions and experimental data. High correlation values indicate good agreement.

- *Integral Length Scale* – Assesses the ability of the model to predict the size of coherent turbulent structures, comparing it with experimental observations.
- *Turbulent Energy Spectra* – Compares the energy spectra predicted by the model with experimental data, indicating the distribution of energy at different length scales.

These evaluation metrics help researchers and engineers assess the performance of turbulence models in capturing the essential features of free shear and wall-bounded flows, providing insights into the strengths and limitations of different modeling approaches.

4.5.2. Free Shear Flows

A free-shear jet is a form of fluid flow distinguished by the lack of velocity gradients perpendicular to the jet's axis. This indicates that all fluid particles in the jet travel at the same speed and in the same direction, without twisting or shearing. Free-jets are prevalent in nature and can be observed in phenomena such as the flow of the exhaust from a jet engine.

The stability of shear-free jets is an essential characteristic. There are no velocity gradients that could cause the jet to become unstable and fragment into smaller vortices or eddies, as all fluid particles in the jet are moving at the same speed and in the same direction. This renders shear-free jets optimal for a variety of applications, including fluid dynamics, aerospace engineering, and astrophysics.

Shear-free jets have been comprehensively studied in the framework of both laminar and turbulent flow, types of fluid flow characterized by smooth, non-turbulent motion, and chaotic, turbulent motion in fluid dynamics respectively. The equations of Navier-Stokes, which govern the motion of viscous fluids, can be used to characterize the velocity of fluid particles. By solving these equations for a shear-free jet, researchers can gain insight into the fluid flow's behavior and the factors that influence its evolution and stability.

In the disciplines of fluid dynamics, astrophysics, and engineering, shear-free jets are a fascinating and significant topic. By examining these flows, researchers can gain a better comprehension of the underlying physical principles that govern the behavior of fluids,

thereby aiding in the development of new technologies and applications in a variety of fields.

4.5.2.1.Plane Jet

The plane jet is a canonical flow configuration widely used as a benchmark case for validating and comparing various turbulence models in CFD. It represents a fundamental and well-understood flow, allowing researchers to assess the predictive capabilities of turbulence models in simulating complex turbulent behaviors.

A plane jet involves the continuous discharge of a fluid (usually air or water) from a nozzle into a quiescent environment. The jet emerges as a continuous, planar flow with a velocity higher than the surrounding fluid. The flow is often axisymmetric and uniform in the jet core region, simplifying the flow geometry for numerical simulations. As the jet exits the nozzle and interacts with the ambient fluid, it undergoes significant turbulence development, forming complex flow structures such as the potential core, shear layers, vortex rings, and mixing regions (Bailly & Comte-Bellot, 2015).

Researchers use the plane jet as a standard benchmark case to validate and compare the accuracy of turbulence models. The ability of a model to predict key flow features, such as the spreading rate, velocity profiles, turbulent kinetic energy distribution, and vortical structures, is assessed against experimental data. It helps in evaluating the performance and limitations of different turbulence models (RANS, LES, DES, etc.) in capturing the dynamics and evolution of turbulent flows under controlled conditions. The plane jet's-controlled nature allows for systematic parametric studies, enabling researchers to understand the sensitivity of turbulence models to various flow conditions, such as Reynolds number variations, jet-to-ambient density ratios, or different nozzle geometries. Detailed experimental and numerical investigations of the plane jet aid in unraveling the underlying mechanisms of turbulence generation, development, and decay within a well-defined flow configuration.

While the plane jet provides a controlled and simplified flow environment, challenges persist, especially regarding the accurate prediction of small-scale turbulent structures and their interaction with the jet's ambient surroundings. Additionally, the sensitivity of

the results to grid resolution and numerical schemes poses challenges in obtaining reliable and accurate simulations.

In summary, the plane jet serves as an essential benchmark case, offering insights into turbulence modeling and providing a standardized platform for comparing and improving turbulence models' predictive capabilities. Its controlled nature and well-documented experimental data make it a valuable tool for advancing our understanding of turbulent flows.

Figure 4.3 shows the important dimensions, regions and some characteristic parameters related to plane jet. The figure illustrates the presence of three distinct regions: the initial region, which corresponds to the potential core region; the transition region, which represents the interaction region; and the self-similar region.

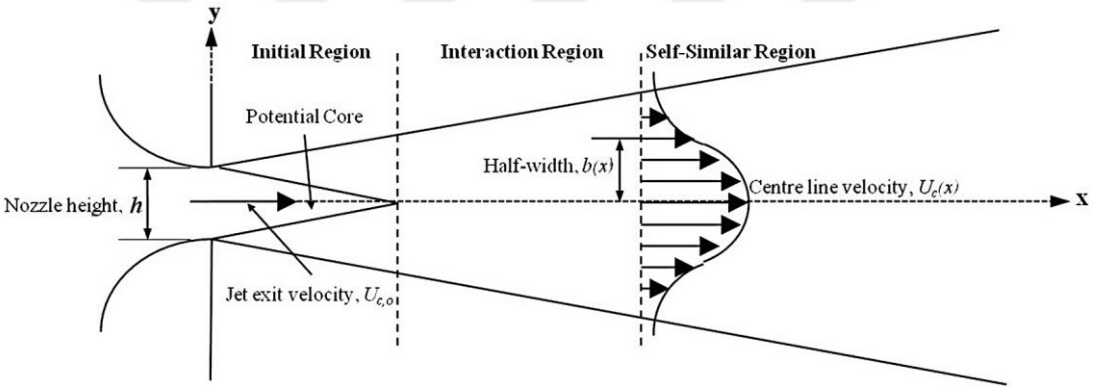

Figure 4.3. Structure of a Plane Jet (Shim et al., 2013)

Initial Region (Potential core section): The term "potential core section" in the context of a planar jet denotes the first segment of the jet characterized by a reasonably homogeneous and unhindered flow that is mainly untouched by external forces. This particular area is distinguished by certain flow characteristics and is vital for comprehending the formation and progression of the jet. Typically, the potential core length (x_P) is specified as the axial distance at which the core velocity equals 98% of the nozzle exit velocity (U_∞). In the case of a contraction nozzle emitting a subsonic isothermal plane jet with a Reynolds number between 1500 and 16500, this value can vary from 3d to 6d given x the axial coordinate as shown in **Figure *4.3***, d the transverse dimension of the nozzle or nozzle height, and Reynolds number as in equation 1.1 (Deo et al., 2008).

In the potential core, the flow is often axisymmetric and exhibits relatively uniform properties along the centerline of the jet. The flow velocity within the potential core is significantly higher compared to the ambient surroundings. This high-velocity region is relatively compact and central within the jet. Due to the limited influence of external factors, such as turbulence or viscous effects, mixing between the jet and the ambient fluid is relatively low in this region. The momentum of the jet's core is relatively well conserved, with minimal dissipation or distortion. The flow within the potential core remains relatively steady, providing a region where the flow characteristics are more predictable and simpler to model or analyze.

The potential core is highly sensitive to changes in operating conditions, nozzle geometry, and surrounding environment, making its accurate prediction challenging. Experimental measurements or numerical simulations aiming to capture the potential core require high-resolution techniques and accurate boundary conditions to represent this region effectively.

Transitional region (Interaction Region): The transitional region in a planar jet refers to the area where the initially laminar flow starts to undergo a transition to turbulence. This region lies between the potential core (the initial portion of the jet) and the fully developed turbulent region. The transitional region plays a significant role in understanding the evolution of the flow structure from laminar to turbulent states.

In this region, the flow experiences instabilities that lead to the breakdown of the laminar flow structures. These instabilities can arise due to various factors such as velocity gradients, Kelvin-Helmholtz instabilities, or perturbations induced by the surrounding environment. The flow in the transitional region gradually starts to exhibit characteristics of turbulence, including the formation of small-scale vortices and fluctuations in velocity and pressure. The symmetrical nature of the flow observed in the potential core starts to distort as the flow transitions toward turbulence. The once orderly and symmetric flow patterns become irregular and begin to break down. Small-scale turbulent structures begin to form, contributing to increased mixing between the jet and the surrounding fluid. This region is critical in studying the mechanisms and processes involved in the transition from laminar to turbulent flow. It provides valuable insights into the initiation and development of turbulence (Ma et al. 2000).

The transitional region is associated with the formation of localized turbulent spots or patches within the flow, which eventually grow and merge, leading to the complete establishment of turbulence in the flow. Accurately predicting and modeling the transitional region poses challenges due to the complexities associated with the transition process, including the interactions between laminar and turbulent flow structures. Understanding the transitional region is crucial in various engineering applications, including jet propulsion, mixing processes, and environmental fluid dynamics, where the control and prediction of turbulent flow behavior are essential.

The transitional region's behavior can vary significantly similar to potential core region based on external conditions, such as Reynolds number, nozzle geometry, and ambient conditions, making its characterization and prediction challenging. Capturing the transitional region accurately requires high-resolution experimental techniques or computational simulations capable of resolving the evolving flow structures with precision.

Self-similar region: In the context of a planar jet, the self-similar region refers to a portion of the flow where certain flow characteristics exhibit a consistent and uniform behavior across different streamwise locations. This region typically appears downstream of the potential core and the transitional zone and precedes the fully developed turbulent region. Flow variables such as velocity profiles or turbulent quantities may exhibit similarity when normalized appropriately.

Following the transitional region, the flow starts to regain certain ordered patterns or scaling behavior, allowing for the application of similarity laws or scaling relations to describe flow properties. Certain flow characteristics, such as mean velocity profiles or turbulent intensity profiles, might exhibit self-similarity when normalized using appropriate length and velocity scales. Flow features in the self-similar region tend to approach a universal behavior, implying that their functional forms or scaling laws become less sensitive to downstream variations.

The self-similar region provides an opportunity for researchers to employ scaling laws or similarity analysis to describe and predict certain flow properties, which simplifies the modeling and understanding of the flow. Observing the flow in the self-similar region

offers insights into how certain turbulent characteristics evolve as the flow progresses downstream towards a fully developed turbulent state.

Understanding the self-similar region provides insights into the universal behavior of certain flow characteristics, aiding in the development of simplified models or scaling relations applicable in various engineering applications. These insights can be used in fields like jet propulsion, mixing processes, and environmental fluid dynamics, among others. In summary, the self-similar region in a planar jet represents a part of the flow where certain flow characteristics exhibit a degree of uniformity or similarity along the streamwise direction, allowing for the application of scaling laws and providing insights into the flow evolution.

The mesh-independent grid structure for the plane jet case can be seen in **Figure 4.4**.

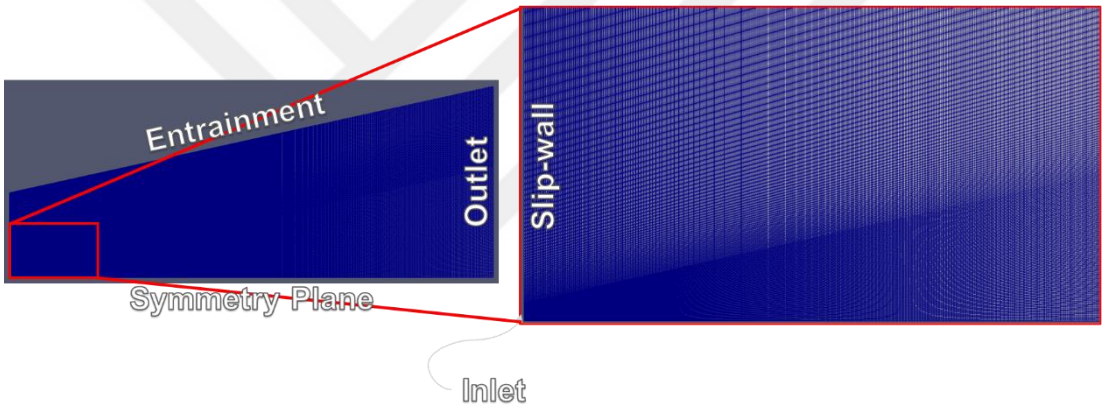

Figure 4.4. Selected grid structure of the Plane Jet case

Some of the early studies by use of a hot wire anemometry were performed by various researchers (Bradbury, 1965; Gutmark & Wygnanski, 1976; Heskestad, 1964; Miller & Comings, 1957; Robins, 1973; Van der Hegge Zijnen, 1958). According to the findings, jets that are released into stagnant environments eventually form self-similar states in which their time-averaged quantities may be expressed by only one length scale and one velocity. In other words, Reynolds stress and the mean velocity distribution must not depend on the streamwise coordinate "x" as these scales are used to normalize them. A turbulent flow is said to be self-similar when some or all of its normalized statistical properties such as half-width of the jet (spreading rate $= \frac{\partial y_h}{\partial x}$) become constant.

Mean axial velocity distribution achieve self-similarity before the turbulence entities. However, there is no consensus on where this state is reached; it varies from x/d = 40 to 100. The calculated spreading rates exhibit a high degree of concordance with a value of $\frac{\partial y_h}{\partial x}$ of 0.109.

TKE in the vicinity of the nozzle tip increases depending on its high production rate in regions characterized by a large velocity gradient. This high TKE produced in the high shear area diffuses towards the jet's center and edge as it expands.

The turbulence quantity measurements are widely dispersed. LDA measurement of Ramaprian and Chandrasekhara (Ramaprian & Chandrasekhara, 1985) gave the second lowest maximum shear stress level of $\frac{\overline{uv}_{max}}{U_{cl}^2} = 2$ with the highest spreading rate of 0.112 (**Table 4.3**). For jets in stagnant environments, the self-similar form is regarded as universal and independent of the jet's initial conditions. Consequently, uniform TKE level ($k_j = 1/2(U_0 I)^2$ and a flat velocity profile at the jet nozzle, are selected as initial conditions, where *I,* denotes turbulence intensity.

Table 4.3. Comparison of experimental and model results for incompressible planar jet

Investigator	Spreading Rate	$\frac{\overline{uv}_{max}}{U_{cl}^2}$	Remarks
Miller & Comings (Miller & Comings, 1957)	0.097	0.025	CTA
Van der Hegge Zijnen (Van der Hegge Zijnen, 1958)	0.095	-	HWA
Bradbury (Bradbury, 1965)	0.109	0.024	HWA
Heskestad (Heskestad, 1964)	0.11	0.020	HWA
Gutmark & Wygnanski (Gutmark & Wygnanski, 1976)	0.11	0.024	HWA
Everitt & Robins (Everitt & Robins, 1978)	0.09 - 0.11	0.019	CTA

Ramaprian & Chandrasekhara (Ramaprian & Chandrasekhara, 1985)	0.112	0.02	LDA
$k-\varepsilon$ model	0.108	0.022	
$SST\ k-\omega$ model	0.113	0.0215	
$RNG\ k-\varepsilon$ model	0.117	0.029	
$k-\varepsilon-\tau$ model	0.109	0.0216	

The computed mean velocity distribution for plane jets in the area of self-similarity is displayed in **Figure 4.5** in the axial direction. It is assessed in comparison with the experimental results of Robins (Robins, 1973), and predictions of the other two-equation models considered in the current manuscript.

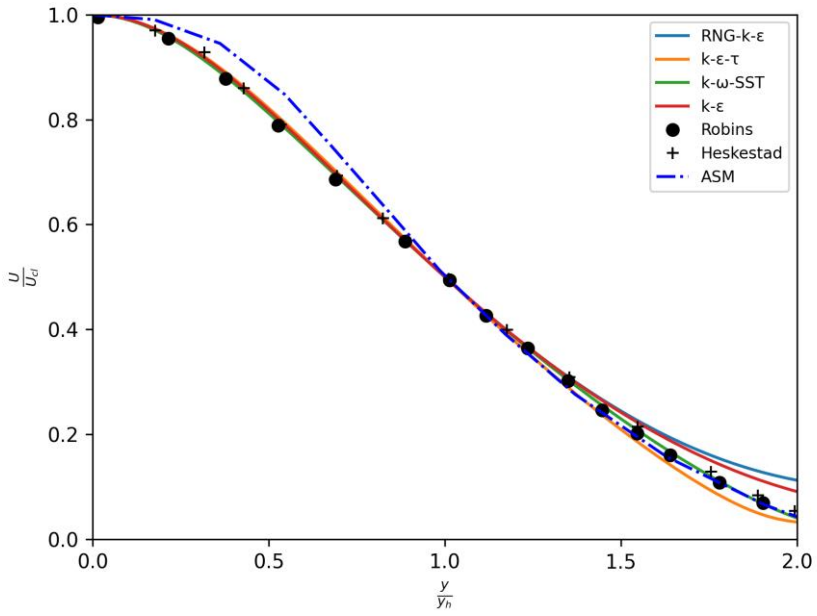

(**a**)

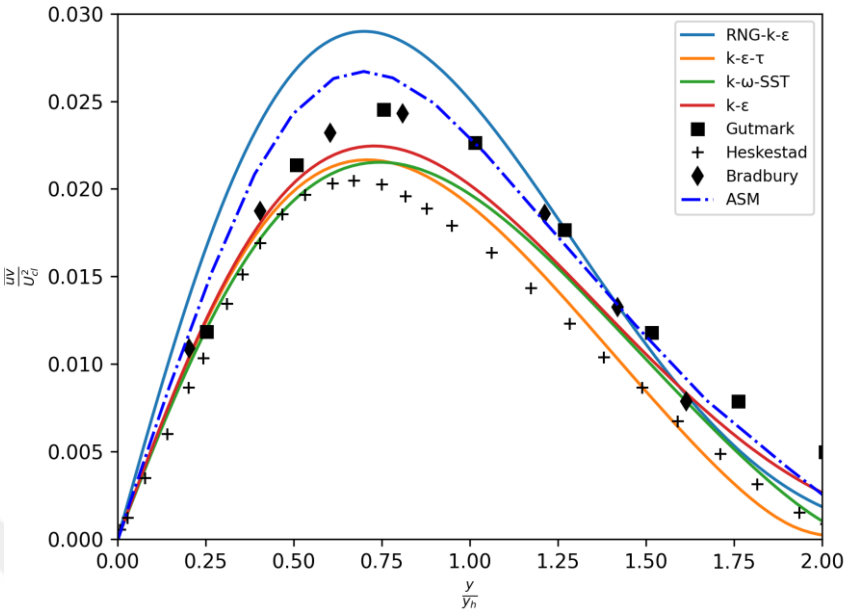

(b)

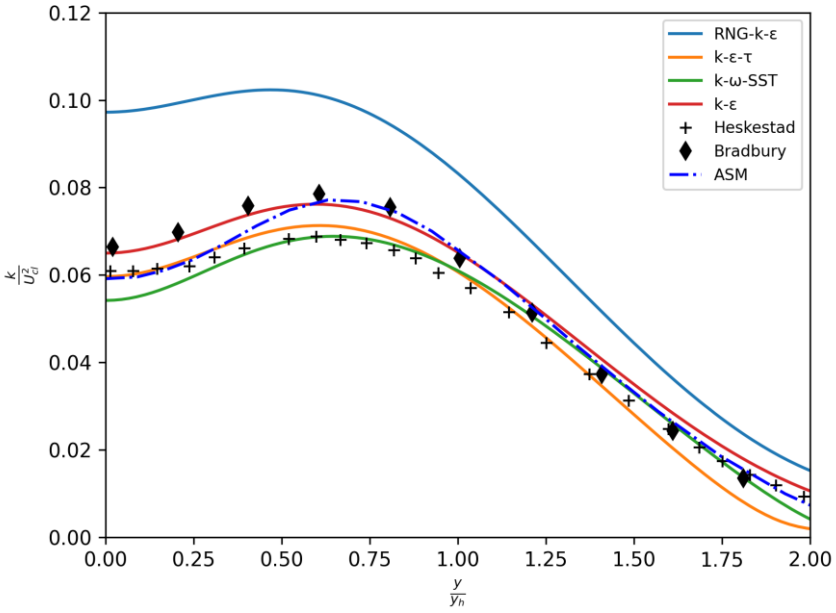

(**c**)

Figure 4.5. Prediction of (a) mean axial velocity, (b) shear stress and (c) TKE profiles for plane jets.

Figure 4.5 presents a comparison of the shear stress "$\overline{uv}$" and TKE data from Gutmark and Wygnanski (Gutmark & Wygnanski, 1976) and Bradbury (Bradbury, 1965) respectively. The modified k-ε-τ model provides better agreement for shear stress and complies with TKE patterns observed in both experimental findings documented in the scientific literature closer to the centre of the jet, and slightly underestimated towards the twice distance of y_h.

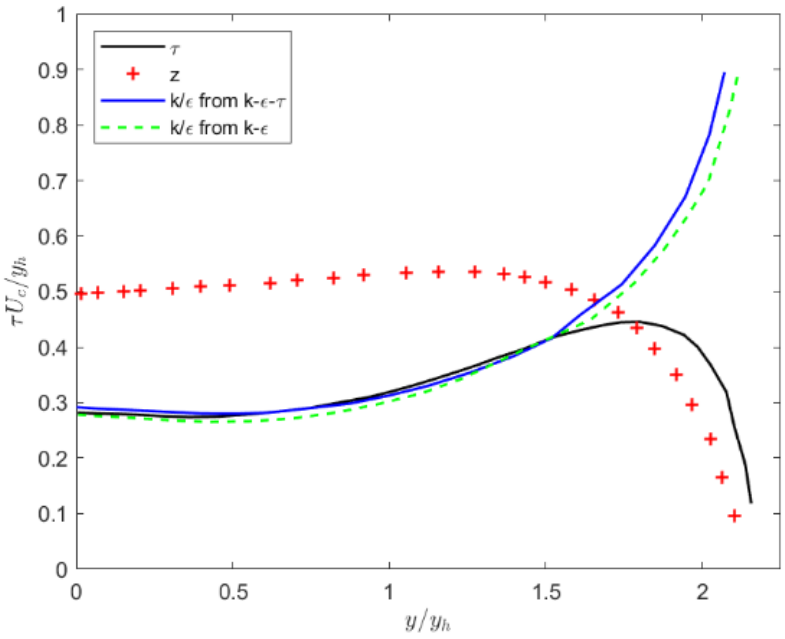

Figure 4.6. Estimation of z-profiles and turbulence time-scale in plane jet.

Table 4.3 displays the spreading-rates as well as the maximum shear stress levels achieved for the plane jet in comparison to different experimental results and values determined using various two-equation models. It is evident that the k-ε-τ model predicts spreading-rate far more accurately with a value of 0.109, and the maximum shear stress levels are also consistent with the revised model. This is not unexpected considering that the coefficients are modified in order to achieve optimal agreement among the turbulence quantities, spreading rate, and mean velocity.

The time-scale τ can be normalized in two ways, either by $\tau^* = \frac{\tau U_{CL}}{y_h}$ or $z = \frac{\varepsilon\tau}{k}$. The latter can also be expressed as the ratio of two different time scales and, it should be comparable to the reciprocal of $C_{\varepsilon 2}$ of the standard k-ε model (1/1.92). Figure 4.6 shows time-scales

τ^* and z respectively. τ^* is compared with values of $\frac{k}{\varepsilon}$ (times $\frac{1}{C_{\varepsilon 2}}$of the k-ε model) predicted from both the k-ε and k-ε-τ models. Time-scales of $\frac{k}{\varepsilon}$ from both models go in parallel, the one predicted from the k-ε-τ model being 4% higher, across the jet. Time-scale τ^* starts with the same value of $\frac{k}{\varepsilon}$ of the k-ε model in the centre of the jet and slightly increases until about $1.5y_h$ by yielding at the maximum a 7% higher value between $0.9y_h$ to $1.4y_h$. Although the k-ε model suggests that its $C_{\varepsilon 2}$ coefficient depends only on decay exponent, variation of *"z"* across the jet implies that the coefficient $C_{\varepsilon 2}$ of the k-ε model would not be a true constant. The TKE budget as found by the modified k-ε-τ model is compared in Figure 4.7 with the Bradbury's energy balance which is found to be more consistent than Gutmark's according to Rodi (Rodi, 1975). Agreement is again very good and consistent with the above findings.

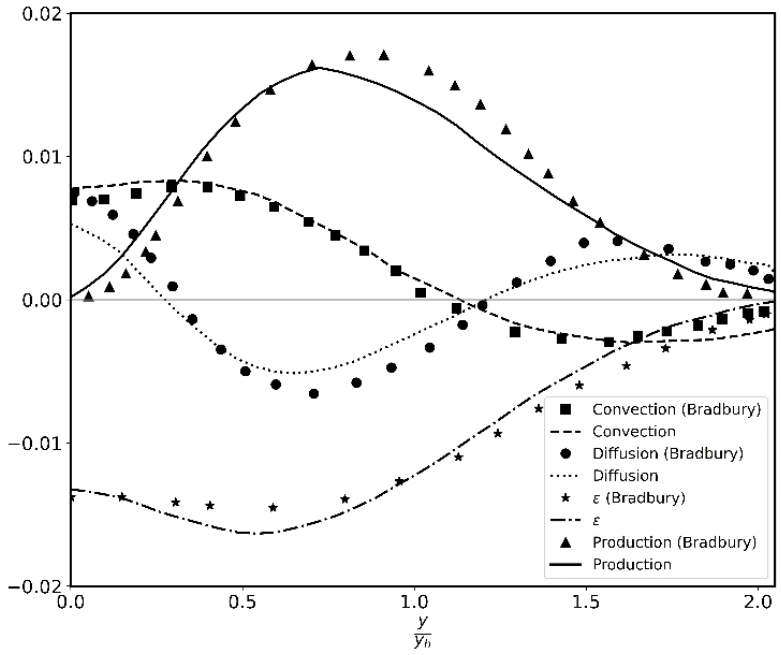

Figure 4.7. Plane jet energy budget.

4.5.2.2.Round Jet

Round jets, often referred to as axisymmetric jets, represent a fundamental and extensively studied configuration in fluid mechanics. They are characterized by the flow of fluid discharged from a circular orifice into a surrounding medium, exhibiting

rotational symmetry around the jet's axis. This configuration finds applications across various engineering fields, including aerospace, environmental science, combustion, and industrial processes, due to its relevance in understanding fluid dynamics, mixing phenomena, and turbulent flow behaviors (Bailly & Comte-Bellot, 2015).

Axisymmetric jets display distinctive flow characteristics that evolve as the jet travels downstream. Upon exiting the nozzle or orifice, the initial region of the jet, known as the potential core, is marked by coherent and high-velocity fluid motion. In this region, the jet's velocity profile is approximately self-similar, implying that the jet maintains its shape and characteristics without significant changes. As the flow progresses downstream, the jet's radial spreading occurs due to the influence of surrounding air or fluid, resulting in velocity decay and expansion of the jet cross-section. The development of axisymmetric jets is typically categorized into distinct flow regimes based on the jet's characteristics and the surrounding flow environment. The initial region, the potential core, remains well-defined within a short distance from the nozzle exit. Beyond the potential core, the jet enters a region of transition where the flow becomes susceptible to external influences, leading to a gradual decay of the coherent core and the onset of turbulent mixing. Further downstream, the jet enters a turbulent self-similar region, characterized by enhanced mixing, momentum decay, and broadening of the jet's profile. In this region, the flow becomes increasingly influenced by turbulence, resulting in complex vortical structures, fluctuations, and entrainment of surrounding fluid into the jet core. Understanding round jet characteristics is crucial in various applications. In aerospace engineering, axisymmetric jets play a vital role in propulsion systems, exhaust flow dynamics, and aerodynamic studies. In environmental engineering, they are crucial in modeling pollutant dispersion, air entrainment, and water quality assessments. In combustion studies, round jets serve as a fundamental configuration for investigating combustion behavior, flame stabilization, and fuel-air mixing processes in combustion chambers (Batchelor & Gill, 1962).

Experimental techniques such as PIV, HWA, and LDV are commonly employed to analyze axisymmetric jet characteristics, including velocity profiles, turbulence intensity, and flow structures. Numerical simulations, such as CFD, are also extensively utilized to

model round jets, providing insights into complex flow phenomena and aiding in the design optimization of engineering systems.

Round jets, or axisymmetric jets, represent a fundamental flow configuration in fluid mechanics, offering insights into various aspects of fluid dynamics, turbulence, and mixing phenomena. Their relevance spans across numerous engineering applications, highlighting their significance in understanding flow behaviors, turbulence modeling, and designing efficient engineering systems.

The mesh-independent grid structure for the round jet case can be seen in **Figure 4.8**.

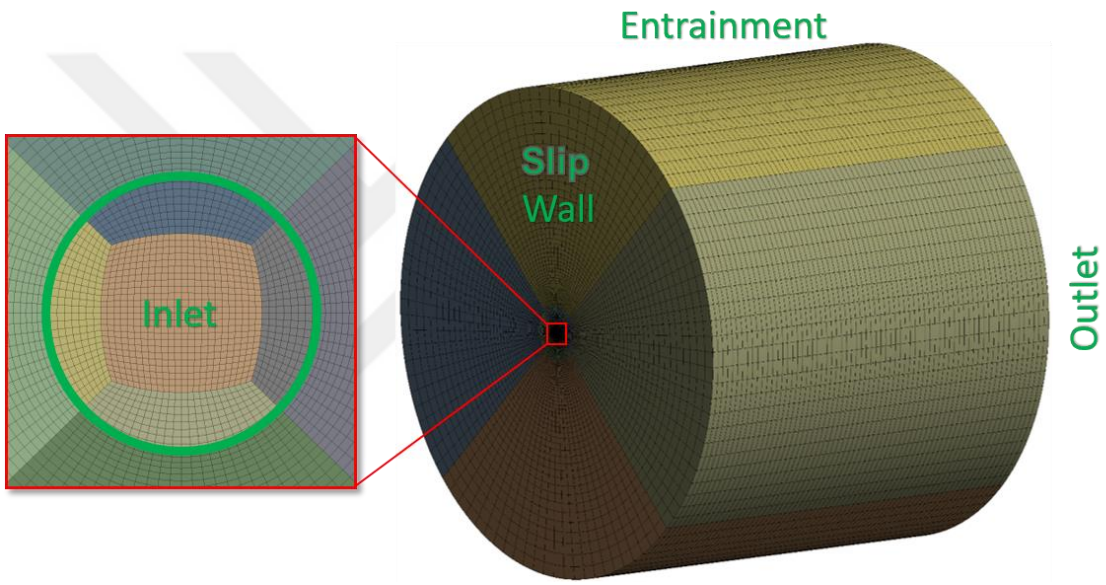

Figure 4.8. Selected grid structure of the Round Jet case.

Table 4.4 gives a summary of experiments and simulation outcomes of the turbulence properties in the self-similar area. Compared to a plane jet, a round jet spreads slower, according to these observations, and takes between 50 and 70 diameters to achieve its self-similar form. Hussein and George (Hussein & George, 1989) reported a peak value of about $\frac{\overline{uv}}{U_{cl}^2} = 0.021$ at 70 *x/D* and gave a value of 0.094 for the spreading rate although early research indicates a spreading-rate of $\frac{dy_h}{dx} = 0.086$.

The traditional models consistently anticipate higher spreading rates for the axisymmetric case, also known as the "plane jet/round jet" anomaly, which was initially documented by Rodi and Spalding (Rodi & Spalding, 1970) in their analysis using the *k*-k_l model.

However, the round jet spreading rates predicted by the *SST k-ω* and *k-ε* models are around 28% too high, while the *k-ε-τ* model (applying the identical model parameters to the plane jet) provides a considerably closer value of 0.089. *Realizable k-ε* model is close behind *k-ε-τ* model in terms of spreading rates with a value of 0.088.

Table 4.4. Comparison of experimental and model results for incompressible axisymmetric jet

Investigator	Spreading Rate	$\frac{\overline{uv}_{max}}{U_{cl}^2}$	Remarks
Wygnanski & Fiedler (Wygnanski & Fiedler, 1969)	0.086	0.0165	HWA
Rodi (Rodi, 1972)	0.086	0.0186	HWA
Capp (Capp, 1983)	0.095	-	LDA
Panchapakesan & Lumley (Panchapakesan & Lumley, 1993)	0.096	0.021	moving HW
Taulbee et al. (Taulbee et al., 1987)	0.094-0.102	0.021	LDA-HWA
Hussein & George (Hussein & George, 1989)	0.094	0.021	moving HW
$k-\varepsilon$ model	0.120	0.025	
$SST\ k-\omega$ model	0.121	0.028	
$Realizable\ k-\varepsilon$ model	0.088	0.023	
$k-\varepsilon-\tau$ model	0.089	0.027	

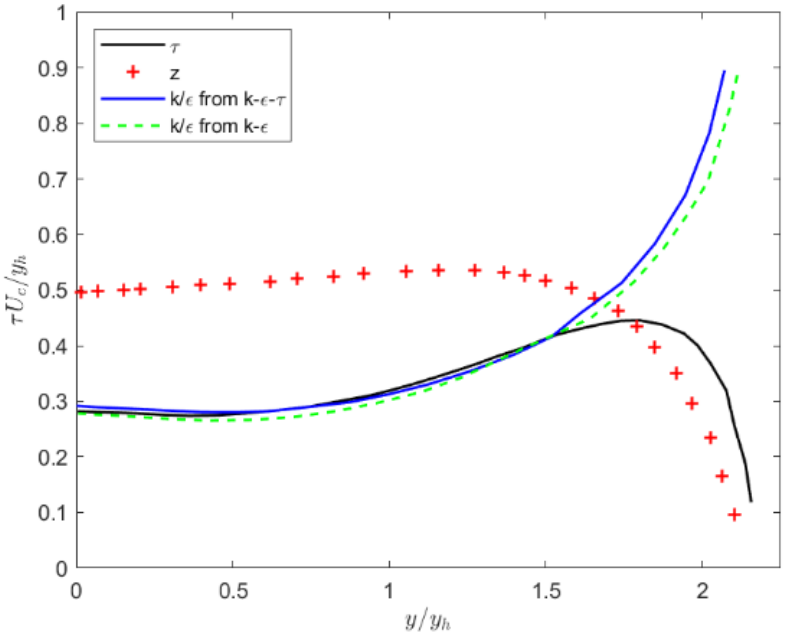

Figure 4.9. Estimation of z-profiles and turbulence time-scale in round jet.

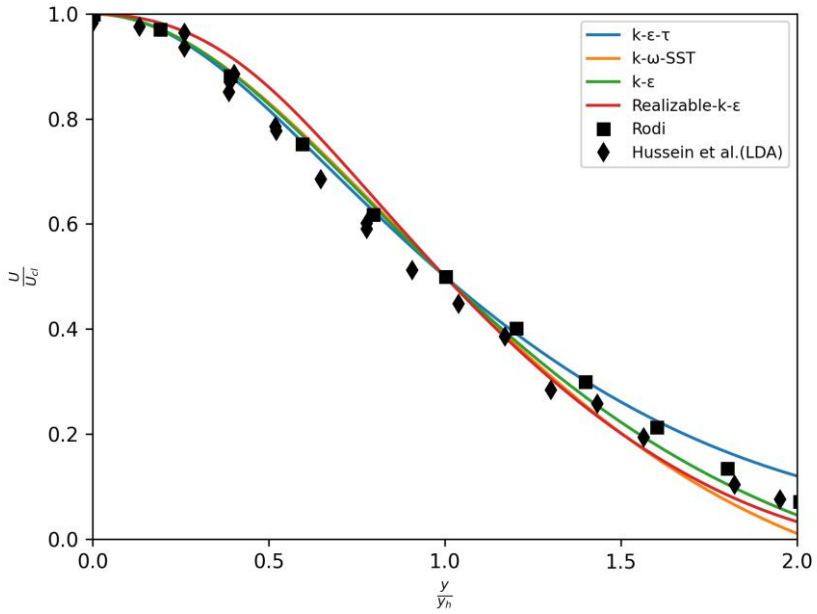

(**a**)

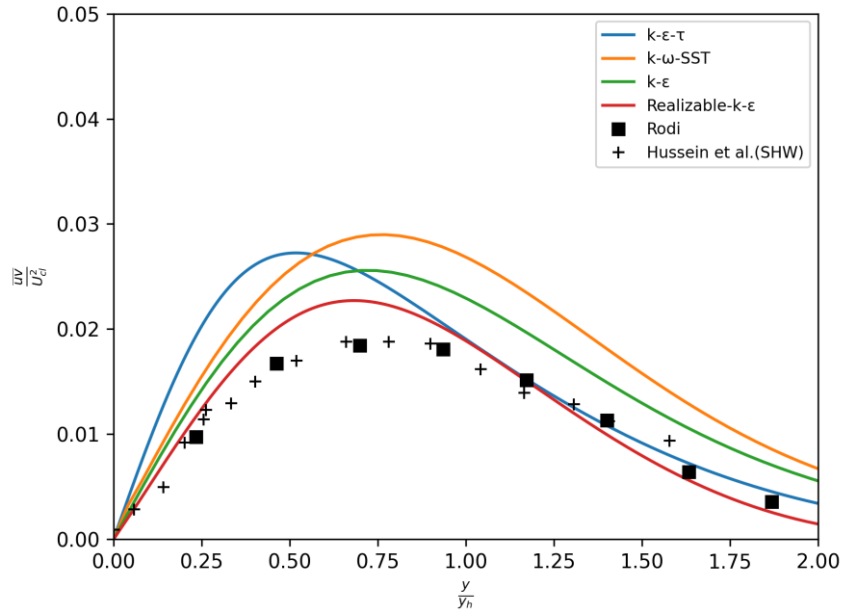

(b)

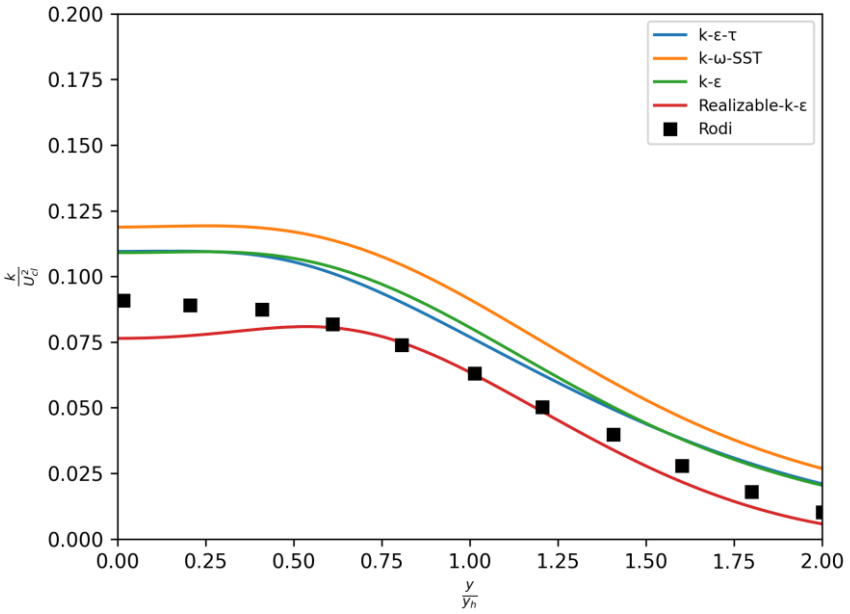

(**c**)

Figure 4.10. Prediction of (a) mean axial velocity, (b) shear stress and (c) TKE profiles for round jets.

The predicted mean axial velocity, shear stress, and TKE profiles for axisymmetric jets are compared to the work of Rodi (Rodi, 1972) at the self-similar region in **Figure 4.10**.

It is evident that consistency of the k-ε-τ model outputs are quite satisfactory. The maximum shear stress profiles are projected to be 22% higher by the k-ε model that is compatible with the prediction of its spreading rate. k-ε-τ model, after making a slight hump which is not consistent with experiments, at about $0.5y_h$, it levels with the data from the measurements of Rodi (Rodi, 1972), and Hussein et al. (Hussein et al., 1994), thereafter the agreement with it is quite good.

Interestingly, the aforementioned "plane jet/round jet" anomaly does not appear in the k-ε-τ model. Unlike the close error margin considering the plane jet, TKE profiles are overestimated by about 9% from the jet axis in the first quarter.

On the other hand, TKE predictions of *SST* k-ω model are much higher than the rest of the models considered in the manuscript in terms of both shear stress and TKE distributions.

Turbulence time-scale τ^* level is consistently higher than the k-ε level from the k-ε-τ model up to the outer edge of the jet by about 5% at the jet centre, and 12% at $1.4y_h$ (**Figure 4.10**), but agrees with $\frac{k}{\varepsilon}$ from the k-ε model. It can also be observed in the same figure that the z-level is increased slightly (7-8%) compared to plane jet **Figure 4.9**. This could be due to an increased energy dissipation rate predicted in the round jet as can be seen in the energy budget in **Figure 4.11**. It can also be seen that convection and production terms in the energy budget are predicted reasonably well compared with the measurements. The change of sign in the diffusion term, close to the centre of the jet, is consistent with the predictions of TKE. However, this is not supported by the experiments.

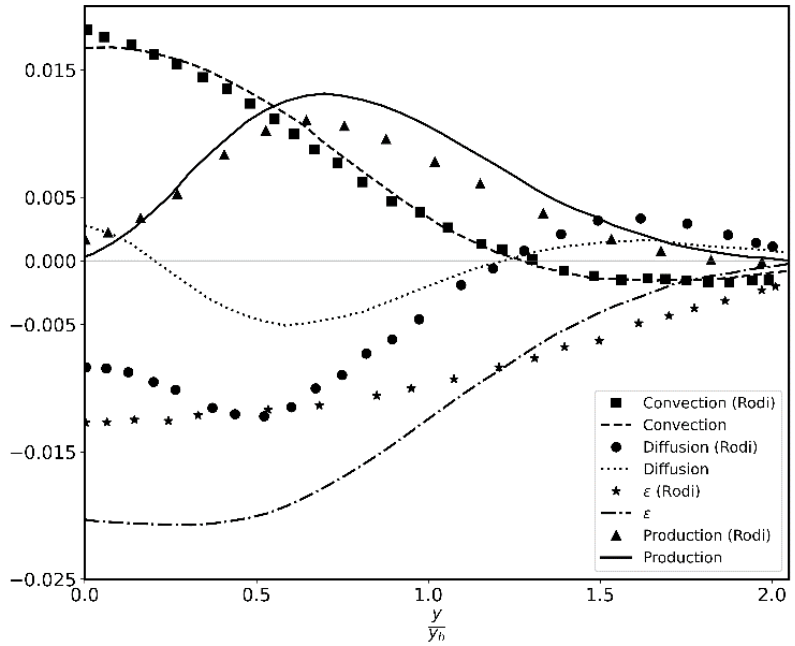

Figure 4.11. Round jet energy budget.

4.5.2.3.Plane Far Wake

The plane far wake, considered a benchmark case in fluid mechanics, represents the flow generated behind an object moving steadily through a fluid medium. This wake configuration provides valuable insights into the dynamics of vortices shed by an object and their subsequent evolution downstream. The study of the plane far wakes aids in understanding flow patterns, vorticity structures, and turbulence phenomena, offering significant implications in various engineering applications, including aerodynamics, marine engineering, and renewable energy.

The 2D wake flow is characterized by the formation of vortices or eddies trailing an object moving steadily in a fluid. The flow near the obstacle is generally complex and strongly depends on the shape of the obstacle. In the far wake region, where the flow has sufficiently developed away from the object, the wake exhibits a two-dimensional nature, allowing for simplified analysis and modeling. The wake structure comprises a series of vortices that propagate downstream, influenced by the object's shape, Reynolds number, and the flow conditions.

The wake development begins with the shedding of vortices from the object's surface into the wake region. These vortices interact and evolve downstream, leading to the formation of a distinctive pattern characterized by alternating vortices known as the von Kármán vortex street. In the plane far wake, the vortices exhibit periodic shedding and maintain their two-dimensional structure, facilitating easier observation and analysis compared to three-dimensional wake flows (Gunasekaran & Altman, 2021).

The study of the plane far wake holds significant importance in various engineering disciplines. In aerodynamics, it provides fundamental insights into the flow behavior behind bluff bodies, aiding in the design of streamlined structures, reducing drag, and enhancing aerodynamic performance. In marine engineering, the understanding of wake dynamics contributes to ship design optimization, propeller efficiency, and minimizing wake-induced vibrations. Additionally, in renewable energy, wake studies are crucial in wind turbine efficiency, wake effects, and wind farm layout design.

Experimental techniques such as flow visualization using smoke, dye, or PIV are employed to study the wake structure, shedding frequency, and vortex formation. Numerical simulations, particularly CFD, play a crucial role in modeling wake flows, allowing detailed analysis of flow characteristics, vortex shedding, and wake evolution. These investigations provide valuable data for validating theoretical models and enhancing our understanding of wake dynamics.

The plane far wake, a benchmark case in fluid mechanics, offers fundamental insights into the complex flow phenomena occurring behind an object in a fluid. Its two-dimensional nature simplifies analysis and modeling, making it a valuable tool for understanding wake dynamics, vortex shedding, and turbulence. The study of 2D wake flow finds widespread applications in engineering, shaping the design and optimization of various systems and structures.

The mesh-independent grid structure for the plane far wake case can be seen in **Figure 4.12**.

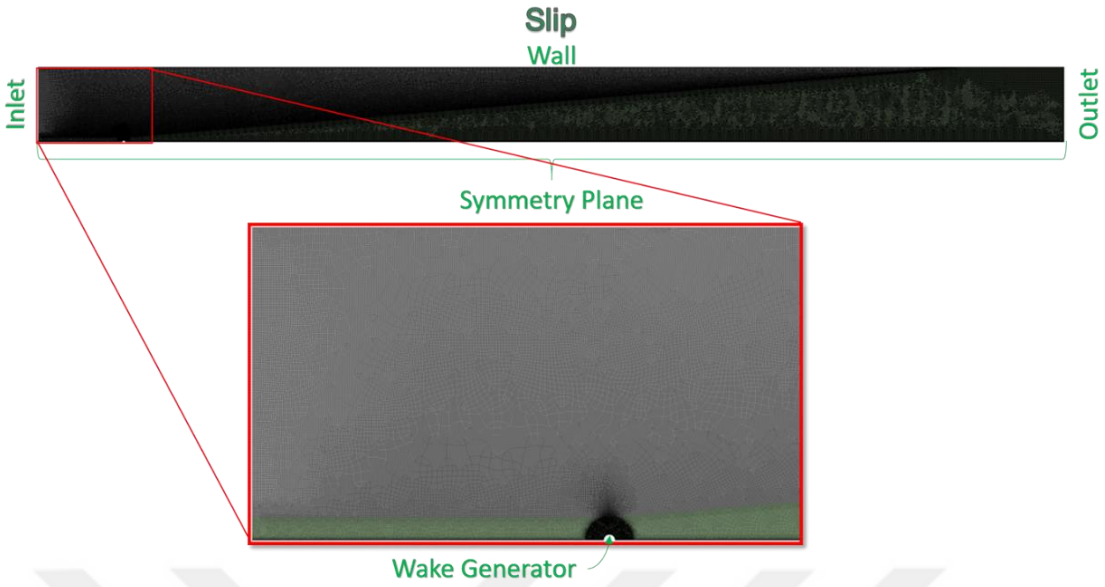

Figure 4.12. Selected grid structure of the Plane Far Wake case

It is possible to define a normalized spreading parameter for the wake as $S_w = \frac{\left(\frac{U_E}{U_o}\right)dy_h}{dx}$ where U_E is the outer stream velocity and U_o is the velocity deficit at the centreline of the wake (Newman, 1967; Zhou et al., 1998). Simulation results proved that, the measurements of Wygnanski et al. (Wygnanski et al., 1986) seemed to be the most reliable. They state that the Reynolds number calculated by using the cylinder diameter equals to 1360 and that the similarity zone begins at x/D>400 in the wake of the cylinder that has a certain diameter (D). Their similarity research suggests that the parameter for spreading must have a specific value, irrespective of the wake generator type. Furthermore, Louchez et al. (Louchez et al., 1985) asserted that the plane wake reaches a universal, self-sustaining form that is independent of the initial body when it is sufficiently far downstream, depending on the self-preserving properties demonstrated by second order moments. However, measurements of Wygnanski et al. (Wygnanski et al., 1986) suggested that the developing behaviour and asymptotic structure of plane wake can be impacted by the form of the wake generator, and this was one of the causes of the disagreement observed by different workers.

Table 4.5. Comparison of experimental and model results for plane far wake

Investigator	Spreading Parameter	$-\frac{\overline{uv}_{max}}{U_{cl}^2}$
Townsend (Townsend, 1949)	0.098	0.051
Ermshaus (from Ramaprian & Chandrasekhara (Ramaprian & Chandrasekhara, 1985))	0.089	-
Everitt & Robins (Everitt & Robins, 1978)	0.096	0.037
Sreenivasan & Narasimha (Sreenivasan & Narasimha, 1982)	0.092	-
Wygnanski et al. (Wygnanski et al., 1986)	0.082	0.048
k-ε model	0.077	0.036
$SST\ k-\omega$ model	0.079	0.042
$RNG\ k-\varepsilon$ model	0.099	0.046
k-ε-τ model	0.081	0.039

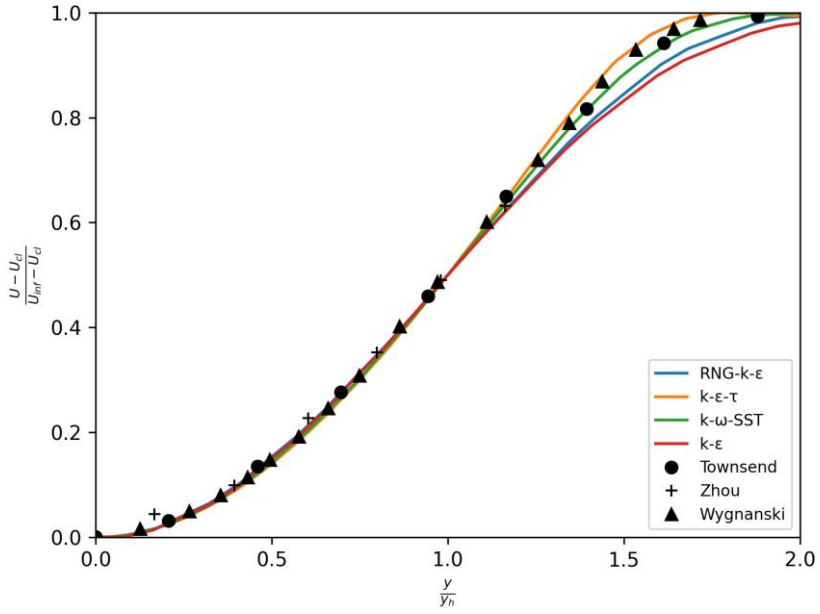

(**a**)

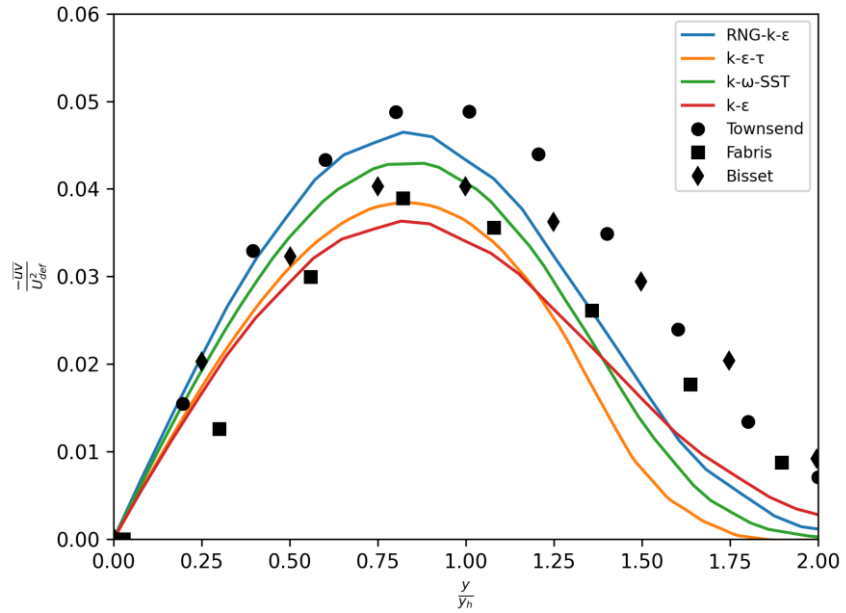

(b)

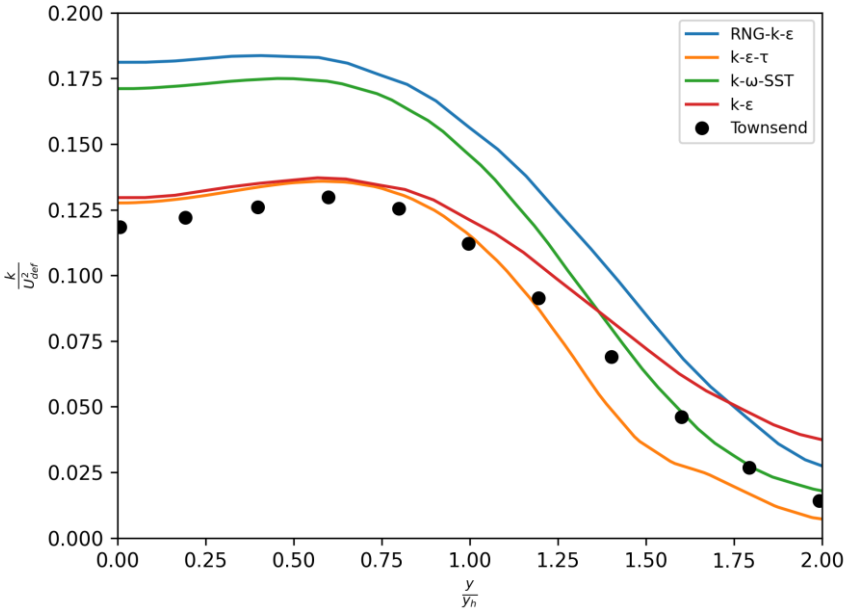

(**c**)

Figure 4.13. Mean axial velocity, $-\overline{uv}$ shear stress and k profiles for plane far wake (Bisset et al., 1990; Fabris, 1979; Townsend, 1949; Zhou et al., 1998)

It is particularly challenging to estimate both weak and strong shear flows using a pair of coefficients, particularly when employing eddy-viscosity models. The phenomenon

known as "weak-strong shear flow" is thought to be induced by the dissipation rate equation in its simulated form. **Table 4.5** presents a compilation of experimental and projected values for the wake spreading parameters in the aftermath of the wake generator, as determined by the typical two-equation models and *k*-*ε*-*τ* model. Regarding the experiments of Wygnanski et al. (Wygnanski et al., 1986), the modified *k*-*ε*-*τ* model underestimates the this spread parameter by less than 2%, suggesting a considerably better result compared to the significant underestimation by the *k*-*ε* and *SST k*-*ω* models.

As can be seen in **Figure 4.13** mean axial velocity profile for the far wake is well predicted, and the result obtained is very similar to that of other models. Despite a 23% lower estimation of maximum shear stress level than experiments (Wygnanski et al., 1986), the modified k-ε-τ model yielded a better value than the k-ε model, which underestimated it by 33%. This finding aligns with the comparative evaluation of the models' spreading parameter performance. Moreover, TKE profiles are predicted within 3% deviation close to the centre of the wake, up to the point of 1.2 y_h. Conversely, throughout the interval of 0-1.2 y_h, shear stress profiles are underestimated by approximately 15-30 percent, yielding a reduced level of concurrence in comparison to the other models considered in this research. When compared to experimental behavior, both turbulence energy profiles and shear stress appear to cease instantly near the outer edge.

Considering the results, the channel flow-trained and calibrated *k*-*ω*-*τ* model performed better on capturing the TKE however, underpredicted shear stress compared to SST *k*-*ω* which is also the same condition for *k*-*ε*-*τ* on plane far wake case.

Figure 4.14, **Figure 4.15**, and **Figure 4.16** shows the *k*-*ω*-*τ* model performance on given turbulence entities for plane far wake case.

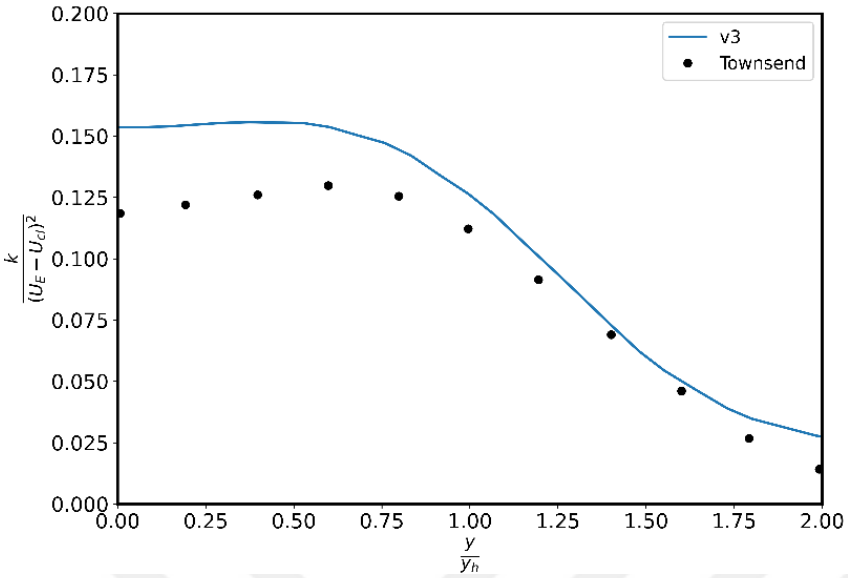

Figure 4.14. Normalized k profiles for plane far wake using v3 of k-ω-τ model.

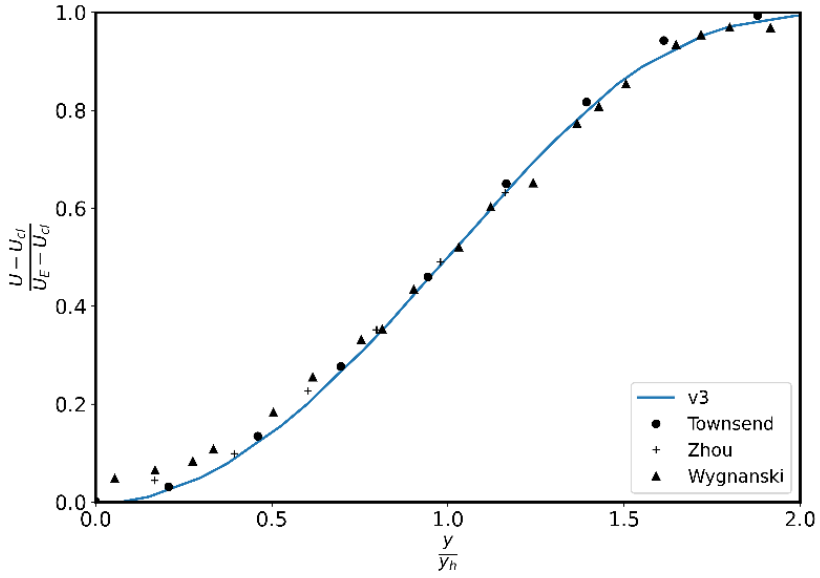

Figure 4.15. Mean axial velocity profiles for plane far wake using v3 of k-ω-τ model.

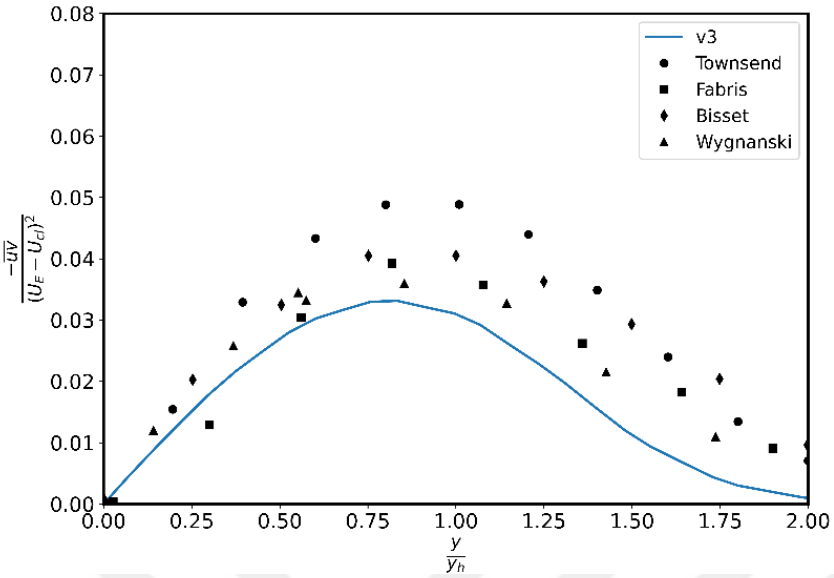

Figure 4.16. $-\overline{uv}$ shear stress profiles for plane far wake using v3 of k-ω-τ model.

On the other hand, where the isotropic models fail to sense the variation of the values of diagonal terms of the Reynolds stress tensor, *R-ε-τ* model shows better estimation which can be seen from the figures below.

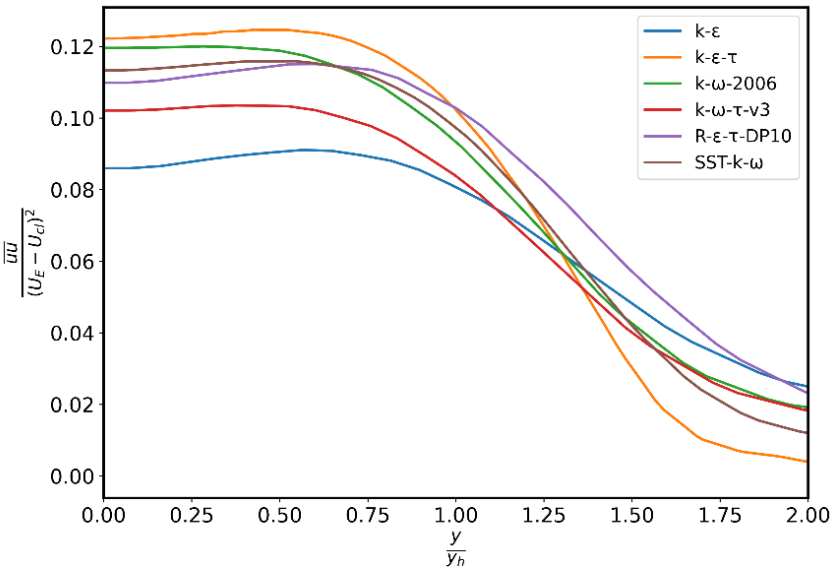

Figure 4.17. $\overline{uu}$ stress profiles for plane far wake using v3 of *R-ε-τ* model

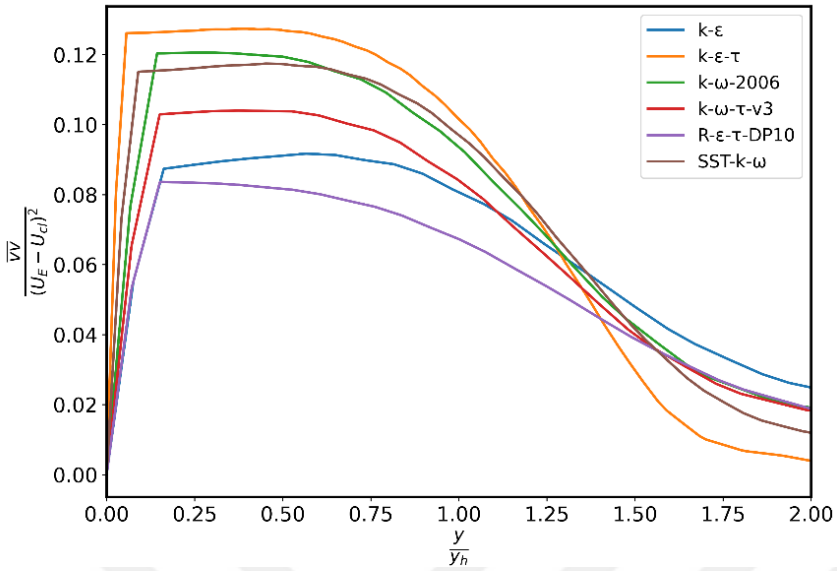

Figure 4.18. $\overline{vv}$ stress profiles for plane far wake using v3 of *R*-ε-τ model

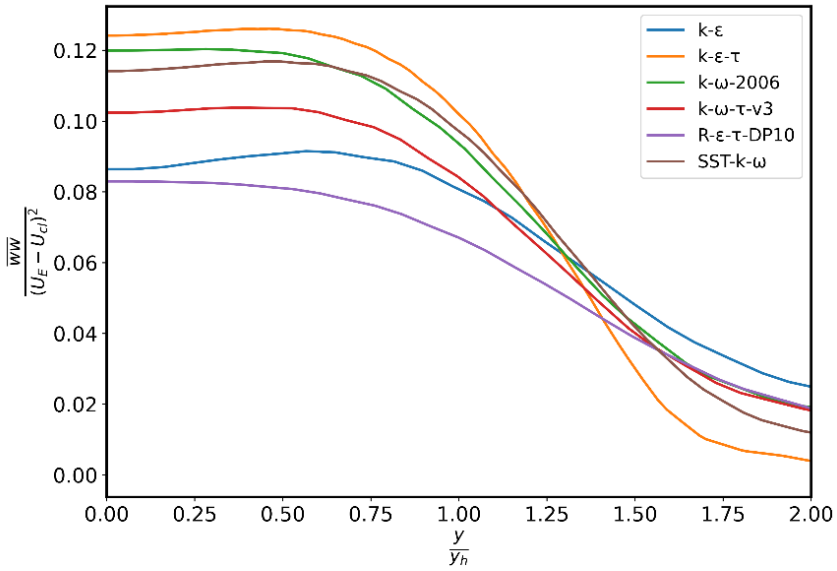

Figure 4.19. $\overline{ww}$ stress profiles for plane far wake using v3 of *R*-ε-τ model

4.5.3. Confined (Wall-Bounded) Flows

Confined flows, also known as wall-bounded flows, refer to the passage of fluid within a confined space, such as between solid boundaries or within pipes, channels, or ducts. These fluxes are of great interest to the field of fluid dynamics due to their numerous

practical applications. This section intends to provide a comprehensive analysis of confined flows, including their properties, mathematical descriptions, and applications.

Wall-bounded flows are characterized by the proximity of solid surfaces, leading to the formation of boundary layers. These boundary layers experience velocity gradients, viscous effects, and interactions between the fluid and the wall, influencing flow behavior. Key characteristics include flow separation, boundary layer growth, and the development of coherent structures within the flow.

Studying wall-bounded flows is crucial for developing and validating turbulence models due to their relevance in various engineering applications. These flows serve as fundamental test cases for model development and validation, aiding in understanding turbulence, boundary layer dynamics, and flow transition, leading to improved predictive capabilities in CFD simulations.

Typical benchmark cases of confined flows can be listed as below:

- *Flat-Plate Boundary Layer* – A flow over a flat plate used to study laminar to turbulent transition, boundary layer development, and skin friction.
- *Channel Flow* – A flow between parallel plates, relevant for studying wall-bounded turbulence, velocity profiles, and pressure distributions.
- *Pipe Flow* – Fluid flow within a cylindrical pipe, essential in understanding fully-developed turbulent flows, wall shear stress, and flow characteristics.
- *Plane Poiseuille Flow* – Laminar flow between parallel plates with a constant pressure gradient, significant for validating numerical methods and understanding laminar flows.
- *Axisymmetric Jet Impingement* – The flow generated when a jet impacts a surface, essential for heat transfer studies, cooling applications, and flow visualization.
- *Square Duct Flow* – A duct with a square cross-section, providing insights into secondary flows, vortex structures, and turbulence modeling.
- *Backward-Facing Step* – Study of flow separation and reattachment behind a step, significant for understanding separation bubbles and recirculation zones.
- *Curved Pipe Flow* – Fluid flow through curved pipes, crucial for investigating secondary flows, centrifugal forces, and turbulence characteristics.

- *Wall Jets* – Flow parallel to a wall with boundary layer development, important in studying spreading rates, velocity profiles, and shear layer dynamics.
- *Taylor-Couette Flow* – Flow between two rotating concentric cylinders, relevant for investigating shear-driven instabilities, transition to turbulence, and vortical structures.

Wall-bounded or confined flows play a pivotal role in fluid mechanics and turbulence research, providing crucial insights into boundary layer phenomena, turbulence modeling, and flow behavior near solid surfaces. These benchmark cases offer fundamental test scenarios for model validation and contribute significantly to improving our understanding of complex fluid dynamics.

Three of the above-mentioned benchmark cases have been selected for this study. The turbulence models mentioned in Section 2.4 and the newly developed models have been compared in the following cases, namely the turbulent flat plate boundary layer flow, channel flow, and backward-facing step flow.

4.5.3.1.Turbulent Flat Plate Boundary Layer Flow

The turbulent flat plate scenario is a fundamental benchmark problem in CFD and turbulence modeling. This case is extensively employed to evaluate turbulence models because to its simplicity, comprehensible physics, and the availability of both experimental and theoretical data. The primary aim of this benchmark is to precisely forecast the evolution of the turbulent boundary layer over a flat plate in the absence of a pressure gradient.

The turbulent flat plate scenario entails simulating fluid flow, often air or water, over a planar surface. As the fluid traverses the plate, a boundary layer forms due to the no-slip condition at the wall, where the fluid velocity is zero relative to the plate. The flow within this boundary layer transforms from laminar to turbulent as it progresses downstream, resulting in a fully developed turbulent boundary layer.

The incoming flow generally exhibits a high Reynolds number, facilitating the transition of the boundary layer to turbulence following a brief laminar phase adjacent to the leading edge of the plate.

As the fluid traverses the plate, the boundary layer increases in thickness, and its velocity profile evolves from a linear configuration near the leading edge to a logarithmic profile as it progresses into turbulence.

The wall shear stress, which affects drag, markedly increases in the turbulent zone relative to the laminar region. Precisely forecasting wall shear stress is essential for the validation of turbulence models.

The Reynolds number is a critical parameter defined as $\mathrm{Re} = \frac{\mathrm{U}_\infty \mathrm{L}}{\nu}$, where U_∞ is the free-stream velocity, L is a characteristic length (e.g., distance from the leading edge), and ν is the kinematic viscosity. High Reynolds numbers (e.g., $Re > 10^5$) lead to a fully turbulent boundary layer.

Uniform velocity profile or a boundary layer profile can be specified. Typically, a pressure outlet condition is used to let the flow exit freely. A no-slip boundary condition is applied at the plate surface, with zero normal velocity and specified wall roughness if needed.

Precise simulation necessitates refined grids adjacent to the wall to accurately depict boundary layer intricacies. A high-resolution grid with enhanced cells in the streamwise and wall-normal orientations is advised. The precise modeling of the near-wall region is difficult because of strong velocity gradients. The appropriate selection of wall functions or low-Reynolds number models is essential.

No singular turbulence model excels universally; therefore, hybrid methodologies (such as Detached Eddy Simulation or LES/RANS integration) are frequently investigated.

This case also highlights the complexities of boundary layer flows, contributing significantly to the understanding and development of advanced turbulence models.

The schematic description of the turbulent flat plate boundary layer flow can be found below in the **Figure *4.20***.

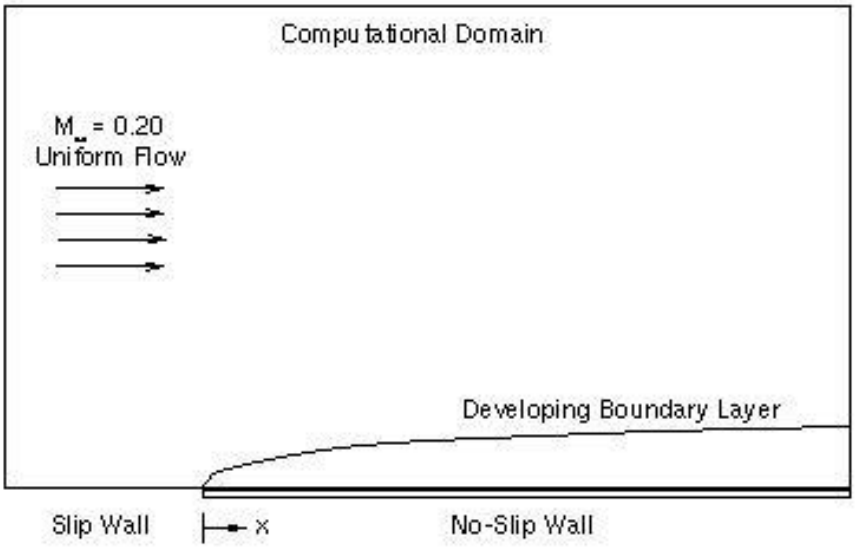

Figure 4.20. Flat plate boundary layer flow setup *(Wieghardt & Tillman, 1951)*.

The mesh-independent grid structure for the turbulent flat plate boundary layer flow case can be seen in **Figure 4.21**.

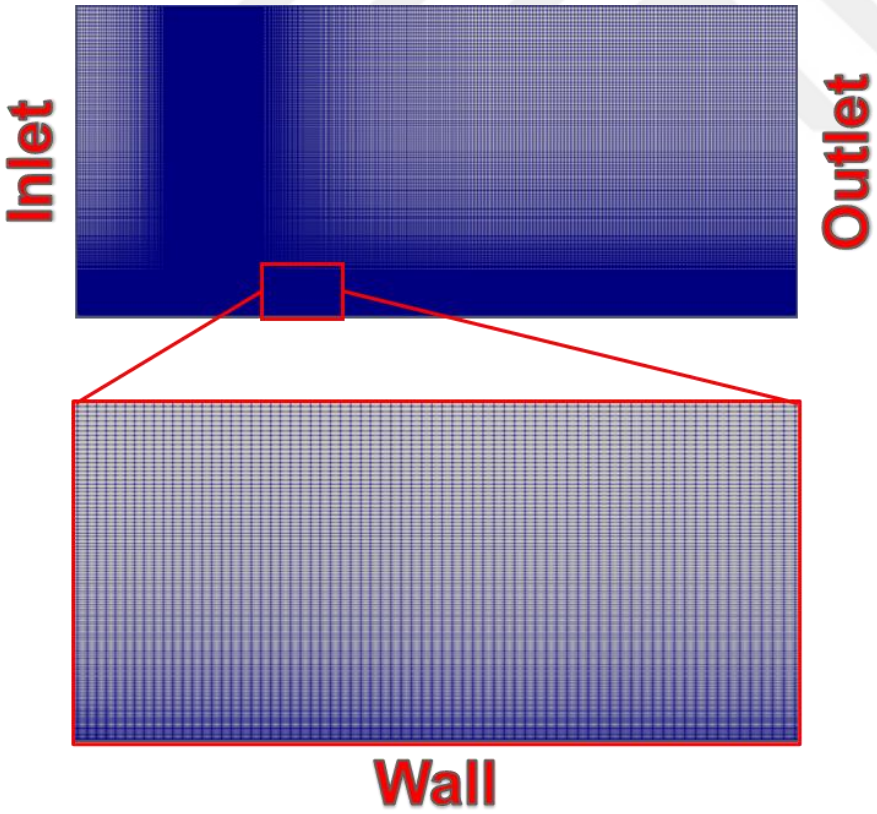

Figure 4.21. Selected grid structure of the turbulent flat plate boundary layer flow case.

Simulation results using various turbulence models have been presented below in different graphs such as in **Figure *4.22*** that compares various model results to experimental study of Wieghardt et al. (Wieghardt & Tillman, 1951) and Patel et al. (Patel et al., 1985).

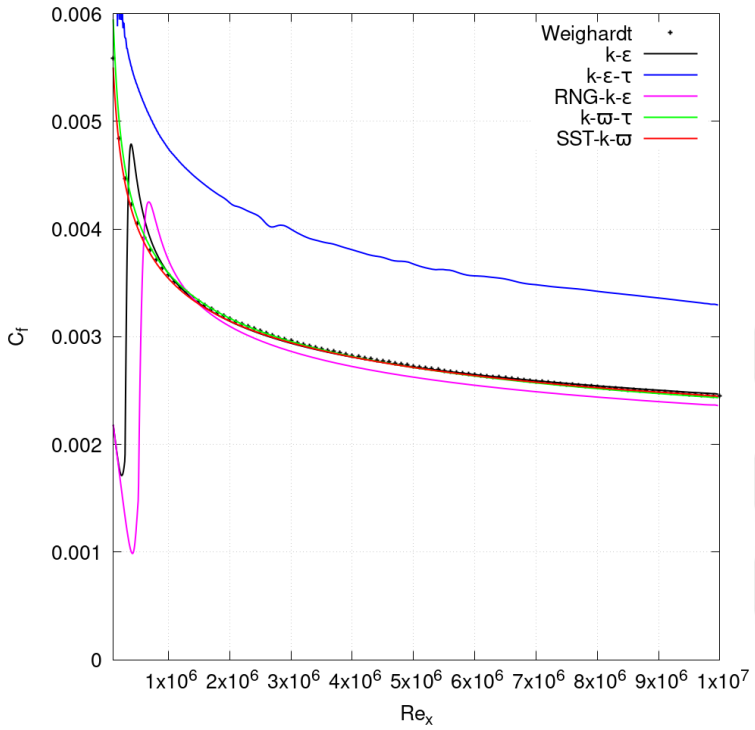

Figure 4.22. Comparison of skin friction coefficient vs Re_x.

The wall variables of u^+ and y^+ correlation has been presented in Figure 4.23. model data to both Spalding's Law and Weighardt et al. *(Wieghardt & Tillman, 1951)*.

k-ε model shows good agreement with the experimental data at higher Reynolds numbers but overpredicts C_f at lower Re_x. It diverges slightly from the experimental trend, indicating some inaccuracies, especially at lower Reynolds numbers. The *k-ε-τ* model consistently overestimates the skin friction coefficient throughout the whole spectrum of Reynolds numbers in comparison to experimental data and alternative models. This indicates that the model may be ill-suited for this flow pattern, particularly in forecasting C_f. The RNG *k-ε* model outperforms the traditional *k-ε* model at lower Reynolds numbers; however, it exhibits oscillating behavior, suggesting either numerical instability or sensitivity to initial conditions. It continues to correlate closely with the experimental findings at elevated Re_x values. *k-ω-τ* model provides one of the best fits to the

experimental data, closely following the trend of C_f across all Reynolds numbers. It suggests a reliable prediction of boundary layer behavior and is quantitatively one of the most accurate among the models shown. The *SST k-ω* model exhibits strong concordance with experimental data and other high-performing models, including the *k-ω-τ*. It demonstrates commendable precision across the spectrum of Reynolds values and does not display notable variations or oscillations.

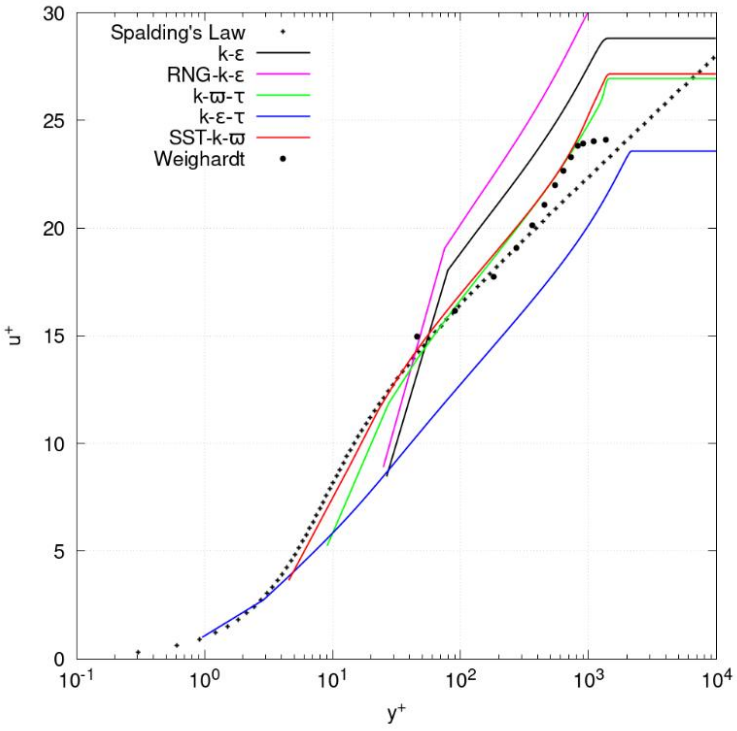

Figure 4.23. Comparison of the dimensionless variables u^+ and y^+.

Figure 4.23 compares the non-dimensional velocity profile (u^+) against the non-dimensional wall distance (y^+) for several turbulence models and experimental data (Weighardt).

k-ε matches the Spalding's Law and experimental data well in the buffer layer but deviates slightly in the log-law region at higher y^+, showing a slight overprediction. RNG *k-ε* shows significant deviation, especially at higher y^+ indicating an overprediction of velocity, which suggests a less accurate performance in this region. *k−ω−τ* model provides a reasonable match with Spalding's Law and the experimental data, performing well in both the viscous sublayer and the log region. *k−ε−τ* underpredicts the velocity in the log region, showing lower accuracy compared to other models. *SST k−ω* closely

follows Spalding's Law and Weighardt data, making it one of the most accurate models, especially in the near-wall region.

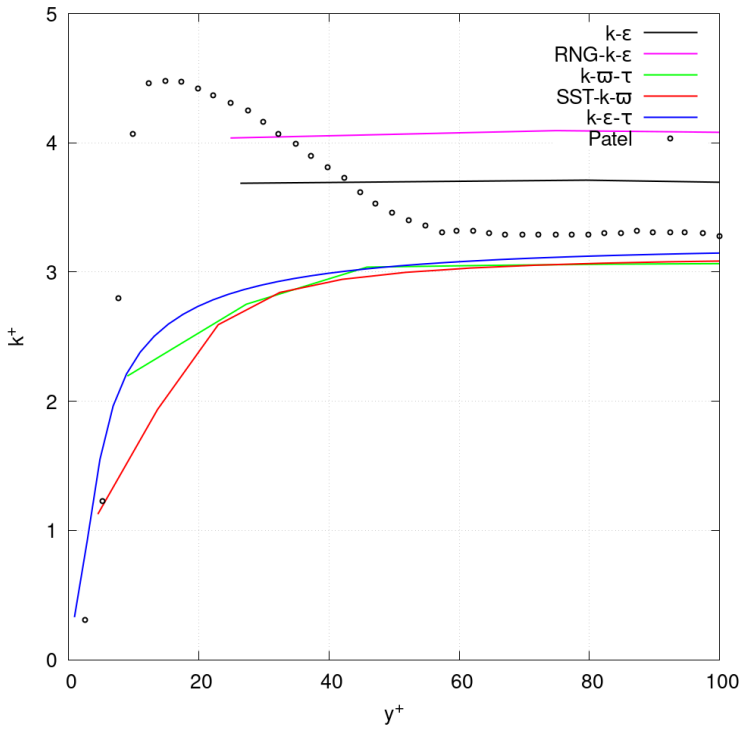

Figure 4.24. Comparison of the wall-normalized TKE vs. y^+.

As can be seen from **Figure 4.24**, *k-ε* shows a nearly constant prediction of k^+, significantly overpredicting values compared to the experimental data and deviating from expected physical behavior. RNG *k-ε* overpredicts k^+ throughout, showing poor alignment with experimental data, indicating an aggressive prediction of turbulent kinetic energy. $k-\omega-\tau$ and *SST-k−ω* models closely follow the experimental data in the near-wall region and remain within acceptable bounds throughout, with *SST-k−ω* showing slightly better performance. $k-\varepsilon-\tau$ **s**hows a better alignment in the near-wall region but still overpredicts slightly compared to the most accurate models.

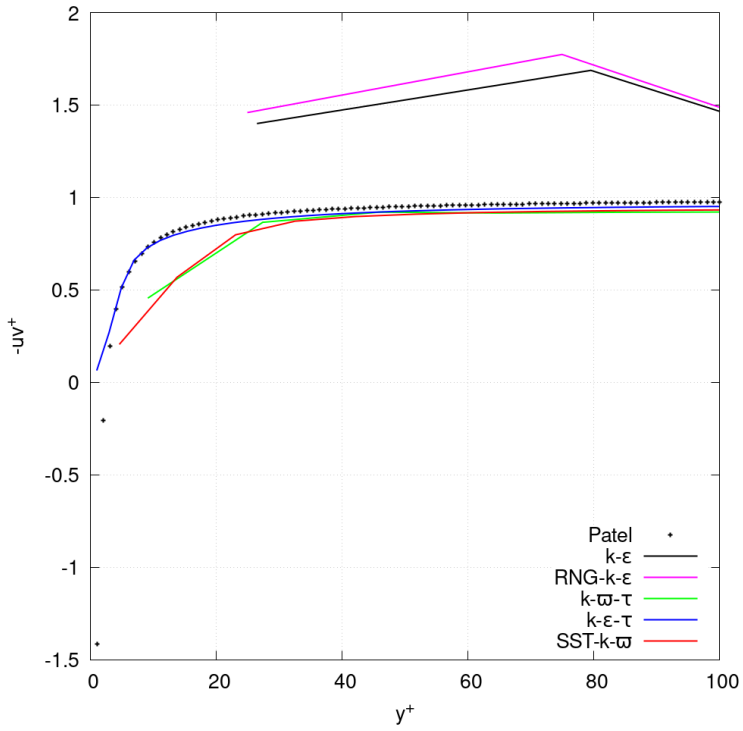

Figure 4.25. Comparison of the wall-normalized shear stress u^+ and y^+.

Figure 4.25 shows that *k-ε* predicts a nearly constant value for $-u'v'^+$, which aligns poorly with experimental data, suggesting a simplistic representation of turbulence structures. RNG *k-ε* overpredicts the stress values and does not match well with the experimental trend, showing significant deviation. *k−ω−τ* and *SST-k−ω* provide good alignment with experimental data near the wall and taper off correctly with increasing y^+ indicating reliable performance in predicting turbulent stresses. *k−ε−τ* shows reasonable prediction closer to the experimental trend but slightly underpredicts near the wall compared to the *SST-k−ω*.

Furthermore, *k-ω-τ* converges faster compared to SST *k-ω*, using the same computational platform and same conditions. The actual numbers can be found in **Table 4.6**. The configuration of the workstation is as follows: Xeon W-2245 (8-core) CPU, 64 GB of DDR4 (2666 MHz) RAM, and nVIDIA Quadro P5000 GPU.

Table 4.6. Comparison of SST *k-ω* and *k-ω-τ* in terms of convergence and time

	SST *k-ω*	*k-ω-τ*
Iterations	2044	1131
Clock Time	2040s	1539s

4.5.3.2.Channel Flow

Channel flow benchmark cases serve as crucial validation tools for CFD simulations, particularly in studying wall-bounded turbulent flows. The channel flow configuration consists of fluid flowing between two parallel plates. This setup represents a simplified yet fundamental representation of flow in numerous engineering systems, including pipelines, heat exchangers, and microfluidic devices.

One of the most well-known channel flow benchmark cases is the DNS of a turbulent channel flow by Kim, Moin, and Moser (KMM) (J. Kim et al., 1987). This landmark study provided extensive data on the statistics of turbulent channel flow, including mean velocity profiles, Reynolds stresses, and turbulent kinetic energy spectra, which are essential for validating turbulence models.

The channel flow benchmark case typically involves simulating turbulent flow in a channel of specified dimensions and boundary conditions. The Reynolds number, defined as the ratio of inertial forces to viscous forces, is a key parameter in characterizing the flow regime. In channel flow benchmark cases, the Reynolds number is typically defined based on the channel width and the bulk velocity of the flow.

The mesh-independent grid structure for the channel flow case can be seen in **Figure 4.26**.

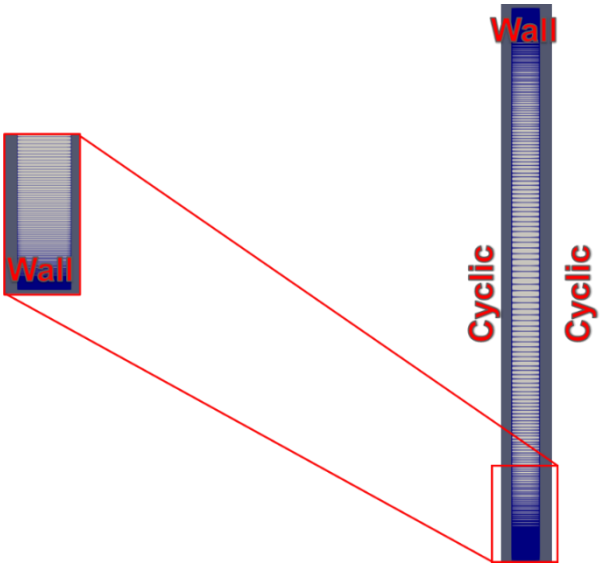

Figure 4.26. Selected grid structure of the channel flow case.

Channel flow results can be found in the **Figure 4.27** comparing many widely used turbulence models in the literature including k-ε-τ model to DNS data of Kim et al. (J. Kim et al., 1987). Normalized velocity graph shows that almost all the models can predict the behavior of the flow fairly or closely. However, by looking at wall velocity and dimensionless distance graph, it can be stated that k-ε family fall short in predicting the near-wall region flow trends. R-ε-τ model outperforms all other models in terms of estimating turbulent kinetic energy. However, it still underpredicts the near-wall turbulent kinetic energy profile.

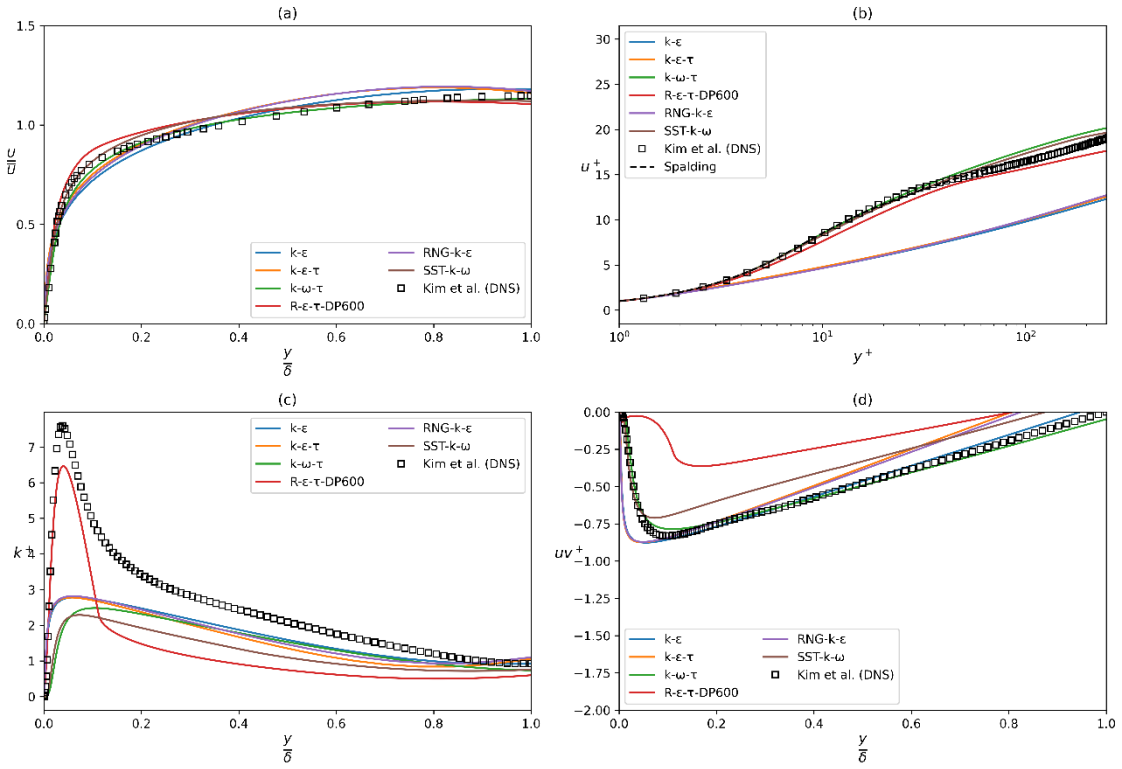

Figure 4.27. (a) Normalized velocity vs normalized wall distance, (b) Comparison of the dimensionless variables u^+ and y^+, (c) Wall turbulent kinetic energy vs normalized wall distance, (d) Wall shear stress vs normalized wall distance for channel flow case.

Results of the optimized coefficients for the k-ω-τ model can found in the figure below.

According to the optimization study, the goals have been reached since, objective function was set to minimize the errors of velocity profiles mostly and then the shear stress profiles.

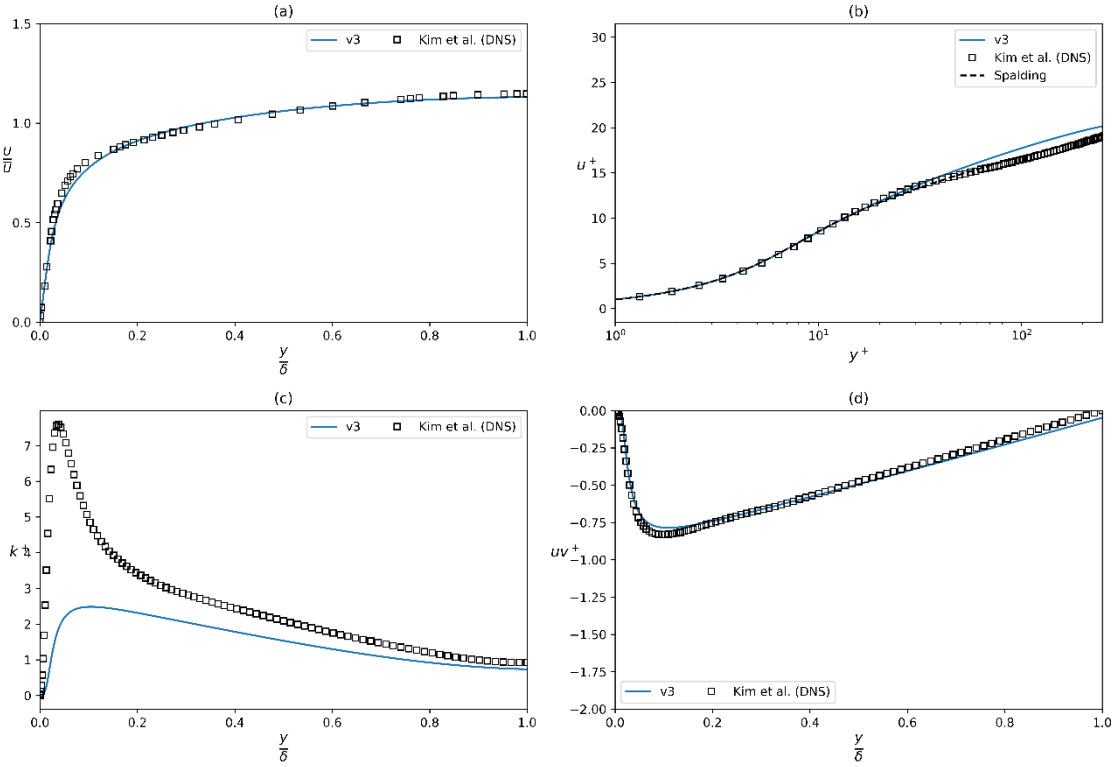

Figure 4.28. Results of the optimized version of *k*-*ω*-*τ* (a) Normalized velocity vs normalized wall distance, (b) Comparison of the dimensionless variables u^+ and y^+, (c) Wall turbulent kinetic energy vs normalized wall distance, (d) Wall shear stress vs normalized wall distance for channel flow case.

The Reynolds-Stress Model that has been studied here needs to optimized, and it can be seen from one of the results of the grid study which was performed by using five input parameters that means five coefficients have been used in the optimization process. Nevertheless, the study has to be extended or the model parameters have to be adjusted to produce acceptable results.

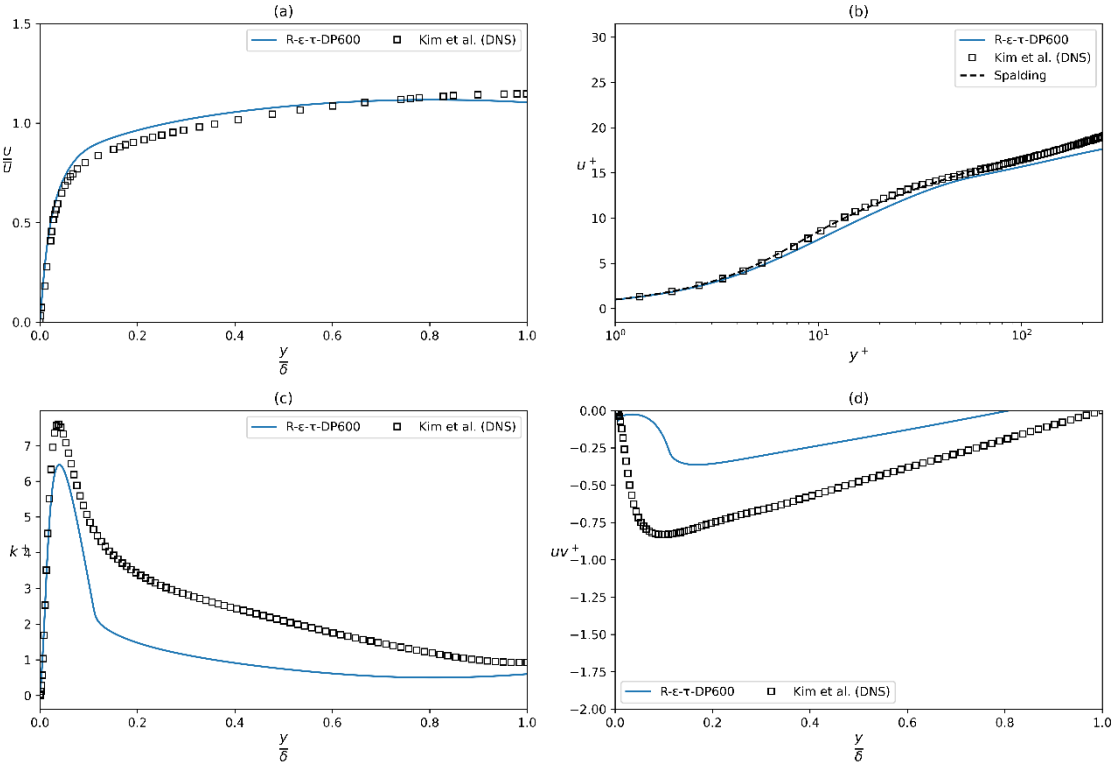

Figure 4.29. One of the grid study results of the of R-ε-τ RSM model (a) Normalized velocity vs normalized wall distance, (b) Comparison of the dimensionless variables u^+ and y^+, (c) Wall turbulent kinetic energy vs normalized wall distance, (d) Wall shear stress vs normalized wall distance for channel flow case

4.5.3.3.Backward-Facing Step Flow

The BFS is a widely used and well-known benchmark example in the fields of turbulence modeling and CFD. It is commonly employed to investigate separated flows, reattachment phenomena, and the behavior of turbulence. It offers vital information about how turbulence models perform in complex flow situations, such as abrupt expansion and reattachment.

The BFS case exhibits an abrupt enlargement in a conduit, where the fluid confronts a vertical change in the height (h) of the bottom wall. The step induces the detachment of the boundary layer, resulting in the formation of a recirculation zone located downstream of the step. The height of the upstream channel prior to the step is typically H, frequently twice the height of the step (2h). The height of the downstream channel is then increased to H + h (L. Chen et al., 2018).

Reattachment and recovery of the flow take place in the downstream channel, where the flow continues through a fully developed inlet velocity profile that is typically specified.

Key flow characteristics of the case can be explained as follows. Upon encountering the step, the flow undergoes separation, resulting in the formation of a recirculation zone directly downstream. The flow reattaches at a specific distance from the step, creating a reattachment point that is distinguished by intricate interactions among turbulent structures.

A shear layer arises at the interface between the detached flow in the recirculation area and the primary flow above it. The shear layer plays a crucial role in the formation of turbulence and must be appropriately represented in simulations.

The precise location at which the separated flow reattaches to the wall is a crucial element for the validation of turbulence models. The reattachment length, x_r, is highly influenced by the turbulence model employed and is frequently utilized as a standard metric for comparison.

Downstream of the reattachment point, the flow slowly recovers and redevelops into a fully turbulent boundary layer.

Boundary Conditions:

- Inlet: The inlet condition is typically a fully developed turbulent velocity profile, with a specified Reynolds number based on step height and inlet velocity.
- Outlet: A pressure outlet or a Neumann boundary condition with zero gradients is usually applied at the downstream exit.
- Walls: The top and bottom walls (including the step surface) are no-slip walls, which means zero velocity at the wall surfaces.

The low entities are recorded at multiple stations located downstream of the step to document the progression of the recirculation zone and the reattachment of the boundary layer. Derived from flow visualization or velocity measurements, identifying the precise location when the split shear layer reattaches to the bottom wall is an expected result to be found out and compared. It provides details regarding the forces exerted on the walls

and assist in verifying the accuracy of the pressure field and turbulent stresses projected by the model.

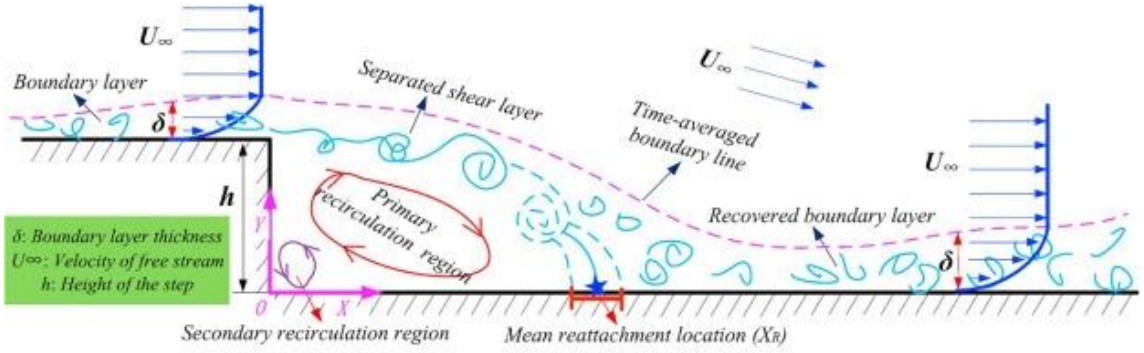

Figure 4.30. Schematic description of a backward-facing step (L. Chen et al., 2018).

The benchmark case, on which Driver and Seegmiller published an experimental work (Driver & Seegmiller, 1985), has been replicated to be simulated using OpenFOAM v2112 with different turbulence models. Figures below show the velocity profiles, and wall-normalized turbulence parameters.

The mesh-independent grid structure for the backward-facing step case can be seen in **Figure 4.31**.

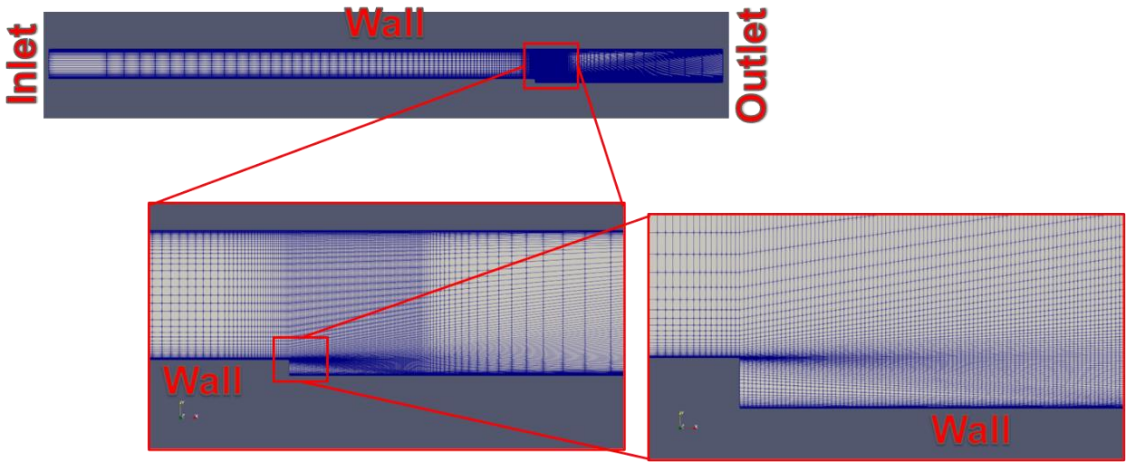

Figure 4.31. Selected grid structure of the Backward-Facing Step case.

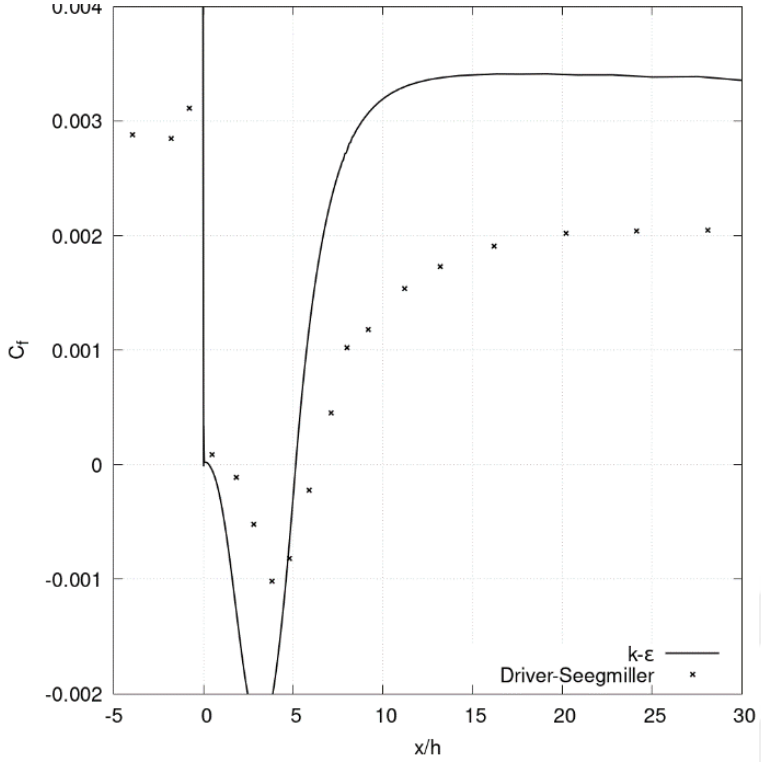

Figure 4.32. Skin friction coefficient at the lower wall (k-ε).

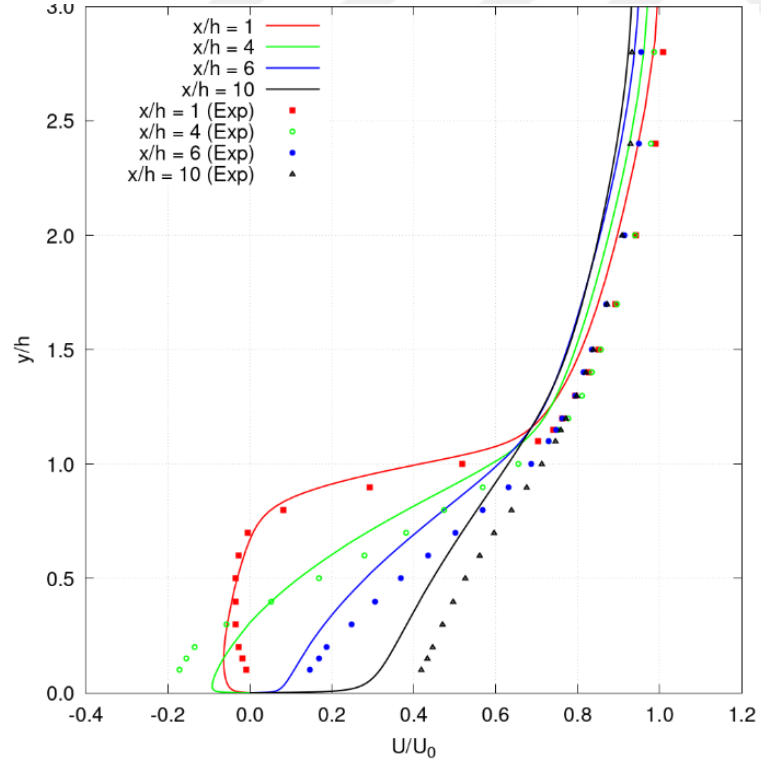

Figure 4.33. Normalized velocity profiles at various locations after the step (k-ε).

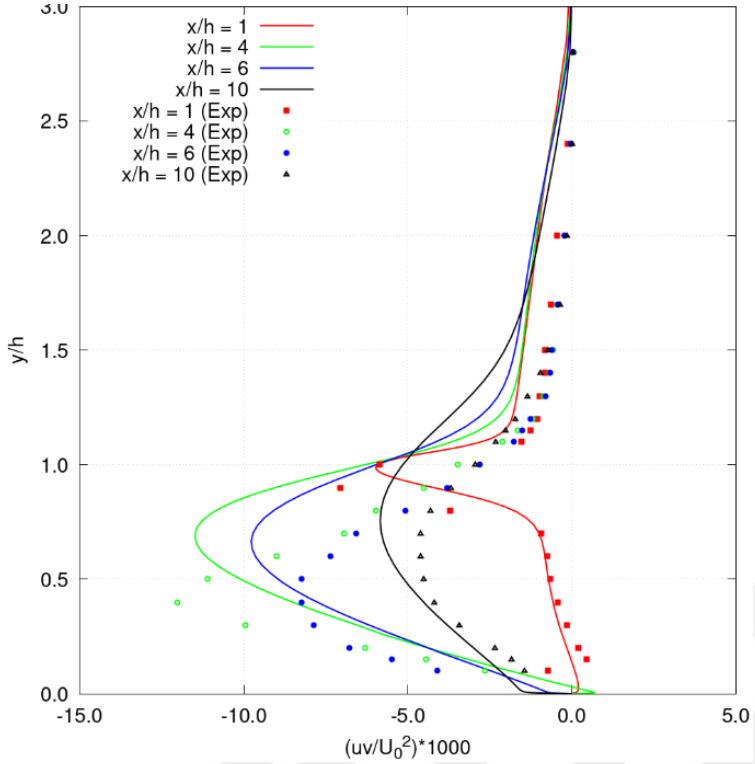

Figure 4.34. Normalized shear stress profiles at various locations after the step (k-ε).

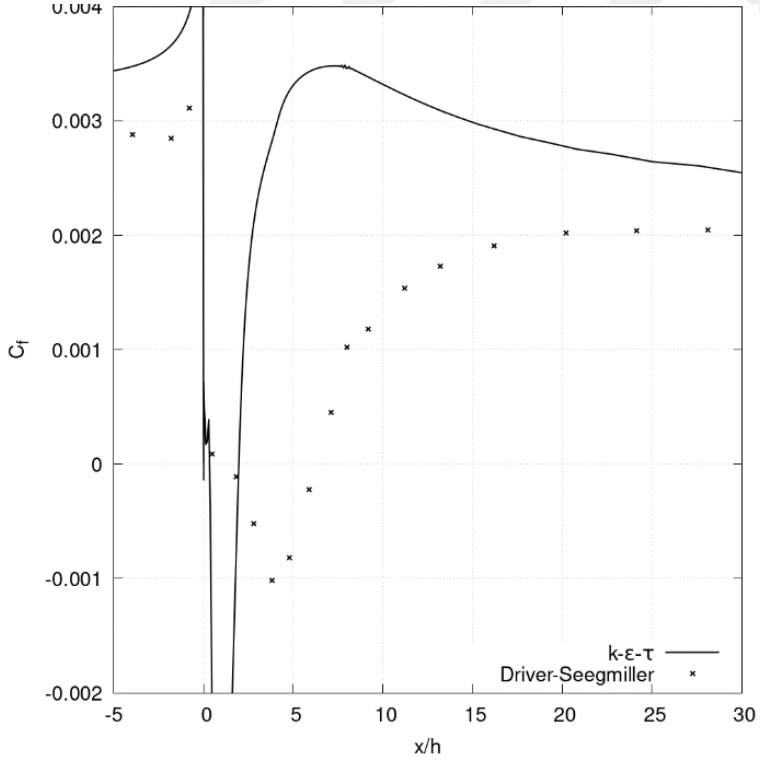

Figure 4.35. Normalized velocity profiles at various locations after the step (k-ε-τ).

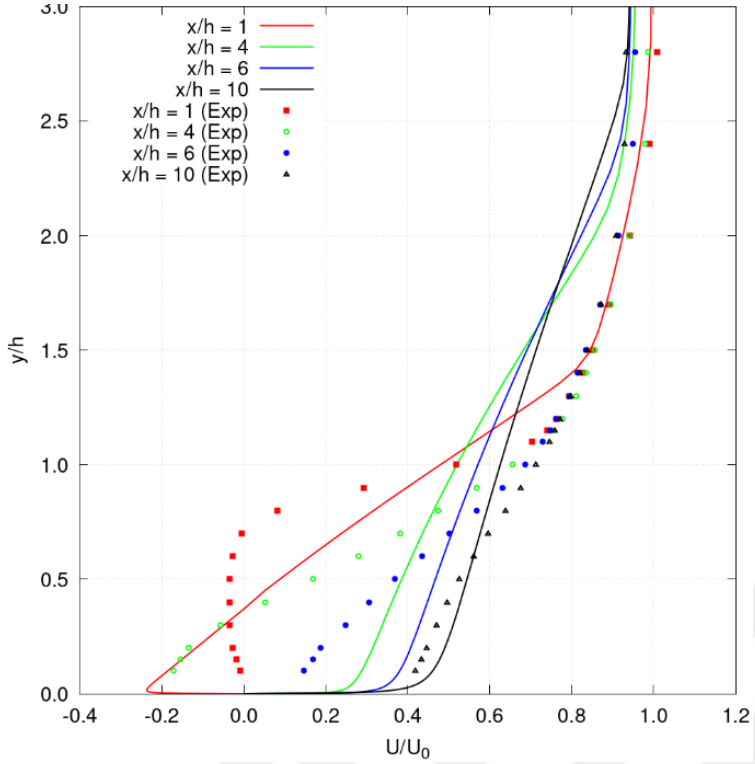

Figure 4.36. Normalized shear stress profiles at various locations after the step (k-ε-τ).

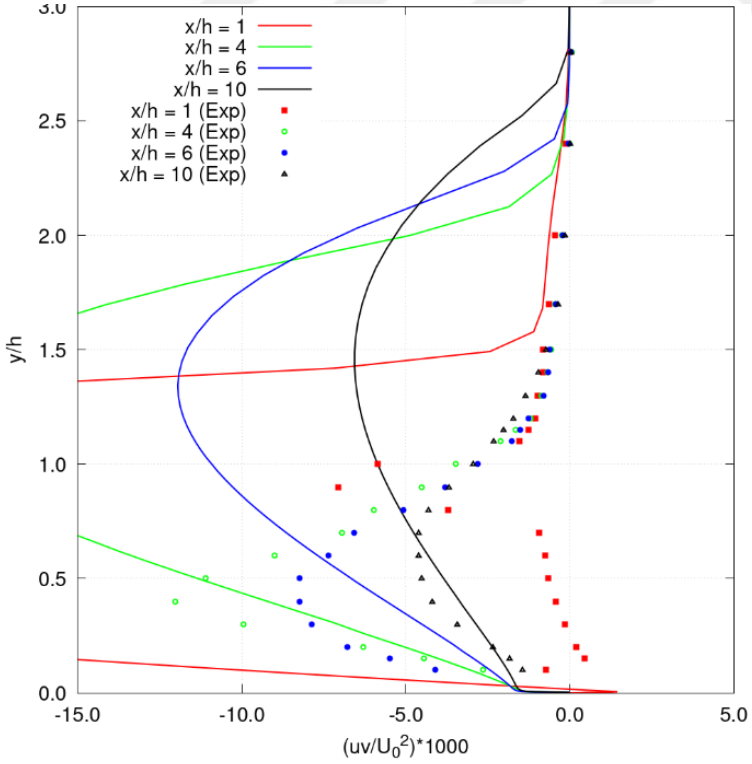

Figure 4.37. Skin friction coefficient at the lower wall (k-ε-τ).

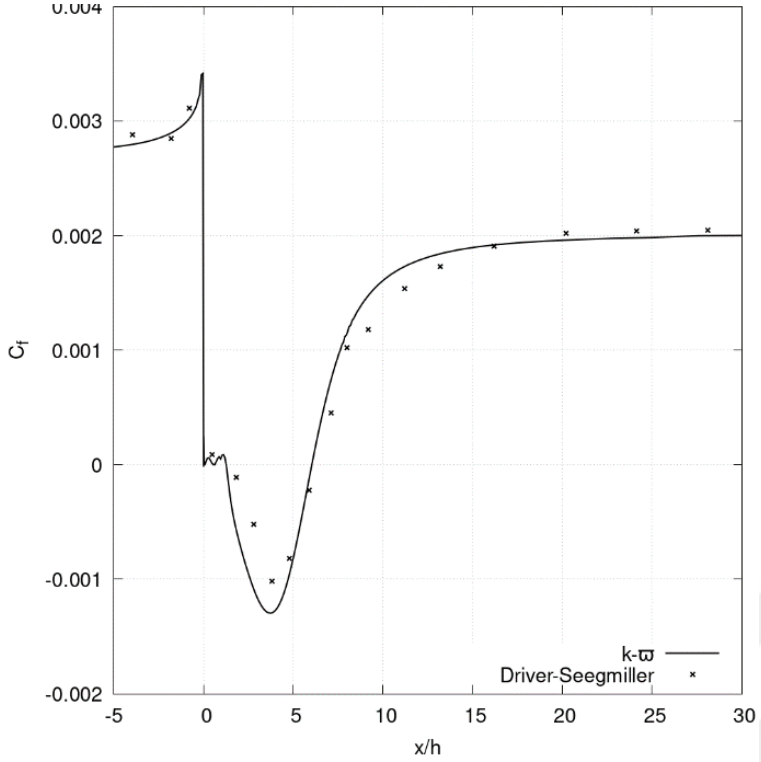

Figure 4.38. Normalized velocity profiles at various locations after the step (k-ω).

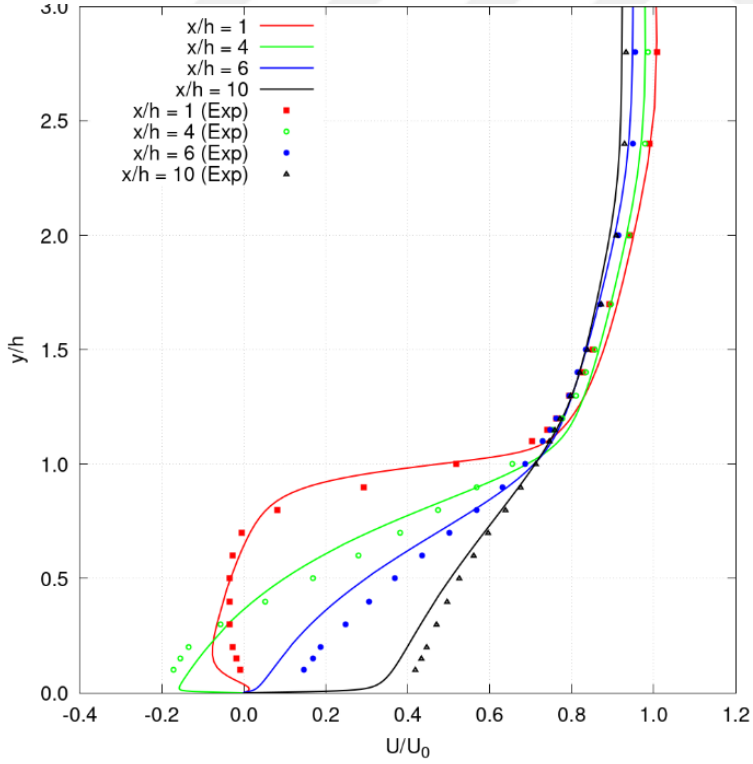

Figure 4.39. Normalized shear stress profiles at various locations after the step (k-ω).

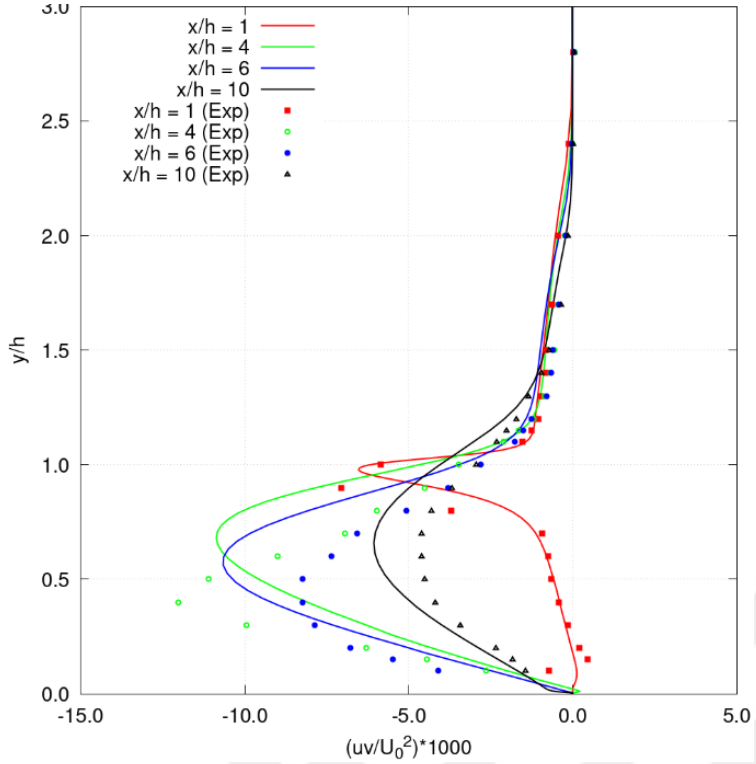

Figure 4.40. Skin friction coefficient at the lower wall (k-ω).

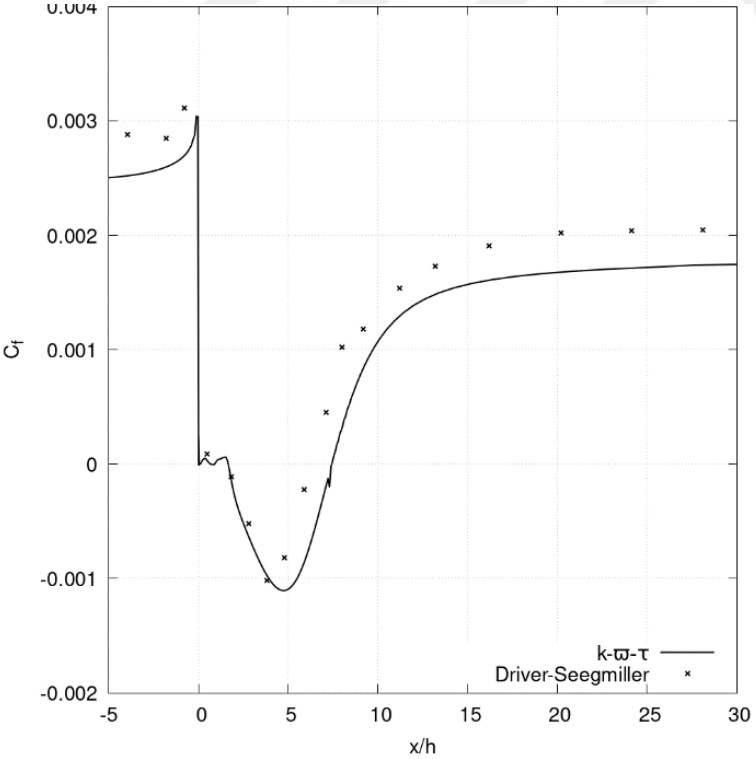

Figure 4.41. Normalized velocity profiles at various locations after the step (k-ω-τ).

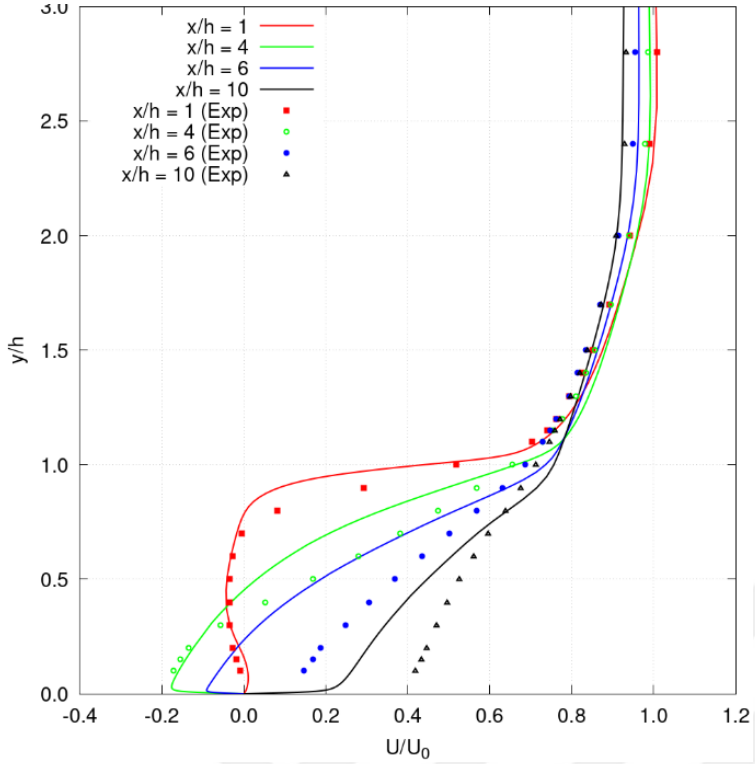

Figure 4.42. Normalized shear stress profiles at various locations after the step (k-ω-τ).

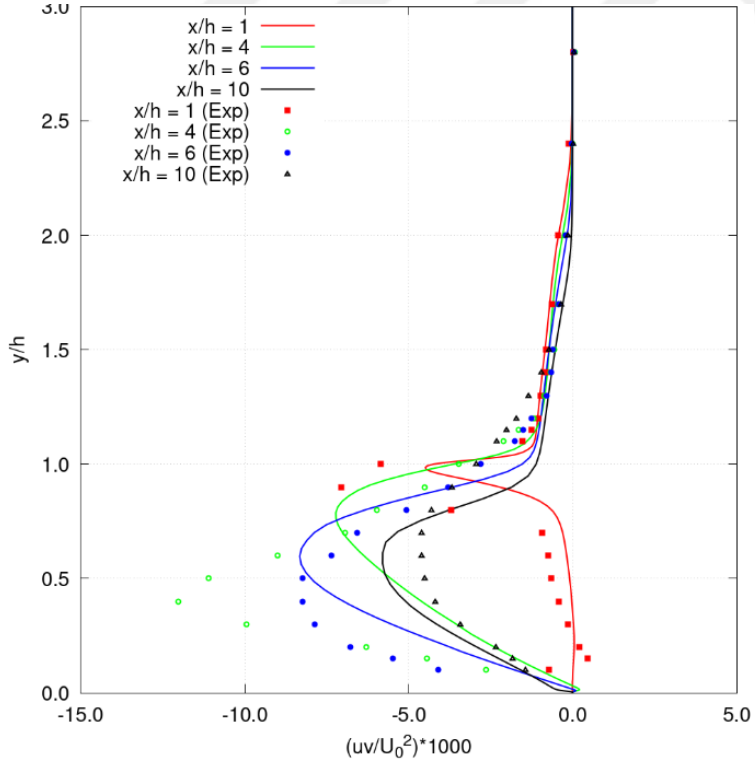

Figure 4.43. Skin friction coefficient at the lower wall (k-ω-τ).

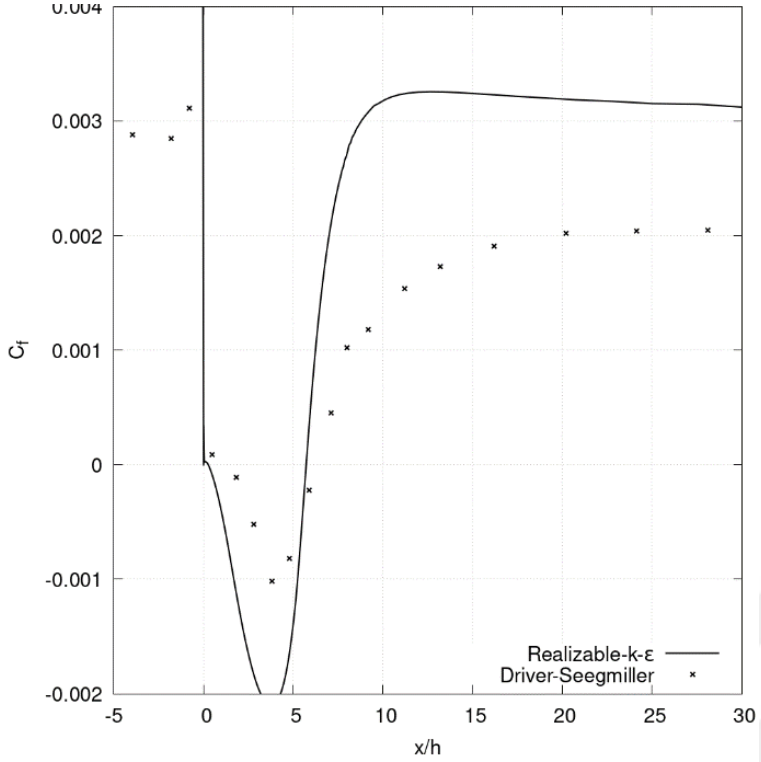

Figure 4.44. Normalized velocity profiles at various locations after the step (Real.-k-ε).

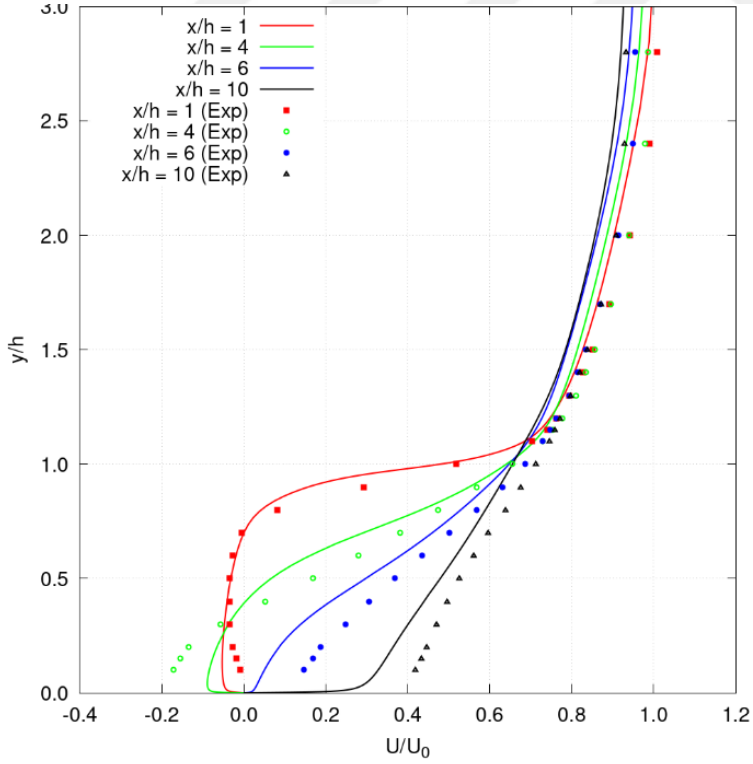

Figure 4.45. Normalized shear stress profiles at various locations after the step (Real.-k-ε).

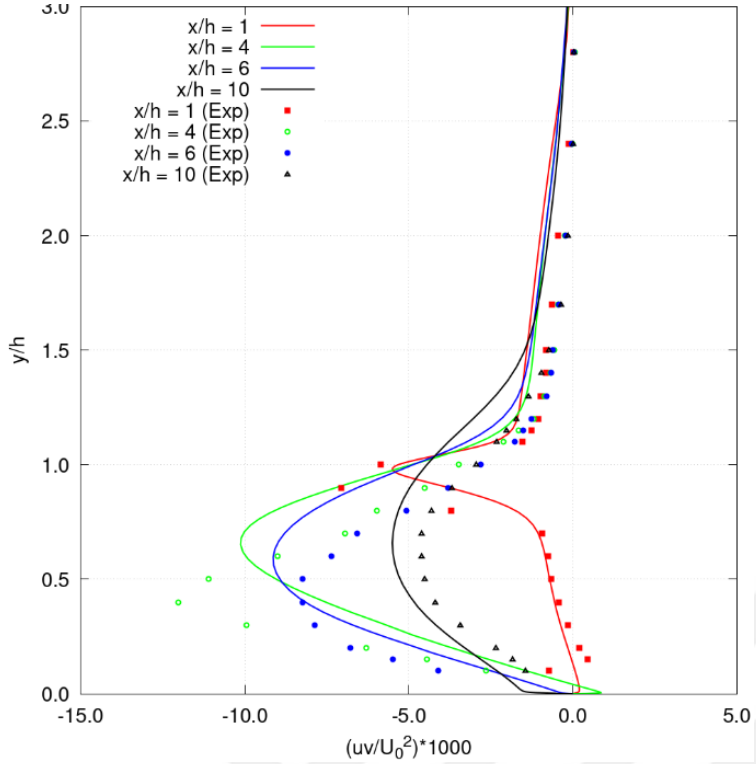

Figure 4.46. Skin friction coefficient at the lower wall (Real.-k-ε).

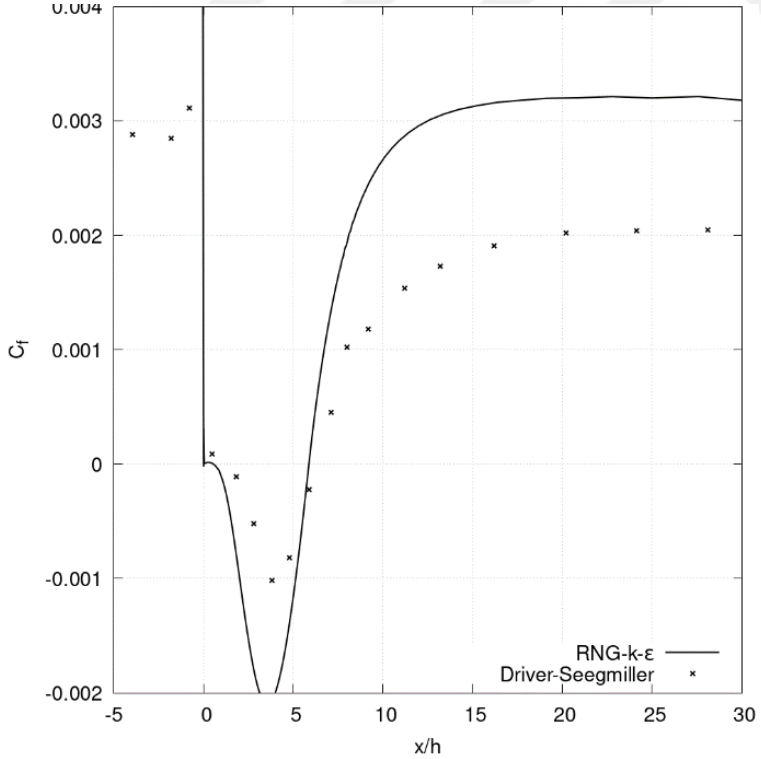

Figure 4.47. Normalized velocity profiles at various locations after the step (RNG-k-ε).

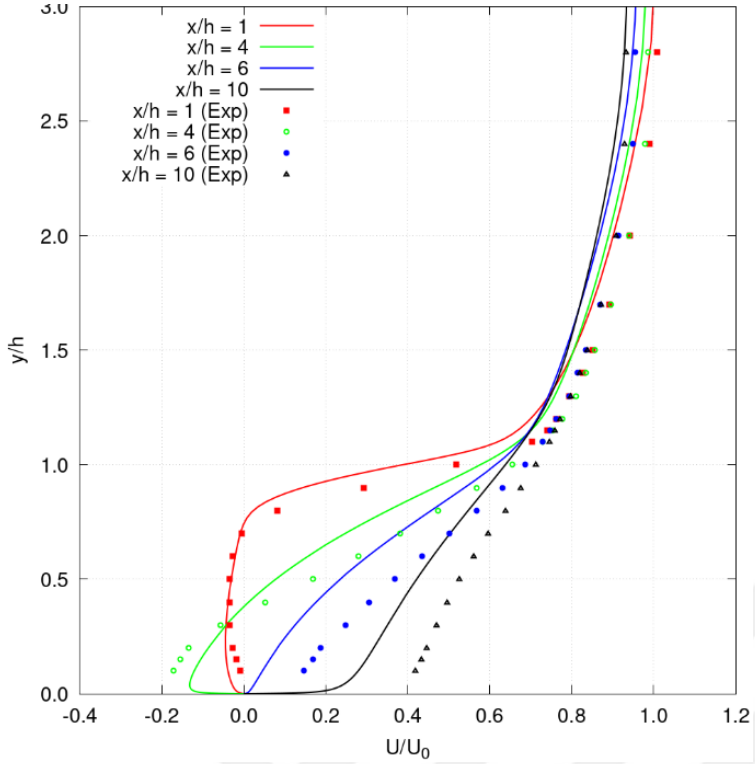

Figure 4.48. Normalized shear stress profiles at various locations after the step (RNG-k-ε).

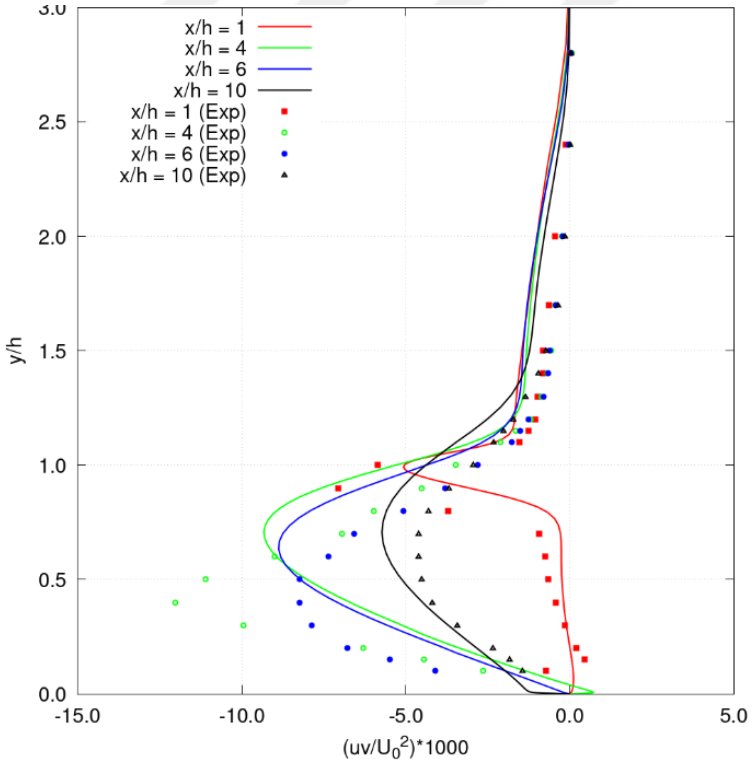

Figure 4.49. Skin friction coefficient at the lower wall (RNG-k-ε).

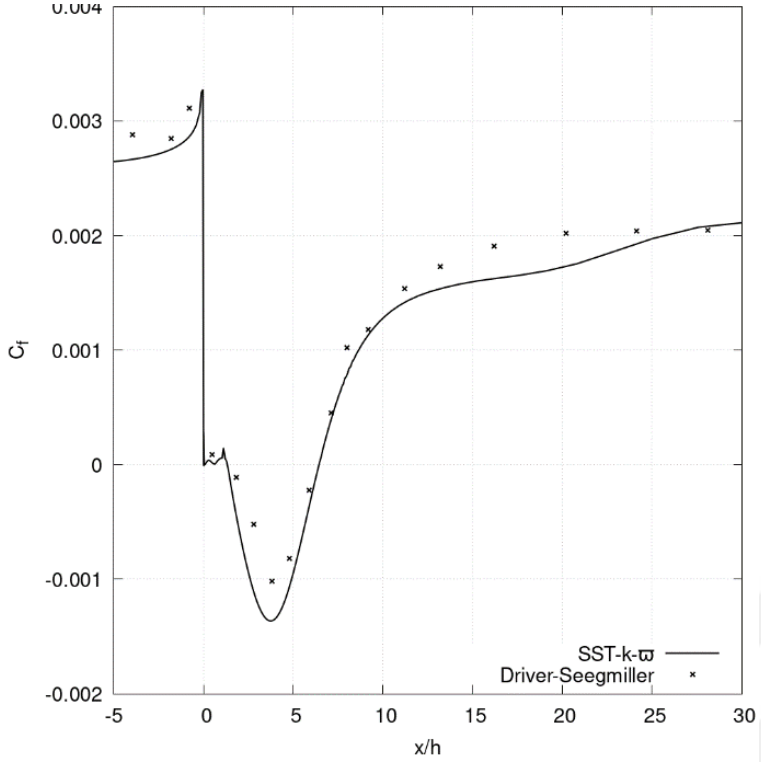

Figure 4.50. Normalized velocity profiles at various locations after the step (SST-k-ω).

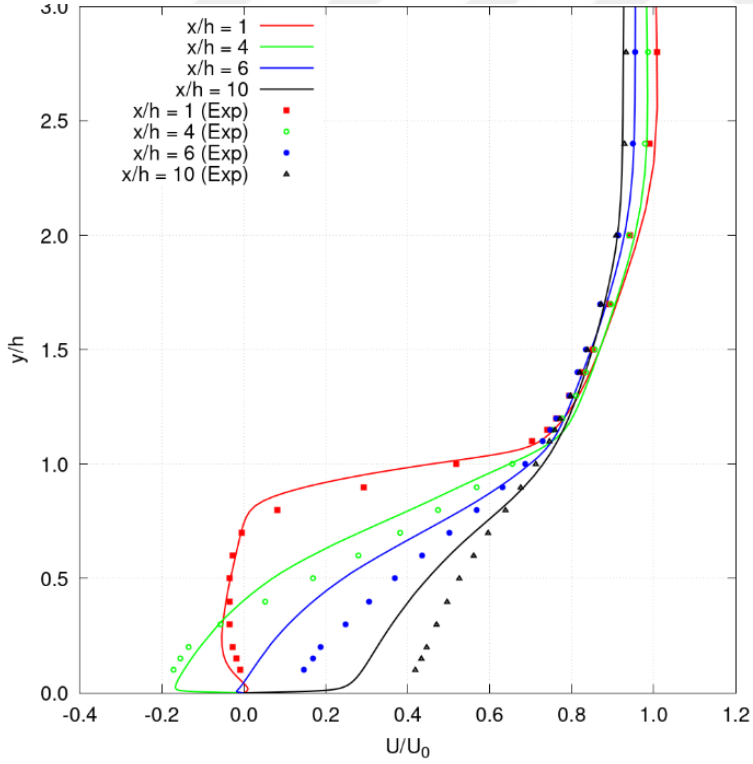

Figure 4.51. Normalized shear stress profiles at various locations after the step (SST-k-ω).

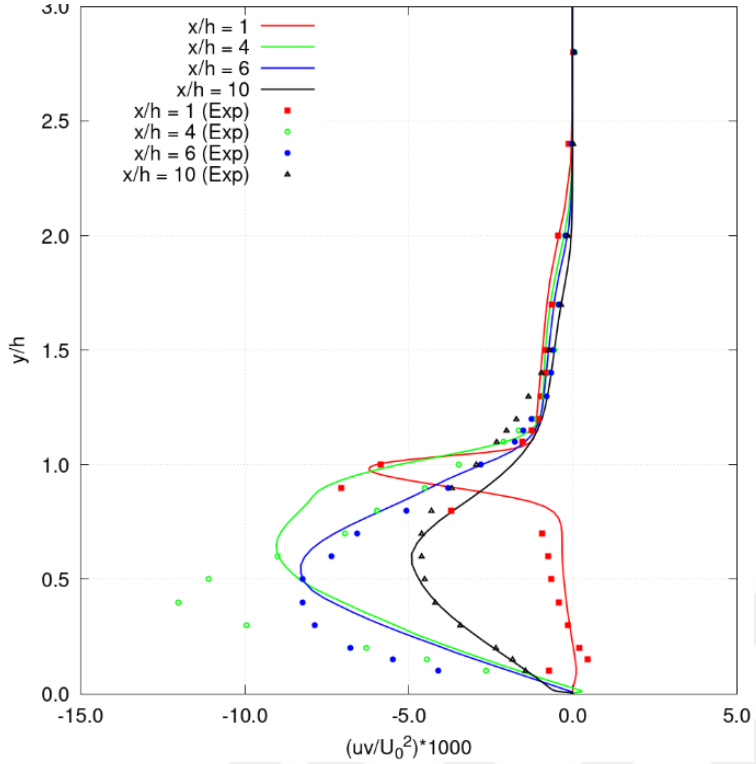

Figure 4.52. Skin friction coefficient at the lower wall (SST-k-ω).

As it is expected, the models incorporating ω, showed better results compared to the turbulence models which are *k*-*ε* derivatives. *k*-*ω*-*τ* on the other hand showed promising results as its coefficients were optimized for channel flow.

Figures above also compare various turbulence models to the Driver-Seegmiller experimental data based on skin friction coefficient C_f versus the normalized position (x/h):

The *k*-*ε* model shows significant deviation from the experimental data near the separation point (around ($x/h = 0$). It predicts a much larger separation bubble with a deeper negative C_f compared to the experimental data. After the reattachment point, the *k*-*ε* model overpredicts C_f and does not capture the recovery trend accurately. The *k*-*ε*-τ model provides a similar trend to the *k*-*ε* model, but it better captures the separation bubble and the reattachment point. However, it still overpredicts C_f after the reattachment and fails to match the gradual recovery trend shown by the experimental data. The *k*-*ω* model captures the separation and reattachment points more accurately compared to the *k*-*ε* based models. It follows the experimental data closely in the separation region but slightly

underpredicts C_f in the recovery phase. This model shows better overall performance in predicting the C_f distribution. The k-ω-τ model demonstrates an excellent match with the experimental data in the separation and reattachment regions. It captures the post-reattachment behavior well and provides a good quantitative match in the recovery phase, making it one of the better models in this comparison. The Realizable k-ε model shows improved behavior over the standard k-ε, particularly in capturing the reattachment point. However, it still exhibits issues in accurately predicting the C_f values in the separation bubble, showing a deeper negative C_f than observed experimentally. The RNG k-ε model performs similarly to the standard k-ε but provides a slightly better prediction of the reattachment point. It shows less overshoot in C_f after reattachment but still deviates significantly in the separation bubble. The SST k-ω model provides closer match to the experimental data among all models. It accurately predicts both the separation and reattachment points and follows the trend of C_f closely in the recovery phase. This model's performance indicates strong predictive capabilities for adverse pressure gradient and separation flows.

In short, the SST k-ω and k-ω-τ models show the best agreement with the experimental data, accurately capturing the critical points of separation and reattachment. k-ε based models generally struggle with accurately predicting the separation bubble and show significant deviations in C_f values. The Realizable k-ε and RNG k-ε models offer slight improvements but still lag behind the ω-based models.

5. CONCLUSIONS

In this study, a novel two-time scale, three-equation turbulence model (k-ω-τ) was developed based on the limitations of WFC model for predicting the behaviour of shear flows, and its performance was then presented for an axisymmetric jet, plane asymptotic wake and plane jet. The starting point was the modification and correction of k-ε-τ model for the better prediction of turbulence entities in free shear flows. Second stage involved forming k-ω-τ model, its implementation, followed by using the data collected from the grid study to calibrate the selected model coefficients using Bayesian Optimization technique. The last stage was to integrate the two-time scale approach in an RSM methodology. Calibration study yielded better only for the case used for training purposes which is the channel flow case. On the other hand, k-ω-τ model has not failed in such occasion. Its only disadvantage was its being an isotropic model which hinders its ability to capture directional variations in turbulence quantities.

The preliminary findings indicate that the k-ε-τ model outperforms the k-ε model by a significant margin. The first benefit is that the "plane jet/round jet" anomaly is better resolved by avoiding additional difficulties of second moment closures. The second benefit is that the flow behaviour is better predicted than with the two-equation models in the wake that is characterised by its weak shear form. Furthermore, it was discovered that:

- Consistent with the measurements, the three-equation model (utilizing identical parameters across all three cases) estimates a spread rate of 0.109 for the plane jet;

- Estimates the round jet spreading rate of 0.089, which is over 23% better than the k-ε, and *SST* k-ω models and consistent with the experimental data;

- The parameter for spreading of the plane wake is estimated to be 0.081, which is approximately 6% more accurate than the k-ε model and 4% more accurate than the *SST* k-ω model;

- Time-scales τ and $\frac{k}{\varepsilon}$ behave quite similar to each other in most part of the jet as expected (in non-equilibrium situations as in the compression stroke of an IC engine, these two will differ considerably).

Considering the studies carried out for optimizing *k-ω-τ* model for the channel flow was a success since, at least the results of the two other benchmark cases are also promising. The optimization study yielded 0.14 RMSE score which is quite satisfactory since, because of the nature of the model, it cannot resolve wall normalized turbulent kinetic energy, and the error could be due to that entity. The calibrated version of the *k-ω-τ* model contains the following coefficients and their values: $\gamma = 0.55$, $C_{\tau 0} = 1.286$, $C_{\tau 1} = 0.592$, $C_{\tau 2} = 0.625$.

RSM model studies also proved to be a better option concerning the mentioned issues above. Wall normalized turbulent kinetic energy was proven to be better resolved compared to other isotropic models considered in the context of this study. The peak value of k^+ where the gradients are quite high estimated with an acceptable error using a certain combination of the coefficients: $C_{\varepsilon 1} = 0.375$, $C_{\varepsilon 2} = 2.0$, $C_{\tau 0} = 2.0$, $C_{\tau 1} = 0.5$, $C_{\tau 2} = 0.25$.

Considering other aspects such as the computational costs and convergence, *k-ω-τ* outperforms SST *k-ω* by almost 24.6% in terms of clock time as it converges faster and uses less CPU in the case of turbulent flat plate boundary layer flow.

6. FUTURE WORK

The models introduced in this thesis mark a notable progress in the field of CFD. However, there are still several possibilities for further research and improvement. Possible future directions to improve the capabilities and relevance of the models have been presented below.

The current implementations mainly concentrate on basic geometry or idealized flow patterns. Expanding the models to accommodate intricate geometries found in real-world engineering applications would greatly enhance its usefulness and applicability. Developing better mesh generation techniques and numerical algorithms may be necessary for this expansion to accurately represent the flow mechanics in complex geometries.

While the developed models demonstrate improved predictive accuracy compared to traditional isotropic models, further enhancements could be achieved by incorporating advanced turbulence modeling approaches. For example, hybrid RANS-LES models or scale-resolving simulations (such as DES or SAS) could be explored to capture a wider range of turbulence scales and improve the fidelity of predictions, particularly in regions of flow separation, transition, or highly turbulent flows.

It is crucial to continuously validate and compare the models with experimental data and high-fidelity simulations to evaluate their performance under various flow conditions and geometries. Collaborating with experimentalists and researchers in relevant domains will help obtain high-quality data for validation and assure the models' reliability and robustness under different operating settings.

Integrating the models into machine learning frameworks would enable engineers to leverage their capabilities for many design and analysis tasks. Coupling the models with optimization algorithms or multidisciplinary optimization techniques could facilitate the automated design of various shapes with improved performance characteristics, such as reduced drag, enhanced lift, or better flow control.

The application of the models to novel flow regimes or engineering problems that have not been extensively studied represents an exciting area for future exploration. Examples include supersonic and hypersonic flows, flows with significant heat transfer or chemical reactions, and flows involving complex fluid-structure interactions or multiphase phenomena. Investigating these challenging scenarios would further validate the models' predictive capabilities and uncover new insights into the behavior of turbulent flows in practical applications.

In conclusion, the development of the models presented in this thesis lays the foundation for future advancements in computational fluid dynamics and engineering simulation. By addressing the aforementioned research directions and collaborating with experts across interdisciplinary fields, the models can continue to evolve and contribute to the ongoing quest for accurate, efficient, and reliable tools for predicting and understanding turbulent flows in engineering applications.

REFERENCES

Almohammadi, K. M. (2020). Assessment of Reattachment Length Using Turbulence Models on Backward Facing Step (BFS) for Turbulent Flow with Modified General Richardson Method. *Arabian Journal for Science and Engineering*, *45*(11), 9293–9303. https://doi.org/10.1007/s13369-020-04695-0

Armaly, B. F., Durst, F., Pereira, J. C. F., & Schönung, B. (1983). Experimental and theoretical investigation of backward-facing step flow. *Journal of Fluid Mechanics*, *127*(1), 473. https://doi.org/10.1017/S0022112083002839

Bailly, C., & Comte-Bellot, G. (2015). *Turbulence*. Springer International Publishing. https://doi.org/10.1007/978-3-319-16160-0

Baldwin, B., & Barth, T. (1991, January 7). A one-equation turbulence transport model for high Reynolds number wall-bounded flows. *29th Aerospace Sciences Meeting*. https://doi.org/10.2514/6.1991-610

Baldwin, B., & Lomax, H. (1978, January 16). Thin-layer approximation and algebraic model for separated turbulent flows. *16th Aerospace Sciences Meeting*. https://doi.org/10.2514/6.1978-257

Barbi, G., Chierici, A., Giovacchini, V., Giovacchini, V., Quarta, F., & Manservisi, S. (2022). Numerical simulation of a low Prandtl number flow over a backward facing step with an anisotropic four-equation turbulence model. *Journal of Physics*. https://doi.org/10.1088/1742-6596/2177/1/012006

Barkalov, K., Lebedev, I., Usova, M., Romanova, D., Ryazanov, D., & Strijhak, S. (2022). Optimization of Turbulence Model Parameters Using the Global Search Method Combined with Machine Learning. *Mathematics*, *10*(15). https://doi.org/10.3390/math10152708

Batchelor, G. K., & Gill, A. E. (1962). Analysis of the stability of axisymmetric jets. *Journal of Fluid Mechanics*, *14*(04), 529. https://doi.org/10.1017/S0022112062001421

Baughn, J. W., & Shimizu, S. (1989). Heat Transfer Measurements From a Surface With Uniform Heat Flux and an Impinging Jet. *Journal of Heat Transfer*, *111*(4), 1096–1098. https://doi.org/10.1115/1.3250776

Billard, F., & Laurence, D. (2012). A robust k-ε-v2/k elliptic blending turbulence model applied to near-wall, separated and buoyant flows. *International Journal of Heat and Fluid Flow*, *33*(1), 45–58. https://doi.org/10.1016/j.ijheatfluidflow.2011.11.003

Bisset, D. K., Antonia, R. A., & Browne, L. W. B. (1990). Spatial organization of large structures in the turbulent far wake of a cylinder. *Journal of Fluid Mechanics*, *218*(1), 439. https://doi.org/10.1017/S0022112090001069

Bradbury, L. J. S. (1965). The structure of a self-preserving turbulent plane jet. *Journal of Fluid Mechanics*, *23*(1), 31–64. https://doi.org/10.1017/S0022112065001222

Capp, S. P. (1983). *Experimental investigation of the turbulent axisymmetric jet* [PhD. Thesis]. State University of New York.

Chen, C. P., & Guo, K. (1991). A non-isotropic multiple-scale turbulence model. *Applied Mathematics and Mechanics*, *12*(10), 981–991. https://doi.org/10.1007/BF02451484

Chen, L., Asai, K., Nonomura, T., Xi, G., & Liu, T. (2018). A review of Backward-Facing Step (BFS) flow mechanisms, heat transfer and control. *Thermal Science and Engineering Progress*, *6*, 194–216. https://doi.org/10.1016/j.tsep.2018.04.004

Cheung, S. H., Oliver, T. A., Prudencio, E. E., Prudhomme, S., & Moser, R. D. (2011). Bayesian uncertainty analysis with applications to turbulence modeling. *Reliability Engineering & System Safety*, *96*(9), 1137–1149. https://doi.org/10.1016/j.ress.2010.09.013

Chiravalle, V. P. (2006). The k-L turbulence model for describing buoyancy-driven fluid instabilities. *Laser and Particle Beams*, *24*(3), 381–394. https://doi.org/10.1017/S026303460606054X

Chitta, V., Dhakal, T. P., & Walters, D. K. (2013). Development and Application of a New Four-Equation Eddy-Viscosity Model for Flows With Transition, Curvature and Rotation Effects. *Fluids Engineering Division Summer Meeting*, 1–10. https://doi.org/10.1115/fedsm2013-16372

Chou, P. Y. (1945). On velocity correlations and the solutions of the equations of turbulent fluctuation. *Quarterly of Applied Mathematics*, *3*(1), 38–54. https://doi.org/10.1090/qam/11999

Cooper, D., Jackson, D. C., Launder, B. E., & Liao, G. X. (1993). Impinging jet studies for turbulence model assessment—I. Flow-field experiments. *International Journal of Heat and Mass Transfer*, *36*(10), 2675–2684. https://doi.org/10.1016/S0017-9310(05)80204-2

Cotton, M. A., & Ismael, J. O. (1998). A strain parameter turbulence model and its application to homogeneous and thin shear flows. *International Journal of Heat and Fluid Flow*, *19*(4), 326–337. https://doi.org/10.1016/S0142-727X(98)10003-6

Craft, T. J. (1998). Developments in a low-Reynolds-number second-moment closure and its application to separating and reattaching flows. *International Journal of Heat and Fluid Flow*, *19*(5), 541–548. https://doi.org/10.1016/S0142-727X(98)10020-6

Craft, T. J., Graham, L. J. W., & Launder, B. E. (1993). Impinging jet studies for turbulence model assessment—II. An examination of the performance of four turbulence models. *International Journal of Heat and Mass Transfer*, *36*(10), 2685–2697. https://doi.org/10.1016/S0017-9310(05)80205-4

Craft, T. J., Iacovides, H., & Yoon, J. H. (2000). Progress in the Use of Non-Linear Two-Equation Models in the Computation of Convective Heat-Transfer in Impinging and

Separated Flows. *Flow, Turbulence and Combustion*, *63*(1/4), 59–80. https://doi.org/10.1023/A:1009973923473

Craft, T. J., Launder, B. E., & Suga, K. (1996). Development and application of a cubic eddy-viscosity model of turbulence. *International Journal of Heat and Fluid Flow*, *17*(2), 108–115. https://doi.org/10.1016/0142-727X(95)00079-6

Craft, T. J., Launder, B. E., & Suga, K. (1997). Prediction of turbulent transitional phenomena with a nonlinear eddy-viscosity model. *International Journal of Heat and Fluid Flow*, *18*, 15–28. https://doi.org/10.1016/S0142-727X(96)00145-2

Davidson, P. (2015). *Turbulence: An Introduction for Scientists and Engineers*. https://doi.org/10.1093/ACPROF:OSO/9780198722588.001.0001

de Zordo-Banliat, M., Merle, X., Dergham, G., & Cinnella, P. (2020). Bayesian model-scenario averaged predictions of compressor cascade flows under uncertain turbulence models. *Computers & Fluids*, *201*, 104473. https://doi.org/10.1016/j.compfluid.2020.104473

Deo, R. C., Mi, J., & Nathan, G. J. (2008). The influence of Reynolds number on a plane jet. *Physics of Fluids*, *20*(7). https://doi.org/10.1063/1.2959171

Dhakal, T. P., & Walters, D. K. (2011). A Three-equation variant of the SST k-w model sensitized to rotation and curvature effects. *Journal of Fluids Engineering, Transactions of the ASME*, *133*(11). https://doi.org/10.1115/1.4004940

Driver, D. M., & Seegmiller, H. L. (1985). Features of a reattaching turbulent shear layer in divergent channelflow. *AIAA Journal*, *23*(2), 163–171. https://doi.org/10.2514/3.8890

Duarte, C. A. R., Duarte, L. E. R., de Lima, B. S., & de Souza, F. J. (2020). Performance of an optimized k−ϵ turbulence model for flows around bluff bodies. *Mechanics Research Communications*, *105*. https://doi.org/10.1016/j.mechrescom.2020.103518

Duranti, S., & Pittaluga, F. (2000). Navier-Stokes Prediction of Internal Flows with a Three-Equation Turbulence Model. *AIAA Journal*. https://doi.org/10.2514/2.1075

Everitt, K. W., & Robins, A. G. (1978). The development and structure of turbulent plane jets. *Journal of Fluid Mechanics*, *88*(3), 563–583. https://doi.org/10.1017/S0022112078002281

Fabris, G. (1979). Conditional sampling study of the turbulent wake of a cylinder. Part 1. *Journal of Fluid Mechanics*, *94*(4), 673–709. https://doi.org/10.1017/S0022112079001245

Fares, E., & Schröder, W. (2005). A general one-equation turbulence model for free shear and wall-bounded flows. *Flow, Turbulence and Combustion*, *73*(3–4), 187–215. https://doi.org/10.1007/S10494-005-8625-Y/METRICS

Fürst, J., Příhoda, J., & Straka, P. (2013). Numerical simulation of transitional flows. *Computing*, *95*(1), 163–182. https://doi.org/10.1007/s00607-012-0266-0

Galperin, B., & Orszag, S. A. (2010). *Large Eddy Simulation of Complex Engineering and Geophysical Flows* (2nd ed.). Cambridge University Press.

Garnier, E., Adams, N., & Sagaut, P. (2009). *Large Eddy Simulation for Compressible Flows* (1st ed.). Springer Netherlands. https://doi.org/10.1007/978-90-481-2819-8

Ghirelli, F. (2007). κεα: A three-equation eddy-viscosity model of turbulence. *International Journal of Numerical Methods for Heat and Fluid Flow*, *17*(2), 140–164. https://doi.org/10.1108/09615530710723939

Gibson, M. M., & Launder, B. E. (1978). Ground effects on pressure fluctuations in the atmospheric boundary layer. *Journal of Fluid Mechanics*, *86*(3), 491–511. https://doi.org/10.1017/S0022112078001251

Goebel, S. G., & Dutton, J. C. (1991). Experimental study of compressible turbulent mixing layers. *AIAA Journal*, *29*(4), 538–546. https://doi.org/10.2514/3.10617

Goldberg, U. C. (1996a). Exploring a three-equation R-k-ε turbulence model. *Journal of Fluids Engineering-Transactions of The Asme*. https://doi.org/10.1115/1.2835511

Goldberg, U. C. (1996b). Exploring a three-equation r-k-ϵ turbulence model. *Journal of Fluids Engineering, Transactions of the ASME*, *118*(4), 795–799. https://doi.org/10.1115/1.2835511

Goldberg, U., Peroomian, O., Batten, P., & Chakravarthy, S. (2009). The k-ε-Rt Turbulence Closure. *Engineering Applications of Computational Fluid Mechanics*, *3*(2), 175–183. https://doi.org/10.1080/19942060.2009.11015263

Gomez, C. A., & Girimaji, S. S. (2011). Algebraic reynolds stress model (ARSM) for compressible shear flows. *41st AIAA Fluid Dynamics Conference and Exhibit*. https://doi.org/10.2514/6.2011-3572

Grunloh, T. P. (2019). Four equation k-omega based turbulence model with algebraic flux for supercritical flows. *Annals of Nuclear Energy*. https://doi.org/10.1016/j.anucene.2018.09.024

Guillas, S., Glover, N., & Malki-Epshtein, L. (2014). Bayesian calibration of the constants of the k-ε turbulence model for a CFD model of street canyon flow. *Computer Methods in Applied Mechanics and Engineering*, *279*, 536–553. https://doi.org/10.1016/j.cma.2014.06.008

Gul, M. Z., Yangaz, M. U., & Sen, S. (2024). A Two-Time-Scale Turbulence Model and Its Application in Free Shear Flows. *Applied Sciences*, *14*(3), 1133. https://doi.org/10.3390/app14031133

Gul, Z. (1994). *Prediction of In-Cylinder Flow By Use of a Multiple Time Scale Turbulence Models* [PhD]. UMIST.

Gunasekaran, S., & Altman, A. (2021). Far Wake and Its Relation to Aerodynamic Efficiency. *Energies*, *14*(12), 3641. https://doi.org/10.3390/en14123641

Gutmark, E., & Wygnanski, I. (1976). The planar turbulent jet. *Journal of Fluid Mechanics*, *73*(3), 465–495. https://doi.org/10.1017/S0022112076001468

Hamlington, P. E., & Ihme, M. (2014). Modeling of Non-Equilibrium Homogeneous Turbulence in Rapidly Compressed Flows. *Flow, Turbulence and Combustion*, *93*(1), 93–124. https://doi.org/10.1007/s10494-014-9535-7

Hanjalić, K., Jakirlić, S., & Hadžić, I. (1997). Expanding the limits of "equilibrium" second-moment turbulence closures. *Fluid Dynamics Research*, *20*(1–6), 25–41. https://doi.org/10.1016/S0169-5983(96)00043-3

Hanjalić, K., & Launder, B. (2011). *Modelling Turbulence in Engineering and the Environment*. Cambridge University Press. https://doi.org/10.1017/CBO9781139013314

Hanjalic, K., Launder, B. ~E., & Schiestel, R. (1979). Multiple-time-scale concepts in turbulent transport modelling. *2nd Symposium on Turbulent Shear Flows*, 10.31-10.36.

Hanjalic, K., Launder, B., & Schiestel, R. (1980). Multiple-time-scale concepts in turbulent transport modeling. *Turbulent Shear Flows 2*, 36–49.

Heskestad, G. (1964). Hot-wire measurements in a plane turbulent jet. *Journal of Applied Mechanics, Transactions ASME*, *32*(4), 721–734. https://doi.org/10.1115/1.3627309

Heskestad, G. (2011). Hot-Wire Measurements in a Plane Turbulent Jet. *Journal of Applied Mechanics*, *32*(4), 721. https://doi.org/10.1115/1.3627309

Hussein, H. J., Capp, S. P., & George, W. K. (1994). Velocity measurements in a high-Reynolds-number, momentum-conserving, axisymmetric, turbulent jet. *Journal of Fluid Mechanics*, *258*(1), 31–75.

Hussein, H. J., & George, W. K. (1989). Measurement of small scale turbulence in an axisymmetric jet using moving hot-wires. *7th Symposium on Turbulent Shear Flows*, *2*, 30.2.1-30.2.6. https://ui.adsabs.harvard.edu/abs/1989tsf.....2...30H/abstract

Igci, A. A., & Arici, M. E. (2016). A comparative study of four low-Reynolds-number k - ε turbulence models for periodic fully developed duct flow and heat transfer. *Numerical Heat Transfer, Part B: Fundamentals*, *69*(3), 234–248. https://doi.org/10.1080/10407790.2015.1097141

John, V. (2004). *Large Eddy Simulation of Turbulent Incompressible Flows* (Vol. 34). Springer Berlin Heidelberg. https://doi.org/10.1007/978-3-642-18682-0

Kashefi, A., Rempe, D., & Guibas, L. J. (2021). A point-cloud deep learning framework for prediction of fluid flow fields on irregular geometries. *Physics of Fluids*, *33*(2). https://doi.org/10.1063/5.0033376

Kim, J., Moin, P., & Moser, R. (1987). Turbulence statistics in fully developed channel flow at low Reynolds number. *Journal of Fluid Mechanics*, *177*, 133–166. https://doi.org/10.1017/S0022112087000892

Kim, S.-W., & Chen, C.-P. (1990). A Multiple-Time-Scale Turbulence Model Based On Variable Partitioning Of The Turbulent Kinetic Energy Spectrum. *Numerical Heat Transfer, Part B: Fundamentals*, *16*(2), 193–211. https://doi.org/10.1080/10407798908944935

Klein, T. S., Craft, T. J., & Iacovides, H. (2015). Assessment of the performance of different classes of turbulence models in a wide range of non-equilibrium flows. *International Journal of Heat and Fluid Flow*, *51*, 229–256. https://doi.org/10.1016/J.IJHEATFLUIDFLOW.2014.10.017

Klein, T. S., Craft, T. J., & Iacovides, H. (2018). The development and application of two-time-scale turbulence models for non-equilibrium flows. *International Journal of Heat and Fluid Flow*, *71*(May), 334–352. https://doi.org/10.1016/j.ijheatfluidflow.2018.04.010

Langtry, R. B., & Menter, F. R. (2009). Correlation-Based Transition Modeling for Unstructured Parallelized Computational Fluid Dynamics Codes. *AIAA Journal*, *47*(12), 2894–2906. https://doi.org/10.2514/1.42362

Launder, B. E., Reece, G. J., & Rodi, W. (1975). Progress in the development of a Reynolds-stress turbulence closure. *Journal of Fluid Mechanics*, *68*(3), 537–566. https://doi.org/10.1017/S0022112075001814

Launder, B. E., & Sharma, B. I. (1974). Application of the Energy-Dissipation Model of Turbulence to the Calculation of Flow Near a Spinning Disc. *Letters in Heat and Mass Transfer*, *1*(2), 131–138.

Launder, B. E., & Spalding, D. B. (1974). The numerical computation of turbulent flows. *Computer Methods in Applied Mechanics and Engineering*, *3*(2), 269–289. https://doi.org/10.1016/0045-7825(74)90029-2

Lefantzi, S., Ray, J., Arunajatesan, S., & Dechant, L. (2014). *Tuning a RANS k-ε model for jet-in-crossflow simulations*.

Li, H., Zhang, Y., & Chen, H. (2020). Aerodynamic prediction of iced airfoils based on modified three-equation turbulence model. *AIAA Journal*, *58*(9), 3863–3876. https://doi.org/10.2514/1.J059206

Liu, J. (2013). A three-equation turbulence model for high-speed flows. *Science China Technological Sciences*, *56*(4), 803–811. https://doi.org/10.1007/s11431-013-5178-5

Liu, W., Fang, J., Rolfo, S., Moulinec, C., & Emerson, D. R. (2021). An iterative machine-learning framework for RANS turbulence modeling. *International Journal of Heat and Fluid Flow*, *90*. https://doi.org/10.1016/j.ijheatfluidflow.2021.108822

Lopez, M., & Walters, D. K. (2016). Prediction of transitional and fully turbulent flow using an alternative to the laminar kinetic energy approach. *Journal of Turbulence*, *17*(3), 253–273. https://doi.org/10.1080/14685248.2015.1062509

Louchez, P. R., Kawall, J. G., & Keffer, J. F. (1985). Investigation of the detailed spread characteristics of plane turbulent wakes. *Fifth Symposium on Turbulent Shear Flows, (Ithaca, U.S.A.,: Aug. 7-9, 1985)*, 98–109. https://doi.org/10.1007/978-3-642-71435-1_10

Ma, K., & Lai, H. (2016). Comparison of Five Two-Equation Turbulence Models for Calculation of Flow in 90° Curved Rectangular Ducts. *Journal of Applied Fluid Mechanics*, *9*(6), 2917–2931.

Mashayek, F., & Taulbee, D. B. (2002). A FOUR-EQUATION MODEL FOR PREDICTION OF GAS-SOLID TURBULENT FLOWS. *Numerical Heat Transfer Part B-Fundamentals*. https://doi.org/10.1080/104077902317240030

Menter, F. R. (1994). Two-equation eddy-viscosity turbulence models for engineering applications. *AIAA Journal*, *32*(8), 1598–1605. https://doi.org/10.2514/3.12149

Miller, D. R., & Comings, E. W. (1957). Static pressure distribution in the free turbulent jet. *Journal of Fluid Mechanics*, *3*(1), 1–16. https://doi.org/10.1017/S0022112057000440

Molchanov, A. M., & Bykov, L. V. (2013). Three-equation K-ε-Vn turbulence model for high-speed flows. *43rd Fluid Dynamics Conference*. https://doi.org/10.2514/6.2013-3181

Mompean, G. (1994). Three-equation turbulence model for prediction of the mean square temperature variance in grid-generated flows and round jets. *International Journal of Heat and Mass Transfer*, *37*(7), 1165–1172.

Morgan, B. E., Schilling, O., & Hartland, T. A. (2018). Two-length-scale turbulence model for self-similar buoyancy-, shock-, and shear-driven mixing. *Physical Review E*, *97*(1), 013104. https://doi.org/10.1103/PhysRevE.97.013104

Moukalled, F., Mangani, L., & Darwish, M. (2016). *The Finite Volume Method in Computational Fluid Dynamics* (Vol. 113). Springer International Publishing. https://doi.org/10.1007/978-3-319-16874-6_21

Nagano, Y., Kondoh, M., & Shimada, M. (1997). Multiple time-scale turbulence model for wall and homogeneous shear flows based on direct numerical simulations. *International Journal of Heat and Fluid Flow*, *18*(4), 346–359. https://doi.org/10.1016/S0142-727X(97)00015-5

Newman, B. G. (1967). *Turbulent Jets and Wakes in a Pressure Gradient*. DDC. https://books.google.com.tr/books?id=TKIQyAEACAAJ

Nowruzi, H., Ghassemi, H., & Ghiasi, M. (2017). Performance predicting of 2D and 3D submerged hydrofoils using CFD and ANNs. *Journal of Marine Science and Technology*, *22*(4), 710–733. https://doi.org/10.1007/s00773-017-0443-0

Orszag, S. A. (1970). Analytical theories of turbulence. *Journal of Fluid Mechanics*, *41*(2), 363–386. https://doi.org/10.1017/S0022112070000642

Panchapakesan, N. R., & Lumley, J. L. (1993). Turbulence measurements in axisymmetric jets of air and helium. Part 1. Air jet. *Journal of Fluid Mechanics*, *246*, 197–223. https://doi.org/10.1017/S0022112093000096

Park, C. H., & Park, S. O. (2005). A compressible turbulence model for the pressure–strain correlation. *Journal of Turbulence*, *6*. https://doi.org/10.1080/14685240500055095

Patel, V. C., Rodi, W., & Scheuerer, G. (1985). Turbulence models for near-wall and low Reynolds number flows - A review. *AIAA Journal*, *23*(9), 1308–1319. https://doi.org/10.2514/3.9086

Piquet, J. (1999). *Turbulent Flows* (1st ed.). Springer Berlin Heidelberg. https://doi.org/10.1007/978-3-662-03559-7

Pope, S. B. (2000). *Turbulent Flows*. Cambridge University Press. https://doi.org/10.1017/CBO9780511840531

Portal-Porras, K., Fernandez-Gamiz, U., Ugarte-Anero, A., Zulueta, E., & Zulueta, A. (2021). Alternative artificial neural network structures for turbulent flow velocity field prediction. *Mathematics*, *9*(16). https://doi.org/10.3390/math9161939

Prandtl, L. (1925). 7. Bericht über Untersuchungen zur ausgebildeten Turbulenz. *ZAMM - Journal of Applied Mathematics and Mechanics / Zeitschrift Für Angewandte Mathematik Und Mechanik*, *5*(2), 136–139. https://doi.org/10.1002/zamm.19250050212

Rahman, M. M., Siikonen, T., & Agarwal, R. K. (2011). Improved Low-Reynolds-Number One-Equation Turbulence Model. *AIAA Journal*, *49*(4), 735–747. https://doi.org/10.2514/1.J050651

Ramaprian, B. R., & Chandrasekhara, M. S. (1985). LDA measurements in plane turbulent jets. *Journal of Fluids Engineering, Transactions of the ASME*, *107*(2), 264–271. https://doi.org/10.1115/1.3242472

Ramaprian, B. R., & Chandrasekhara, M. S. (2009). LDA Measurements in Plane Turbulent Jets. *Journal of Fluids Engineering*, *107*(2), 264. https://doi.org/10.1115/1.3242472

Robins, A. (1973). *The structure and development of a plane turbulent free jet* [PhD. Thesis]. University of London.

Rodi, W. (1972). *The prediction of free turbulent boundary layers by use of a two-equation model of turbulence* [PhD. Thesis]. University of London.

Rodi, W. (1975). A review of experimental data of uniform density free turbulent boundary layers. In B. E. Launder (Ed.), *Studies in Convection*. Academic Press.

Rodi, W. (1993). On the simulation of turbulent flow past bluff bodies. *Journal of Wind Engineering and Industrial Aerodynamics*, *46–47*, 3–19. https://doi.org/10.1016/0167-6105(93)90111-Z

Rodi, W., & Mansour, N. N. (1993). Low Reynolds number k-ε modelling with the aid of direct simulation data. *Journal of Fluid Mechanics*, *250*, 509–529. https://doi.org/10.1017/S0022112093001545

Rodi, W., & Spalding, D. B. (1970). A two-parameter model of turbulence, and its application to free jets. *Wärme- Und Stoffübertragung*, *3*(2), 85–95. https://doi.org/10.1007/BF01108029

Rotta, J. (1951a). Statistische Theorie nichthomogener Turbulenz. *Zeitschrift Für Physik*, *129*(6), 547–572. https://doi.org/10.1007/BF01330059

Rotta, J. (1951b). Statistische Theorie nichthomogener Turbulenz. *Zeitschrift Für Physik*, *129*(6), 547–572. https://doi.org/10.1007/BF01330059

Safronov, A. V., & Khotulev, V. A. (2008). Results of Experimental Researches of the Supersonic Cold and Hot Jet. *Physico-Chemical Kinetics in Gas Dynamics*, *6*.

Sávio, E., & Maciel, D. G. (2011). Comparison between the two-equation turbulence models of Jones and Launder and of Wilcox and Rubesin applied to aerospace problems. *Journal of Mechanical Engineering Research*, *3*(July), 248–263.

Shih, T. H., Liou, W. W., Shabbir, A., Yang, Z., & Zhu, J. (1995). A new k-ϵ eddy viscosity model for high reynolds number turbulent flows. *Computers and Fluids*, *24*(3), 227–238. https://doi.org/10.1016/0045-7930(94)00032-T

Shih, T.-H., Liou, W. W., Shabbir, A., Yang, Z., & Zhu, J. (1995). A new k-ϵ eddy viscosity model for high reynolds number turbulent flows. *Computers & Fluids*, *24*(3), 227–238. https://doi.org/10.1016/0045-7930(94)00032-T

Shim, Y. M., Sharma, R. N., & Richards, P. J. (2013). Proper orthogonal decomposition analysis of the flow field in a plane jet. *Experimental Thermal and Fluid Science*, *51*, 37–55. https://doi.org/10.1016/j.expthermflusci.2013.06.014

Shuai, S., & Agarwal, R. K. (2020, January 6). A New Improved One-Equation Turbulence Model Based on k-kL Closure. *AIAA Scitech 2020 Forum*. https://doi.org/10.2514/6.2020-1075

SimScale. (2024, September 4). https://www.simscale.com/forum/t/what-is-y-yplus/82394

Singh, A., Aravind, S., Srinadhi, K., & Kannan, B. T. (2020). Assessment of Turbulence Models on a Backward Facing Step Flow Using OpenFOAM®. *IOP Conference Series: Materials Science and Engineering*, *912*(4), 042060. https://doi.org/10.1088/1757-899X/912/4/042060

Smith, A. M., & Cebeci, T. (1967). *Numerical Solution of the Turbulent-Boundary-Layer Equations*. https://apps.dtic.mil/sti/citations/AD0656430

Spalart, P., & Allmaras, S. (1992, January 6). A one-equation turbulence model for aerodynamic flows. *30th Aerospace Sciences Meeting and Exhibit*. https://doi.org/10.2514/6.1992-439

Spalart, P. R. (2000). Strategies for turbulence modelling and simulations. *International Journal of Heat and Fluid Flow*, *21*(3), 252–263. https://doi.org/10.1016/S0142-727X(00)00007-2

Speziale, C. G., Sarkar, S., & Gatski, T. B. (1991). Modelling the pressure–strain correlation of turbulence: an invariant dynamical systems approach. *Journal of Fluid Mechanics*, *227*, 245–272. https://doi.org/10.1017/S0022112091000101

Sreenivasan, K. R., & Narasimha, R. (1982). Equilibrium parameters for two-dimensional turbulent wakes. *Journal of Fluids Engineering, Transactions of the ASME*, *104*(2), 167–169. https://doi.org/10.1115/1.3241801

Strelets, M. (2001, January 8). Detached eddy simulation of massively separated flows. *39th Aerospace Sciences Meeting and Exhibit*. https://doi.org/10.2514/6.2001-879

Su, X., Li, X., Wang, X., Liu, Y., Chen, Q., Shi, Q., Sheng, X., Sheng, X., & Gu, L. (2022). Development and Assessment of an Isotropic Four-Equation Model for Heat Transfer of Low Prandtl Number Fluids. *Frontiers in Energy Research*. https://doi.org/10.3389/fenrg.2022.816560

Sun, L., An, W., Liu, X., & Lyu, H. (2019). On developing data-driven turbulence model for DG solution of RANS. In *Chinese Journal of Aeronautics* (Vol. 32, Issue 8, pp. 1869–1884). Chinese Journal of Aeronautics. https://doi.org/10.1016/j.cja.2019.04.004

Sung, H. J., & Chung, M. K. (1984). Four-Equation Turbulence Model for Prediction of the Turbulent Boundary Layer affected by Buoyancy Force over a Flat Plate. *International Journal of Hydrogen Energy*. https://doi.org/10.1016/0017-9310(84)90097-8

Tahry, S. H. El. (1983). k-epsilon equation for compressible reciprocating engine flows. *Journal of Energy*, *7*(4), 345–353. https://doi.org/10.2514/3.48086

Tannehill, J., Anderson, D. A., & Pletcher, R. H. (2013). Computational Fluid Mechanics and Heat Transfer. In *Journal of Fluid Mechanics* (3rd edition, Vol. 172, Issue 1). https://doi.org/10.1017/S0022112086211878

Taulbee, D. B., Hussein, H., & Capp, S. (1987). Round jet - experiment and inferences on turbulence modeling. *6th Symposium on Turbulent Shear Flows*, 10-5–1. http://inis.iaea.org/Search/search.aspx?orig_q=RN:19096716

Thangam, S., Abid, R., & Speziale, C. G. (1992). Application of a new K-tau model to near wall turbulent flows. *AIAA Journal*, *30*(2), 552–554. https://doi.org/10.2514/3.10952

Thuerey, N., Weißenow, K., Prantl, L., & Hu, X. (2020). Deep Learning Methods for Reynolds-Averaged Navier–Stokes Simulations of Airfoil Flows. *AIAA Journal*, *58*(1), 25–36. https://doi.org/10.2514/1.J058291

Townsend, A. A. (1949). The fully developed turbulent wake of a circular cylinder. *Australian Journal of Scientific Research, Series A: Physical Sciences*, *2*, 451–468.

Tracey, B., Duraisamy, K., & Alonso, J. (2013, January 7). Application of Supervised Learning to Quantify Uncertainties in Turbulence and Combustion Modeling. *51st AIAA Aerospace Sciences Meeting Including the New Horizons Forum and Aerospace Exposition*. https://doi.org/10.2514/6.2013-259

Tu, J., Yeoh, G.-H., & Liu, C. (2012). *Computational Fluid Dynamics* (2nd ed.). Elsevier. https://doi.org/10.1016/C2015-0-06135-4

Van der Hegge Zijnen, B. G. (1958). Measurements of the velocity distribution in a plane turbulent jet of air. *Applied Scientific Research, Section A*, *7*(4), 256–276. https://doi.org/10.1007/BF03185052

Versteeg, H. K. (Henk K., & Malalasekera, W. (Weeratunge). (2007). *An introduction to computational fluid dynamics : the finite volume method*. Pearson Education Ltd. https://books.google.com.tr/books/about/An_Introduction_to_Computational_Fluid_D.html?id=RvBZ-UMpGzIC&redir_esc=y

Walters, D. K., & Cokljat, D. (2008). A three-equation eddy-viscosity model for reynolds-averaged navier-stokes simulations of transitional flow. *Journal of Fluids Engineering, Transactions of the ASME*, *130*(12), 1214011–12140114. https://doi.org/10.1115/1.2979230

White, F. M. (2011). *Fluid Mechanics* (7th ed., Vol. 1). McGraw Hill. https://books.google.com.tr/books?id=egk8SQAACAAJ

Wieghardt, K., & Tillman, W. (1951). *On the Turbulent Friction Layer for Rising Pressure*.

Wilcox, D. C. (1988a). Multiscale model for turbulent flows. *AIAA Journal*, *26*(11), 1311–1320. https://doi.org/10.2514/3.10042

Wilcox, D. C. (1988b). Reassessment of the scale-determining equation for advanced turbulence models. *AIAA Journal*, *26*(11), 1299–1310. https://doi.org/10.2514/3.10041

Wilcox, D. C. (2006). *Turbulence Modeling for CFD* (3rd ed.). D C W Industries. https://www.amazon.com/Turbulence-Modeling-Third-David-Wilcox/dp/1928729088

Wu, C.-T., Ferziger, J. ~H., & Chapman, D. ~R. (1985). Simulation and modeling of homogeneous, compressed turbulence. *5th Symposium on Turbulent Shear Flows*, 17.13-17.19.

Wygnanski, I., Champagne, F., & Marasli, B. (1986). On the large-scale structures in two-dimensional, small-deficit, turbulent wakes. *Journal of Fluid Mechanics*, *168*(1), 31. https://doi.org/10.1017/S0022112086000289

Wygnanski, I., & Fiedler, H. (1969). Some measurements in the self-preserving jet. *Journal of Fluid Mechanics*, *38*(3), 577–612. https://doi.org/10.1017/S0022112069000358

Yakhot, V., Orszag, S. A., Thangam, S., Gatski, T. B., & Speziale, C. G. (1992). Development of turbulence models for shear flows by a double expansion technique. *Physics of Fluids A*, *4*(7), 1510–1520. https://doi.org/10.1063/1.858424

Yoshizawa, A. (1990). Three-equation modeling of inhomogeneous compressible turbulence based on a two-scale direct-interaction approximation. *Physics of Fluids A*, *2*(5), 838–850. https://doi.org/10.1063/1.857632

Zhang, Y., Zhang, D., & Jiang, H. (2023). Review of Challenges and Opportunities in Turbulence Modeling: A Comparative Analysis of Data-Driven Machine Learning Approaches. In *Journal of Marine Science and Engineering* (Vol. 11, Issue 7). Multidisciplinary Digital Publishing Institute (MDPI). https://doi.org/10.3390/jmse11071440

Zhao, Y., Akolekar, H. D., Weatheritt, J., Michelassi, V., & Sandberg, R. D. (2020). RANS turbulence model development using CFD-driven machine learning. *Journal of Computational Physics*, *411*. https://doi.org/10.1016/j.jcp.2020.109413

Zhou, Y., Antonia, R. A., & Tsang, W. K. (1998). The effect of Reynolds number on a turbulent far-wake. *Experiments in Fluids*, *25*(2), 118–125. https://doi.org/10.1007/s003480050215

BRIEF BIO

Murat Umut Yangaz graduated in 2012 from Mechanical Engineering Department, Faculty of Engineering, Uludag University. After working as an engineer in automotive industry for a brief period, he started his graduate education at Marmara University for his Master's Degree in Mechanical Engineering in 2013 and graduated in 2014. During this period, he was employed at Sakarya University as a research assistant. After graduation, he began to work at Marmara University, where he has completed his Ph.D. in Mechanical Engineering by carrying out this study. He also holds a Master's Degree in Chemical Engineering.